

Ab initio modelling of thermal plasma gas discharges (electric arcs)

Von der Gemeinsamen Naturwissenschaftlichen Fakultät
der Technischen Universität Carolo-Wilhelmina

zu Braunschweig

zur Erlangung des Grades eines
Doktors der Naturwissenschaften

(Dr.rer.nat.)

genehmigte

D i s s e r t a t i o n

von Jens Wendelstorf
aus Tübingen

1. Referent: Univ.-Prof. Dr. U. Motschmann
2. Referent: Univ.-Prof. Dr. M. Kock
3. Referent: Univ.-Prof. Dr. J. Mentel
eingereicht am: 6. Juli 2000
mündliche Prüfung (Disputation) am: 20. Dezember 2000

2000

Teilergebnisse aus dieser Arbeit wurden mit Genehmigung der Gemeinsamen Naturwissenschaftlichen Fakultät, vertreten durch den Mentor der Arbeit, in folgenden Beiträgen vorab veröffentlicht:

1. J. Wendelstorf: Two-temperature, two-dimensional modeling of cathode-plasma interaction in electric arcs. In P. Pisarczyk, T. Pisarczyk and J. Wolowski (Ed.): *Proceedings of the XXIV International Conference on Phenomena in Ionized Gases*, Warschau, Polen, 11-16 July 1999 (ISBN 83-902319-5-6), Bd.II, S.227-228
(best computational poster award)
2. J. Wendelstorf, H. Wohlfahrt und G. Simon: Two-temperature, two-dimensional modeling of cathode hot spot formation including sheath effects – application to high pressure xenon arc lamps. In: C. Deeney (Ed.): 1999 IEEE Int. Conf. on Plasma Science, Monterey, California, USA, 20-24.6.1999. IEEE Cat. No. 99CH36297 (ISBN 0-7803-5224-6), S.240 (5P03)
3. J. Wendelstorf, I. Decker, H. Wohlfahrt und G. Simon: Modeling of arc-electrode systems - preliminary results for high pressure xenon arc lamps. *8th Int. Symposium on the Science & Technology of Light Sources (LS-8)*, Greifswald, 30.8.-3.9.1998 (ISBN 3-00-003105-7), S.382-383
4. J. Wendelstorf, I. Decker, H. Wohlfahrt und G. Simon: Investigation of cathode spot behavior of atmospheric argon arcs by mathematical modeling. In: G. Babucke (ed.), *XII Int. Conf. Gas Discharges and their Applications*, Greifswald, 8.-12.9.1997 (ISBN 3-00-001760-7), Bd.I (1997), S.62-65
5. I. Decker, O. Voß, J. Wendelstorf und H. Wohlfahrt: Nutzen numerischer Simulationen für den Einsatz realer Schweißprozesse. *DVS-Berichte*, Bd.186 (1997), S.34-38
6. J. Wendelstorf, I. Decker, H. Wohlfahrt und G. Simon: TIG and plasma arc modelling. In: H. Cerjak (ed.), *Mathematical Modelling of Weld Phenomena 3* (ISBN 1-86125-010-X), The Institute of Materials, London, 1997, S.848-897
7. B. Rethfeld, J. Wendelstorf, T. Klein und G. Simon: A self-consistent model for the cathode fall region of an electric arc. *J. Phys. D: Appl. Phys.*, Bd.29 (1996), S.121-128
8. J. Wendelstorf, I. Decker, H. Wohlfahrt und G. Simon: Berechnung anwendungsrelevanter Zielgrößen von thermischen Lichtbögen: Kathodenfallmodelle und deren Integration in die Lichtbogenmodellierung. *8te Bundesdeutsche Fachtagung Plasmatechnologie*, Dresden, 14-17.7.1997, S.17
9. J. Wendelstorf, G. Simon, I. Decker und H. Wohlfahrt: Untersuchungen zur Berechenbarkeit technologischer Parameter thermischer Lichtbögen am Beispiel des atmosphärischen Argonbogens. *Verhandl. DPG (VI)*, Bd.32 (1997), S.7
10. J. Wendelstorf, I. Decker, H. Wohlfahrt und G. Simon: Modellierung thermischer Lichtbögen zur Optimierung von technologischen Prozeßparametern. *7te Bundesdeutsche Fachtagung Plasmatechnologie*, Bochum 13-14.3.1996, S.118
11. J. Wendelstorf, I. Decker, H. Wohlfahrt und G. Simon: Modellierung des Kathodenfalls zur Simulation thermischer Lichtbögen. *7te Bundesdeutsche Fachtagung Plasmatechnologie*, Bochum 13-14.3.1996, S.37
12. B. Rethfeld, T. Klein, C. Tix, J. Wendelstorf und G. Simon: Modellierung der katodennahen Plasmarandschichten eines WIG-Lichtbogens. *Verhandl. DPG (VI)* Bd.30 (1995), S.243

Braunschweig, 6. Juli 2000

Copyright © Jens Wendelstorf 2000

Alle Rechte, auch das des auszugsweisen Nachdruckes, der auszugsweisen oder vollständigen Wiedergabe, der Speicherung in Datenverarbeitungsanlagen und der Übersetzung, vorbehalten.

Jens Wendelstorf

eMail: jens@wendelstorf.de

Internet: <http://www.wendelstorf.de>

dedicated

to

Prof. Dr. Gerhard Simon

*23.1.1930

†11.2.2000

Kurzfassung:

Thermische Plasmen wurden in Form von Lichtbogenentladungen Anfang des neunzehnten Jahrhunderts entdeckt. Die fundamentalen physikalischen Mechanismen dieser Gasentladungen wurden bereits im Jahre 1903 von J. Stark beschrieben. Während die grundlegende Physik dieses Phänomens somit weitgehend bekannt ist, war es bis heute praktisch kaum möglich, wesentliche Entladungsparameter quantitativ vorauszuberechnen.

Ein fundamentales Problem der Modellierung lag in der Beschreibung der Nichtgleichgewichtsgebiete (Plasmaschichten) vor den Elektroden. Das andere war die Tatsache, daß es sich bei diesen elektrischen Entladungen um dissipative, selbstorganisierende Systeme handelt, deren Eigenschaften sich erst aus der komplexen Wechselwirkung ihrer Teilsysteme ergeben (Emergenz). Diese Probleme werden im Rahmen dieser Arbeit diskutiert und weitgehend gelöst.

Basierend auf der Motivation des Themas und der Geschichte seiner Untersuchung wird zunächst ein Konzept zur vollständigen quantitativen Vorausberechnung dieses Typs von Gasentladungen entwickelt. Es folgt eine physikalische Beschreibung der Lichtbogenteilsysteme Elektrodenfestkörper, Elektrodenoberfläche, Raumladungs- und Ionisationsschichten und der Plasmasäule. Die zur Lösung notwendigen Plasmamaparameter und Transportkoeffizienten werden für den Fall des partiellen lokalen thermodynamischen Gleichgewichts (pLTG) in Abhängigkeit von Elektronen- und Schwerteilchentemperatur und Entladungsdruck berechnet. Mit diesem *ab initio* Gesamtmodell werden dann zunächst die wesentlichen Eigenschaften der Entladung im Detail berechnet. Eine Variation der Entladungsparameter Gas, Druck, Strom und Kathodendurchmesser weist im folgenden die quantitative Berechenbarkeit der fundamentalen Verhaltensweisen von Lichtbögen im Entladungsdruckbereich von 0.1 bis 8 MPa und Strömen oberhalb von 1A für Argon, Xenon und Quecksilber als Plasmamedium nach. Durch das rechnerische Ausschalten einzelner physikalischer Effekte wird deren konkreter Einfluß auf das Verhalten der Entladung untersucht. Diese Analyse gestattet zusammen mit einer im Bezug auf die benötigten Stoßquerschnitte durchgeführten Sensitivitätsanalyse eine Bewertung des Vergleichs mit anderen Modellen und den wenigen quantitativen Messwerten, die für derartige Hochdruckbogenentladungen bisher publiziert wurden.

Für sehr unterschiedliche Entladungsparameter wird ein Vergleich mit dem Experiment vorgenommen, welcher insbesondere die hohe Genauigkeit des entwickelten Kathodenfallmodells nachweist und erste Validierungsaussagen liefert.

Die Zusammenfassung stellt die wesentlichen Neuerungen des Berechnungskonzeptes und die grundlegenden physikalischen Prozesse kurz dar und beschreibt die große Zahl der möglichen Anwendungsbereiche des Modells. Es werden zudem Detailverbesserungen angeregt und Hinweise zur Durchführung von weiteren Validierungsexperimenten gegeben.

Bei dem vorliegenden Berechnungsverfahren wurde weitgehend auf ungerechtfertigte Vereinfachungen verzichtet und durch Kopplung der modellmäßigen Erfassung der Teilsysteme erstmalig die weitgehend vollständige quantitative Vorausberechenbarkeit dieses Typs von Gasentladungen nachgewiesen.

Abstract:

Thermal plasma gas discharges (electric arcs) were discovered at the beginning nineteenth century. The fundamental physical mechanisms of such gas discharges were described first by J. Stark in 1903. While the basic physical laws governing this phenomenon are mostly well known, up to now, a quantitative prediction of the fundamental discharge parameters was practically impossible.

One fundamental modelling problem was the description of the non equilibrium layers (plasma sheaths) in front of the electrodes. Additionally, such electric discharges are dissipative self organizing systems. Their properties emerge from the complex interaction of their parts. These problem will be addressed and solved by this work.

Based on a motivation of the objective and the history of its investigation, a concept of a complete self consistent quantitative prediction of such electric arcs was developed. A physical description of the physical partial systems electrode solid, electrode surface, space charge and ionization sheaths and plasma column is provided. For the case of partial local thermodynamic equilibrium (pLTE), the plasma parameters and transport coefficients as a function of electron- and heavy particles temperature are calculated. Using this *ab initio* model, the properties of arc discharges are computed. A variation of the discharge parameters gas, pressure, current and cathode diameter establishes the quantitative predictability of the fundamental arc behaviour for a discharge pressure range of 0.1 to 8 MPa and arc currents above 1 A for argon, xenon and mercury fillings. By computational disabling individual physical effects, their specific influence on the discharge behaviour will be investigated. Together with the sensitivity analysis performed with respect to the required cross section data, this analysis allows for an assessment of the comparison with other models and the few available experimental results, actually published for such high pressure arc discharges.

For a number of very different discharge parameters an experimental validation is provided. Especially the high precision of the cathode layer model becomes evident leading to a first positive model assessment.

Finally, the main innovations of the computational concept and the basic physical processes together with the broad range of application areas of the model are summarized. Some enhancements are proposed and the realization of validation experiments will be discussed.

The present computational scheme cuts out most unjustified simplifications and, by a numerical coupling of the partial systems models, a complete quantitative predictability of this type of electric gas discharges is established.

Contents

1	Introduction	1
1.1	A short history of thermal plasma gas discharges	3
1.2	Fields of model applications	5
1.3	A practical definition of <i>ab initio</i> modelling	6
1.4	Outline of this work	8
2	Conceptual framework for modelling electric arc discharges	9
2.1	Introduction to complex adaptive systems	10
2.1.1	Complexity measures	12
2.1.2	Emergence: self generated complexity	12
2.1.3	Is the arc discharge a complex system?	13
2.2	The overall behaviour of arc discharges	15
2.3	Numerical modelling concepts	16
2.4	The transfer function concept	18
2.5	Summary of the concept	19
3	Physics of the electric arc discharge	23
3.1	Introduction	23
3.1.1	Basic discharge features	23
3.1.2	Modelling tasks	28
3.2	Physical processes inside the electrodes and at the electrode surface	29
3.3	The cathode–plasma transition layers	32
3.3.1	Electron emission of the cathode surface	32
3.3.2	Space charge layer (sheath)	35
3.3.3	Energy balance and current continuity at the sheath edge	36
3.3.4	Ionization layer (pre-sheath)	36
3.3.5	A simple presheath control model	37
3.3.6	Sheath-surface boundary conditions	38
3.3.7	Presheath-plasma boundary conditions	39
3.4	The anode–plasma transition layers	39
3.5	The thermal arc plasma	42
3.5.1	Modelling the flow of the conducting plasma fluid	42
3.5.2	Modelling the energy transport within the plasma	43
3.5.3	Modelling the electric current transport	44
3.5.4	Diffusion and other transport phenomena	46
3.6	Summary of the arc discharge physics	47

4	Plasma properties and transport coefficients	49
4.1	Introduction	49
4.2	Plasma composition and thermodynamic properties	50
4.2.1	The condition of quasineutrality	50
4.2.2	Dalton's law	50
4.2.3	Saha-Eggert equation	51
4.2.4	Mass density	53
4.2.5	Enthalpy	53
4.2.6	Specific heat	54
4.3	Particle collision integrals	56
4.3.1	Neutral particle interaction	56
4.3.2	Charged particle interaction	56
4.3.3	Ion atom interaction	57
4.3.4	Electron atom interaction	57
4.3.5	Summary of particle collision modelling	57
4.4	Energy exchange term for the pLTE model	59
4.4.1	Elastic energy exchange rate	59
4.4.2	Inelastic energy exchange rate	59
4.5	Diffusivities	60
4.6	Viscosity	61
4.7	Heat conductivity	62
4.7.1	Electron heat conductivity	62
4.7.2	Heavy particles translational heat conductivity	62
4.7.3	Heavy particles internal heat conductivity	63
4.7.4	Heavy particles reactive heat conductivity	63
4.8	Electric conductivity	66
4.9	Simple treatment of radiation effects	68
4.10	Simple treatment of ionization non-equilibrium	71
4.11	Sensitivity analysis of the transport coefficients and their influence on the resulting discharge parameters	71
5	Modelling results, validation and sensitivity analysis	73
5.1	Introduction	73
5.2	Detailed properties computed for a representative arc configuration (model lamp)	73
5.2.1	Properties of the overall discharge	76
5.2.2	Properties of the cathode hot spot	82
5.2.3	Parameter variations	84
5.2.4	Physical sensitivity analysis	99
5.3	Model validation	101
5.3.1	Low current atmospheric argon arc	102
5.3.2	Low current high pressure xenon model lamp	106
5.3.3	High pressure xenon arcs after Bauer and Schulz	108
5.3.4	The high pressure xenon short arc lamp	109
5.3.5	The high pressure mercury discharge	111
5.3.6	The TIG welding arc	114
5.4	Comparison with other modelling results	116
5.5	Summary of the modelling results and validation	117

6 Summary, applications, outlook and conclusions	119
6.1 Major achievements	119
6.2 Conceptual progress	121
6.3 Applications	121
6.4 Future developments	122
6.5 Conclusions	122
Bibliography	122

Unser Kopf ist rund,
damit das Denken
die Richtung wechseln
kann.

Francis Picabia

Chapter 1

Introduction

Conversion of electric power to high heat intensities or light fluxes can be efficiently achieved by **H**igh **I**ntensity gas **D**ischarges (HID). During the long history of commercial applications in this area, progress is often based on the *trial and error* approach. Due to their complexity and the number of possible parameter combinations, the development process relies on the practical experience of the individual developer but not directly on the existing physical knowledge about these discharges.

From the viewpoint of a scientist, atmospheric pressure gas discharges are very easy to obtain and thus understanding and modelling is a matter of scientific interest since the first detection of the arcing phenomenon itself in the nineteenth century. During the last decades, modern computing hardware and advanced software provides the opportunity to compute the overall discharge behaviour in advance and in a quantitative way. This work is dedicated to contribute to the understanding of the overall discharge properties by using these new modelling tools. This objective is reached by the development and application of accurate and validated modelling software.

The investigations are applicable to the so-called *thermal plasmas*, which are distinguished from other types of plasmas by the following characteristics:

- All species have Maxwellian velocity distribution. If they are all according to the same temperature the plasma is named to be in **L**ocal **T**hermodynamic **E**quilibrium (LTE), otherwise the equilibrium is stated to be **p**artial (pLTE).
- The excited energy states are populated to a Boltzmann term.
- Composition can be derived from **L**ocal **C**hemical **E**quilibrium (LCE) or demixing effects have to be calculated from an additional set of diffusion equations.
- Temperatures are less than a few eV (1eV=11604K).
- The plasma is not confined by an external magnetic field.
- The discharge is stabilized by its own magnetic field, by external gas flow, the electrodes or the surrounding solid or liquid walls.

In the American and European literature these plasmas are often called *hot plasmas* (the heavy particles are hot compared to low pressure gas discharges). In the Russian literature and in Germany they are often called *low temperature* plasmas, because their electron temperature is small compared to nuclear fusion plasmas.

During the last decades it became increasingly clear that the existence of LTE in a plasma is rather an exception than a rule. The excited states population often deviates from Boltzmann equilibrium. This is of major importance for spectroscopical plasma diagnostics, but for most practical applications at least the **p**artial **L**ocal **T**hermodynamic **E**quilibrium (pLTE) concept can be used for the following reasons:

- The contribution of the excited states to the total plasma enthalpy is very small.
- The local energy balance of the discharge is dominated by Joule heating, radiative, convective and conductive source terms.
- The plasma composition and transport coefficients mainly depends on the excitation (electron) temperature and the fundamental gas properties.
- There is no direct impact of specific excited states populations on global arc discharge properties.
- Large errors in the calculation of the excited states density highly affect experimental methods, were these quantities are required for data interpretation, but in the self-consistent system calculation, the effect is limited to very small changes in the calculated self-consistent plasma temperature distribution.

Typical discharge parameters are listed in table 1.1. The values are reflecting the typical application areas of these *arc discharges*: lighting and material processing, synthesis and destruction. In the following section, a short historical and application overview is provided. This is followed by the definition of *ab initio modelling*, the objective of the following chapters, as summarized in section 1.4.

Quantity	Range	Comparable to
max. power density	$10^7 \dots 10^9 \text{ J/m}^3$	chemical energy storage
max. current density	$10^7 \dots 10^9 \text{ A/m}^2$	critical current density for type II superconductors
electric field	$10^2 \dots 10^9 \text{ V/m}$	lightning
discharge pressure	$0.05 \dots 20 \text{ MPa}$	$0.5 \dots 200$ atmospheres
discharge power	$1 \dots 10^8 \text{ W}$	airplanes
discharge power density	$1 \dots 100 \cdot 10^6 \text{ W/m}^2$	electron beams
light intensity	$10^8 \dots 10^{10} \text{ cd/m}^2$	sunlight
light flux	$10^4 \dots 10^7 \text{ lm}$	sunlight
lighting efficacies	up to 300 lm/W	low pressure discharge lamps

Table 1.1: Parameters typical for thermal plasmas (for the technical term *efficacy* see e.g. [Way71]).

1.1 A short history of thermal plasma gas discharges

High intensity gas discharges are also called *electric arcs*, because the first discharge observed in detail was a carbon arc *burning* in horizontal position in the ambient atmosphere and thus bent by natural convection.

In table 1.2, a small collection of the milestones in the 200 years history of the arcing phenomenon is sketched. The arc discharge not only forms a basis for efficient discharge lamps, it is also an initiator for the development of plasma physics itself in the 1920's.

From discovery of a certain phenomenon (e.g. the use of metal halides for lighting purposes) to it's industrial use it can take more than 50 years and up to now, most practically important discharges cannot be computed in advance and thus may not be regarded as fully understood.

Year	Contributor	Contribution
1804	Davy	carbon arc lamp
1860	Berthelot	electric arc methane to acetylene conversion
1878	Siemens	arc melting
1890	Moissant, Heroult	arc furnaces
1901	Marconi	arc radio transmitter
1902	Ayrton	monograph <i>The electric arc</i> [Ayr02]
1905	Birkeland, Schönherr	nitrogen fixation
1911	Steinmetz	principle of metal halide arc lamps
1920	Eggert, Saha	equilibrium composition in plasmas
1923	Compton	low pressure sodium lamp
1930	Pirani	300 lm/W low pressure sodium lamp
1933		welding with carbon arcs
1935	Elenbaas	high pressure mercury lamp
1950	Maecker	segmented arc for fundamental research
1951		industrial plasma torches
1960	USAF/NASA	multi MW wind tunnels for space reentry simulation
1962		commercial metal halide arc lamps
1963	Schmidt	high pressure sodium lamps
1965	Paton	transferred arc plasmatron for stainless steel
1977	Liu	multidimensional model of the arc column
1981	Hsu	1st attempt of a 2-D pLTE model for the arc column
1984		arc synthesis of fullerenes
1987	Fischer	1st 2-D plasma electrode model for high pressure lamps
1988	Palacin	2-D model of the xenon short arc lamp column
1989	Tsai, Kou	column model with boundary fitted coordinates
1990	Delalondre	integrated 2-D column-cathode model
1991		low power high pressure mercury discharge car headlights
1995		plasma- and cathode surface temperature measurements for the tungsten inert gas (TIG) welding arc are state of the art
1997		2-D plasma-electrode models including convection are available for a number of discharge configurations
1998		commercial ultra high pressure (UHP)-mercury lamp (200bar)

Table 1.2: History of arc discharge science and technology.

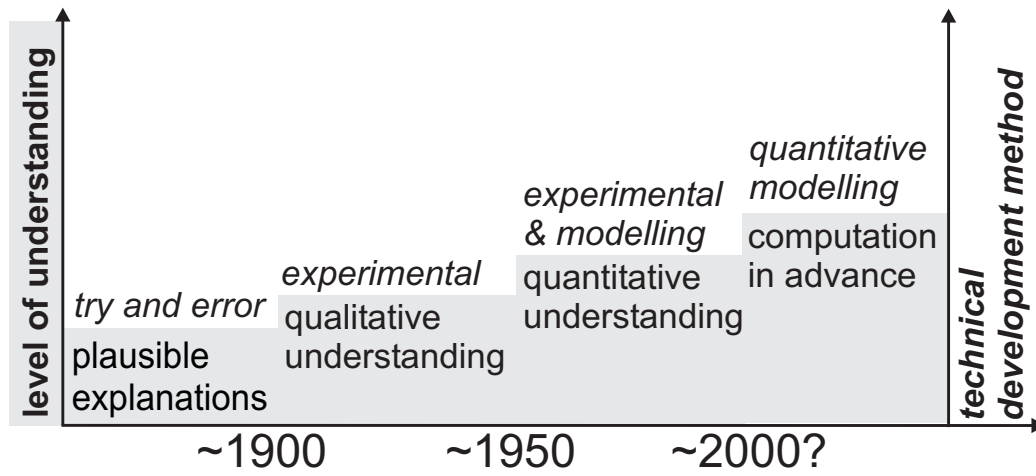


Figure 1.1: Development of HID science and technology.

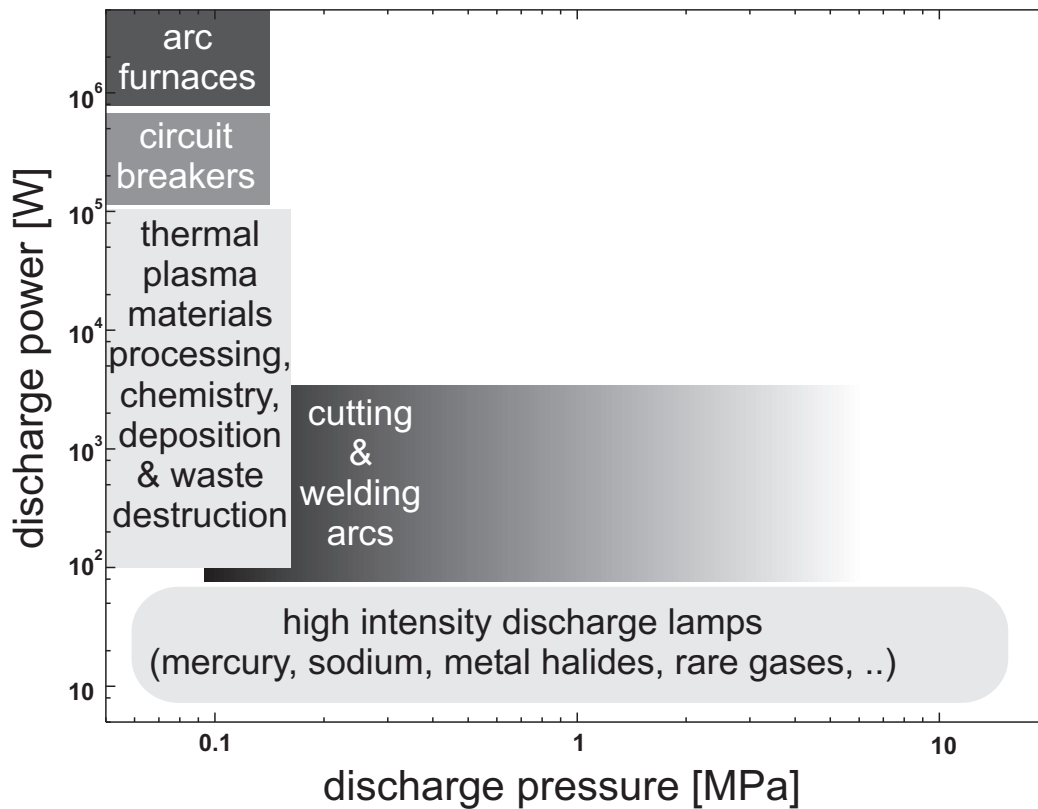


Figure 1.2: Applications of high intensity gas discharges.

Concluding from this long lasting history of the subject, every fifty years, there was a qualitative advance in the overall development paradigm (see figure 1.1). This work is dedicated to the actual change from trial & error supported by a first quantitative understanding to a computation of specific discharge features in advance.

1.2 Fields of model applications

As demonstrated in figure 1.2, discharge powers range from a few W to several MW and discharge pressures are atmospheric in most cases. For lighting and (underwater) materials processing purposes, hyperbaric applications became more and more important in the last decades.

This work is dedicated to the computation and quantitative understanding of arc discharges. As a first step, the models will be applicable to stationary discharges showing cylindrical symmetry:

- Arc lamps, at low frequency alternating current (AC) or direct current (DC), especially for the optimization of
 - electrode geometry and erosion,
 - global energy balances,
 - radiative properties.
- Welding arcs (see [WDWS97b])
 - optimized arc configurations will permit higher processing quality and performance,
 - the impact of new gas mixtures and electrode materials can be determined in advance.
- Arc furnaces (steel and high melting point materials synthesis)
 - optimized high power torches will allow to replace conventional carbon electrodes.
- Plasma torches for enhanced or even new applications:
 - waste destruction,
 - gas heating for reentry simulation and space propulsion,
 - synthesis of nanostructure materials (fullerenes),
 - plasma chemistry and materials deposition (plasma spraying) or removal (plasma etching).

Modelling of AC or pulsed operation and 3-D modelling is actually possible, but requiring large computing resources.

1.3 A practical definition of *ab initio* modelling

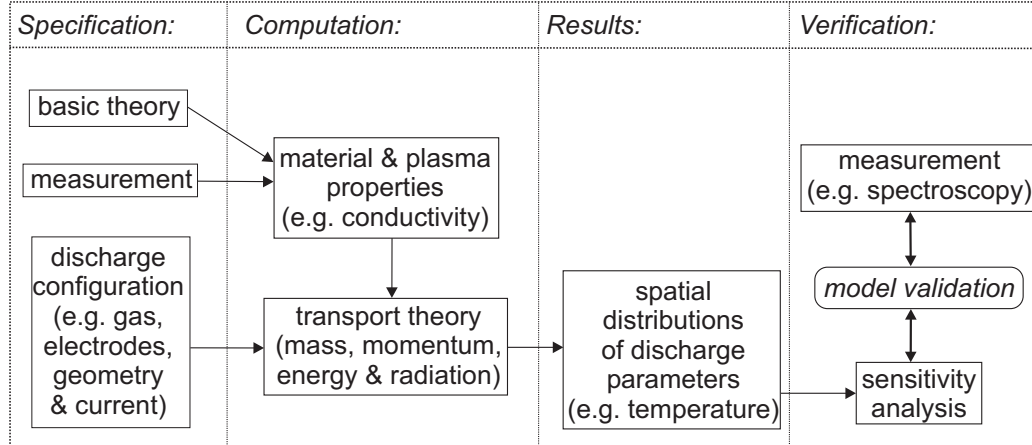


Figure 1.3: Information flow and subtasks of *ab initio* modelling.

The common meaning of *ab initio* modelling is computation based on first principles and fundamental constants. The practical definition used for this work is sketched in figure 1.3:

An *ab initio* model is based on fundamental physics and any material, gas- or plasma property determined by a discharge configuration independent method. The model should not contain any parameter or input value which has to be fitted to experimental discharge data for every individual configuration under investigation. A practical *ab initio* model should allow for the computation of important discharge characteristics with an accuracy better than experimental error or sufficient for automatic optimization of discharge configurations.

The underlying motivation for model development with such high accuracy is the extrapolation capability these models should have. Additionally the strong nonlinear character of the arc discharge implies a need for relative high computation accuracy. The model validation by quantitative comparison with experimental data has to be supplemented by a sensitivity analysis: Some experimental quantities are rather insensitive to changes in the arc configuration (e.g. doubling the current often implies only a few percent change in plasma temperature), while other are easy to determine (e.g. voltage-current characteristics) and also sensitive to important nonlinearity effects like mode transitions.

Sensitivity analysis has to be undertaken within all fields important for the development of the models and their validation:

- Modelling accuracy can be restricted in principle, by the numerical techniques applied and by the available computing resources.
- Validateability of the physical effects included will require detailed knowledge of the transport coefficients involved or the need to compute critical effects like mode transitions. The validation of physical details may be completely hidden by configuration- or measurement-inaccuracies.
- Analysis of the numerical schemes and their parameters allows to increase computation speed as well as to obtain important information on the principle accuracy of the concept.

As a result, some of the involved numerical schemes may be less accurate (10^{-3}), while other have to solve *stiff* problems at high accuracy ($< 10^{-8}$).

One of the most important experience from modelling such systems can be summarized in one sentence:

The validity of the physical description of the system can be justified *a posteriori* (afterwards), but not *a priori* (in advance).

Another is the importance of a sensitivity analysis in order to obtain information about the role of a specific input parameter (e.g. electrode work function) on the overall or local discharge behaviour.

The modelling approach is therefore relying on the comparison with selected reproduceable experimental data of known accuracy. The answers of this validation and sensitivity analysis are not always positive:

- The specific experimental data may be not accurate enough to validate a specific modelling approach, e.g. a validation of a cathode layer model by plasma temperature measurements may require unaffordable spatial resolutions and accuracies – cathode layer models are better justified by an electrical determination of the cathode fall voltage.
- The physical detail may be hidden by a material property not known with sufficient accuracy (e.g. cathode material work function).
- The physical or application detail may be superimposed by the dependency of the results on numerical parameters (e.g. grid size).
- The computing resources may not allow for a sensitivity analysis at all.
- The behaviour of the discharge system itself can be out of the range of the specific modelling approach (e.g. time dependent and 3-D, chaotic or stochastic).

The model will enhance the understanding of the arc phenomenon itself, but the overall objective is quantitative prediction of specific discharge configurations. Some sort of *understanding* of such complex systems can be *obtained* by many different plausible explanations or models with internal *fit parameters*. But these will fail if new discharge configurations are to be computed in advance.

1.4 Outline of this work

<i>Chapter 1:</i>	Introduction.
<i>Chapter 2:</i>	Conceptual framework for modelling electric arc discharges.
<i>Chapter 3:</i>	Physics of the electric arc discharge: <ul style="list-style-type: none"> • Plasma column. • Electrodes. • Electrode layers.
<i>Chapter 4:</i>	Plasma properties and transport coefficients.
<i>Chapter 5:</i>	Modelling results, validation and sensitivity analysis.
<i>Chapter 6:</i>	Summary, outlook and conclusions.

Table 1.3: Outline of this work.

Mathematical or physical modelling conventionally consists of a derivation of the equations describing the system and then solving them. This requires making all assumptions and approximations in advance. As the systems under investigation become more complex, this procedure becomes inapplicable in terms of effort and due to the nonlinearity of nature. Initially made assumptions need to be controlled afterwards and the modelling work becomes an iterative process itself.

Most of all important arc phenomena occur as an *emerging* result of the interaction of different physical processes and discharge regions. The accurate modelling of the individual parts of the discharge is a prerequisite, but the iterative linkage of these models is of the same importance. As sketched in table 1.3, the overall modelling approach is discussed first in chapter 2. After *sectioning* the discharge into regions governed by different physical processes, the global iteration algorithms needed for the complete discharge description are presented. Within chapter 3, the physical models of the plasma column, the electrodes and the boundary layers are presented. The computation of the basic plasma properties and transport coefficients is summarized in chapter 4.

In chapter 5, the model proves its ability to reproduce all major discharge features. Initially, an easy computable arc configuration is selected, and the detailed results available from the modelling data are provided. Additionally, the impact and origin of the flow pattern formation are discussed. For this model lamp, the general arc behaviour is computed for a large range of external parameters. The rest of the chapter is dedicated to the validation of the model by comparison with available experimental data.

The last chapter (6) gives a summary of the achievements, its applications and the possible future enhancements of the model.

Die Schwierigkeit in der Bogenphysik liegt heute nicht so sehr in der Ergundung der physikalischen Vorgange, als vielmehr in der quantitativen Erfassung des Zusammenwirkens aller beteiligten Prozesse . . .

H. Maecker 1951

Chapter 2

Conceptual framework for modelling electric arc discharges

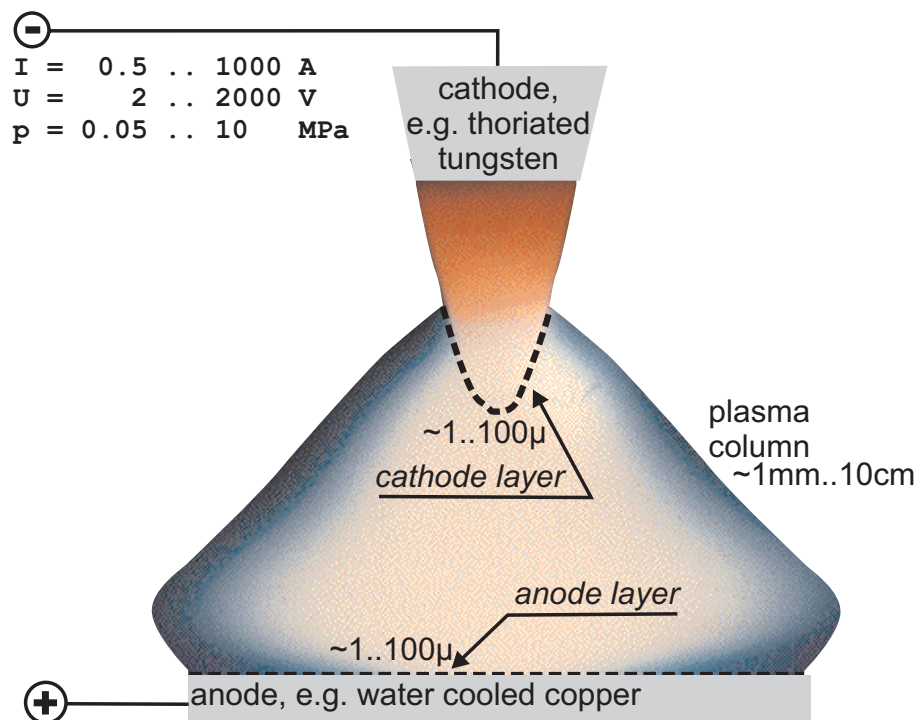


Figure 2.1: Typical electric arc discharge consisting of (solid) electrodes interacting with a thermal plasma through nonequilibrium boundary layers.

The objective of this chapter is to develop the concept for an *ab initio* model of the overall thermal plasma gas discharge behaviour. As sketched in figure 2.1, there are at least three physically different regions:

- The (solid or liquid) electrodes and their surfaces.
- The thermal plasma column and its interaction with the environment and the layers.
- The nonequilibrium boundary layers providing the transition from a solid surface at 1 . . . 4 kK to an (partial) equilibrium plasma at 4 . . . 100 kK.

Looking at the details of these regions, one realizes even finer structures, e.g. the boundary layer split into a space charge *sheath* and ionisation nonequilibrium *presheath*.

As a conclusion, the overall electric discharge system can not be described by a unified mathematical model, or such a model will be useless and untreatable. One has to realize a hierarchy of physical processes occurring in different regions, at different scales and with different relevance to specific features of the discharge. The electric arc is *an arrangement of parts, so intricate as to be hard to understand or deal with – a complex system*. Its behaviour emerges from a self organization of its parts.

For this reason, we have to look at the general behaviour and modelling tasks for general complex systems first, as provided in the next section. Within this framework, in section 2.2 the arc discharge is identified to show the behaviour of a **Complex Adaptive System**.

The specific modelling approaches for the individual arc regions are discussed in section 2.3. Here, we also provide the algorithms required to link physically and numerically different models without losing their individual modelling accuracy. This and alternative approaches are discussed in section 2.3, followed by a summary of the whole chapter.

The overall target is not to develop a model of all possible discharge situations, but to develop a framework which may be regarded as sufficient for some simple arc configurations and open for further improvements. We treat the arc discharge as a *dissipative complex system* and we will get a comprehensive and *simple* picture of some discharges together with the identification of new complex phenomena relevant to others . . . (*just another iteration towards the impossible complete model*).

2.1 Introduction to complex adaptive systems

This section is an adaption of the *arc discharge relevant material* of an introduction provided by Badii and Politi [BP97a]:

Research on complex systems means searching for general patterns in a number of very distinctive systems. Characterizing complexity in a quantitative way is also a vast and rapidly developing field. In general, complexity is not just another phenomenon, it may be regarded as another approach, contradictory to the *reductionist approach* currently used in most areas of science (figure 2.2): Whenever substantial disagreement is found between theory and experiment, the system has been observed with an increased resolution in the search for its *elementary* constituents. Matter has been split into molecules, atoms, nucleons, quarks, thus reducing reality to the assembly of a huge number of bricks, mediated by only three fundamental forces: nuclear, electro-weak and gravitational interactions.

The discovery that everything can be traced back to such a small number of different types of particles and dynamical laws is certainly gratifying. Can one thereby say, however, that one understands the origin of the arc discharge? Well, in principle, yes. One has just to fix the appropriate initial conditions for each of the elementary particles and insert them into the dynamical equations to determine the solution. Without the need of giving realistic numbers, this undertaking evidently appears utterly vain, at least because of the immense size of the problem. An even more fundamental objection to this attitude is that a real understanding implies the achievement of a synthesis from the observed data, with the elimination of information about variables that are irrelevant for the *sufficient* description of the phenomenon. For example, the equilibrium state of a gas is accurately specified by the values of only three macroscopic observables (pressure, volume and temperature), linked by a closed equation. The gas is viewed as a collection of essentially independent subregions, where the *internal* degrees of freedom can be safely neglected. The change of descriptive level, from the microscopic to the macroscopic, allows recognition of the inherent simplicity of this system.

These examples introduce two fundamental problems concerning physical modelling: the practical feasibility of predictions, given the dynamical rules, and the relevance of a minute compilation of the system's features.

In fact, as the study of nonlinear systems has revealed, arbitrarily small uncertainties about the initial conditions are exponentially amplified in time in the presence of deterministic chaos (as in the case of a fluid). This phenomenon may already occur in a system specified by three variables only.

The resulting limitation on the power of predictions is not to be attributed to the inability of the observer but arises from an intrinsic property of the system. In section 2.2, as an example, cathode phenomena in low pressure arc discharges are identified to show such a behaviour.

Nature provides plenty of patterns in which coherent macroscopic structures develop at various scales and do not exhibit elementary interconnections. They immediately suggest seeking a compact description of the spatio-temporal dynamics based on the relationships among macroscopic elements rather than lingering on their inner structure. In a word, it is useful and possible to condense information.

Similar structures evidently arise in different contexts, which indicates that universal rules are possibly hidden behind the evolution of the diverse systems that one tries to comprehend. Many systems can be characterized by a hierarchy of structures over a range of scales. The most strong evidence of this phenomenon comes from the ubiquity of *fractals* (Mandelbrot, [Man82]), objects exhibiting nearly scale-invariant geometrical features which may be nowhere differentiable.

Hierarchical structures appear to be a general characteristic of nature. The difficulty of obtaining a concise description may arise from *fuzziness* of the subsystems, which prevents a univocal separation of scales, or from substantial differences in the interactions at different levels of modelling.

The concept of complexity is closely related to that of understanding, in so far as the latter is based upon the accuracy of model descriptions of the system obtained using a condensed information about it. Hence, a *theory of complexity* could be viewed as a theory of modelling, encompassing various reduction schemes (elimination or aggregation of variables, separation of weak from strong couplings, averaging over subsystems), evaluating their efficiency and, possibly, suggesting novel representations of natural phenomena. It must provide, at the same time, a definition of complexity and a set of tools for analysing it: that is, a system is not complex by some abstract criteria but because it is intrinsically hard to model, no matter which mathematical means are used. When defining complexity, three fundamental points ought to be considered:

1. Understanding implies the presence of a *subject* having the task of describing the *object*, usually by means of model predictions. Hence, complexity is a *function* of both the subject and the object.
2. The object, or a suitable representation of it, must be conveniently divided into *parts* which, in turn, may be further split into subelements, thus yielding a *hierarchy*. Notice that the hierarchy need not be manifest in the object but may arise in the construction of a model. Hence, the presence of an actual hierarchical structure is not an infallible indicator of complexity.
3. Having individualized a hierarchical encoding of the object, the subject is faced with the problem of studying the *interactions* among the subsystems and of incorporating them into a model. Consideration of the interactions at different levels of resolution brings in the concept of *scaling*. Does the increased resolution eventually lead to a stable picture of the interactions or do they escape any recognizable plan? And if so, can a different model reveal a simpler underlying scheme?

2.1.1 Complexity measures

After observing a new phenomenon, research initially attempts to find a quantitative measure for it. For complexity this is historically strongly related to discrete mathematics, coding and compression theory. Details may be found in the literature [BP97a, SST90]. For our discharge modelling context, a specific meaning of the complexity measures is proposed as follows:

- Algorithmic complexities:
 - Algorithmic Information Content, Lempel-Ziv complexity or randomness:
The amount of modelling software (typically $10^{4..6}$ lines of code) required to get the results on one hand, and the compressability (the modelling data compressability by standard methods is larger for more simple discharge configurations) of the results on the other hand.
 - Logical depth: *The computing time (typically more than 10^{11} floating point operations).*
 - Sophistication: *The modelling and numerical concepts and the management of their realization.*
 - Grammatical, regular language and set complexities:
The programming concepts and languages used.
- Hierarchical scaling complexities:
The physical submodels and their interaction.

In the long term, the historical development of discharge models is clearly attracted towards descriptions with balanced complexity. In the short term, the development follows the path of least resistance, where increasing logical depth is simple and increasing sophistication is most difficult.

Before affordable high performance computers emerge in the 1980'ties, the development was focused on the mathematical description of specific physical processes relevant for specific arc configurations or regions. Obtaining numerical solutions was possible for highly simplified models only. Nowadays, special care has to be taken, when using measured quantities (like plasma conductivity) obtained using oversimplified discharge models.

2.1.2 Emergence: self generated complexity

We speak of self-generated complexity whenever the (infinite) iteration of a few basic rules causes the emergence of structures having features which are not shared by the rules themselves. Simple examples of this scenario are represented by various types of symmetry breaking (superconductors, heat convection) and long-ranged correlations (phase transitions, cellular automata). The relevance of these phenomena and their universal properties discovered by statistical mechanical methods indicate self-generation as the most promising and meaningful paradigm for the study of complexity. It must be remarked, however, that the concept of self-generation is both too ample and too loosely defined to be transformed into a practical study or classification tool.

In any case, two extreme situations may occur: the model consists either of a large automaton, specified by many parameters, which achieves the goal in a short time, or of a small one which must operate for a long time. Consequently, the complexity of the pattern is often visualized

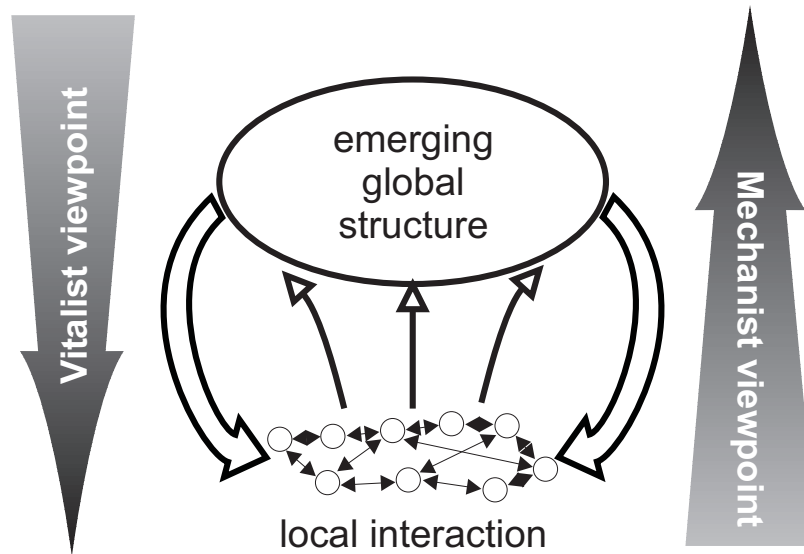


Figure 2.2: The emerging system properties *replace* the inability of the observer to *understand* the system in the classical (reductionism) sense.

either through the size of the former automaton or through the computing time needed by the latter.

Another aspect of the problem emerges, namely, that complexity is associated with the disagreement between model and object rather than with the size of the former. This, in turn, calls for the role of a subject (the observer) in determining the complexity itself through its ability to infer an appropriate model. Of course, a system look: complex as long as no accurate description has been found for it.

These considerations and the limited domain of applicability of all existing complexity measures strongly suggest that there cannot be a unique indicator of complexity, in the same way as entropy characterizes disorder, but that one needs a set of tools from various disciplines (e.g. plasma physics and computer science) and – of course – a significant amount of manpower and computer capacity. As a result, complexity is seen through an open-ended sequence of models and may be expressed by numbers or, possibly, by functions. Indeed, it would be contradictory if the *complexity function*, which must be able to appraise so many diverse objects, were not itself complex!

As sketched in figure 2.2, the global structure of a system is not unidirectional determined by the local interaction of its parts. The global structure may change local interactions. The objective of this work is not to change the viewpoint from reductionism (*escape into detail*) to holism (*ignore the detail*), but to apply both approaches as they are two sides of the same medal.

2.1.3 Is the arc discharge a complex system?

The electric arc discharge is driven by an external supply of electrical energy and permanently exporting heat and radiation to its environment. The plasma electrode system is far from

thermodynamic equilibrium and exporting entropy. The discharge process is irreversible and can become chaotic. The distribution of the hot spots across the electrode surface or the discharge itself can show a fractal nature [FNT93]. As shown in the next chapter, the effective number of degrees of freedom can be reduced by exploiting its hierarchic structure. Such far-from-equilibrium systems manifest self-organization (synergetics). There are mathematical concepts for analysing time series data or nonequilibrium phase transitions by analytical methods [HV97]. In this work, there will be no attempt to extend these concepts to an only numerically treatable hierarchical system like thermal plasma gas discharges. An analytical treatment of the emerging discharge properties and thus the application of existing synergetic concepts is assumed to be possible by changing the type of the model from *ab initio* to *heuristic*. A complex adaptive or self organizing system is not a mathematically well defined object. The arc discharge simply gets this characterization by another complex adaptive system – the human researcher investigating it. By accepting the complex details and their emerging properties, an increased understanding will finally allow the reader to characterize the arc as a *less* complex system.

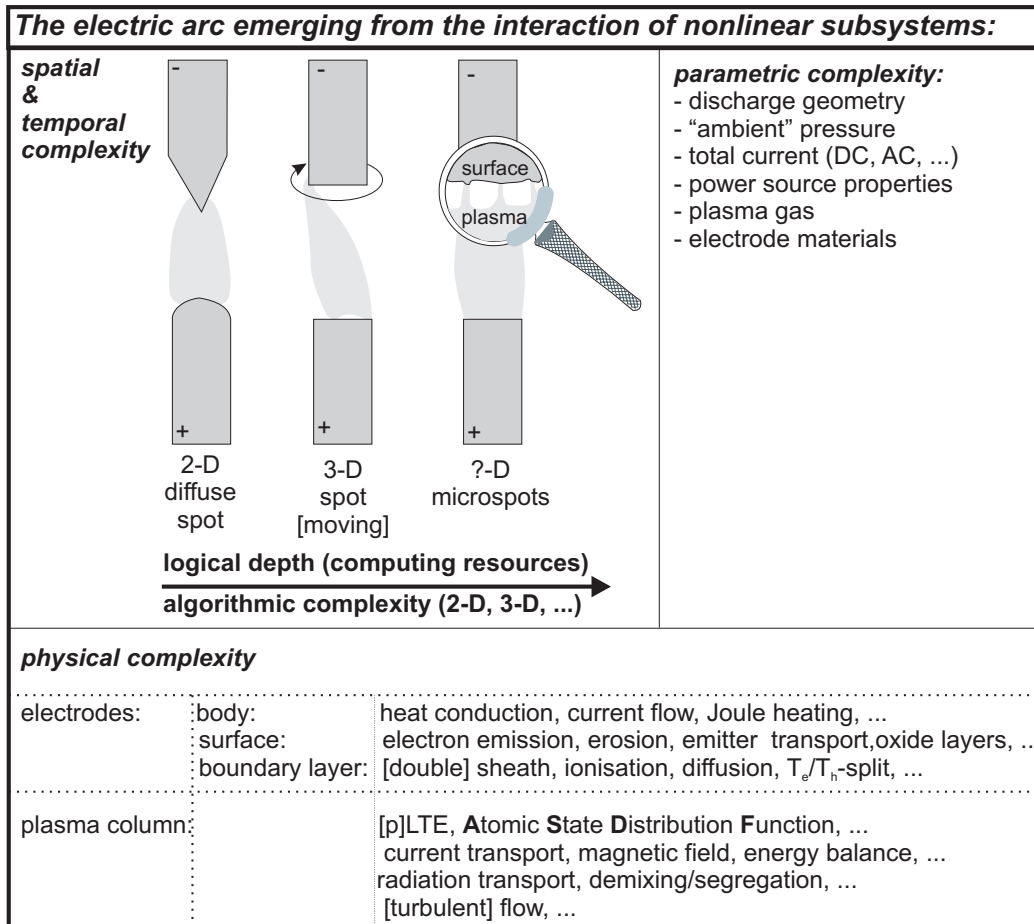


Figure 2.3: The different levels of complexity emerging in electric arc discharges.

2.2 The overall behaviour of arc discharges

Now, we are prepared to realize the different levels of complexity appearing within the parameter range of high intensity gas discharges. This will enable us to define the arc systems predictable by actual modelling concepts (section 2.3) and possible extensions for the future.

In figure 2.3, the different levels of complexity emerging in high intensity gas discharges are sketched. The physical details and models for them are discussed in chapter 3, here we discuss the three major spatial and temporal appearances of the overall discharge:

1. Stationary discharge in cylindrical symmetry:

This kind of discharge appearance can be found in Tungsten Inert Gas welding arcs [Ols59, HEP83, Tho93] and high pressure lamps [Hop87]. Such configurations are under investigation within current modelling attempts (see chapter 5). The cathode material should be *refractory* (i.e. not evaporating) and with homogenous emission properties. The electrode geometry must be properly selected (e.g. tipped and/or rounded). Stabilization to cylindrical geometry is provided by magnetic compression, electrode geometry or outer walls. There will be a single hot spot at the electrodes, often called *diffuse*. Variation of total arc current may lead to a sudden change of the total spot area, a *mode transition*. The smaller hot spot area mode is called *spot mode*.

2. [Quasi]Stationary non symmetric discharge:

Using geometrically problematic electrode configurations (e.g. an unrounded stick electrode) will force the discharge to break cylindrical symmetry. Lower currents support for that by decreasing magnetic compression. Higher currents or hollow electrodes may lead to rotation of the hot spot, as found in arc gas heaters [SMB97].

3. Transient non symmetric discharge:

Decreasing discharge pressure, the arc starves for ionizable material. Decreasing current provides less heating and thus less electron emission in the normal hot spot mode. The system reacts by forming a variety of smaller and smaller cathode spots on different time and length scales. Additional support for such microspot formation comes from spatial or temporal inhomogeneities of the electrode surface, or such inhomogeneities result from burning the discharge for a significant time. Over the years, increased experimental resolution support the assumption of some fractal regimes of cathode spot formation (both in time and space).

Finally we arrive at the vacuum arc with its characteristic transient and non-symmetrical behaviour [Kim74, KPS94, Rak87, Jüt97].

Additionally, some important facts have to be accepted:

- The arc appearance (1-3) depends on all major parameters stated in figure 2.3.
- There are some plausible rules (see above), but prediction of arc appearance for a specific configuration will require models suitable for all possible symptoms.
- It will be a positive quality factor, if e.g. a 2-D stationary model will fail to deliver results for a configuration showing only 3-D instationary arc appearances.

- Deviations of the experimentally realized configuration from the anticipated idealized state may totally hide any other parameter dependencies one tries to observe (e.g. the cathode surface exhibits an inhomogenous work function distribution with dramatic impact on the discharge appearance).
- Discharges may be similar, but not because of the agreement of some external parameters, but because of similar physics and symmetry.

As a rule of thumb, the arc reacts on *harder* burning conditions with increased spatial and temporal complexity. The prediction of *optimum* burning conditions allowing for stationary cylindrical symmetric discharges is one of the objectives of this work.

2.3 Numerical modelling concepts

A physical self consistent description of the overall discharges (as described in chapter 3) needs to be based on a numerical solution concept, which is realistic in terms of development and computing time (algorithmic complexity and logical depth).

Modern methods of scientific computing have to be evaluated with respect to availability, costs and numerical effort. For electric arc modelling, the plasma is described as a conducting fluid. Mainly the concepts of **Computational Fluid Dynamics** (CFD) have to be applied. Because of its tremendous complexity and the amount of practical experiences needed for an understanding of such concepts, the following section can provide a summary only. Understanding will require at least the knowledge of the basic concepts as described in standard textbooks [Pat80, FP99, ADDG92, ZT91].

Regarding the numerical solution of the mathematical plasma electrode model, two different approaches are currently in use:

1. The discharge geometry is divided into finite volumes using a non equidistant grid spacing and volume boundaries perpendicular to the spatial coordinates $\{r, z\}$ (BS, left part of figure 2.4).
2. The computational region is divided into a solution adapted finite element grid based on triangles. (LTI, right part of figure 2.4) [Wie98, FWN00].

In their current implementation (BS: this work, LTI: [Wie98, FWN00]), both concepts have their specific drawbacks.

The orthogonal structured grid of the BS concept wastes a lot of grid volumes because the refinement depends only on the r and z coordinate. A solution adaptive refinement is implemented for the finite volume method by commercial CFD-codes (unstructured grids). The present approach was selected in order to limit code development time to a few years and because of the straightforward fluid flow implementation as described by Patankar [Pat80]. Similar numerical concepts were implemented at CNRS/ENSCP in France [DS90], CSIRO in Australia [ZLM92, LMH97], at UMN/ME in the USA [Hsu82, HP83b] and several other groups.

The finite element arc modelling approach (LTI) is described in detail by Wiesman [Wie98]. There is no inclusion of fluid flow phenomena in this implementation. The major drawback is not a numerical one, it is a result of the physical model used by the LTI approach. The neglect of one dimensional sheath effects and the description of the non equilibrium electrode layers by a 2D model implies the requirement for a very fine numerical mesh near the electrodes

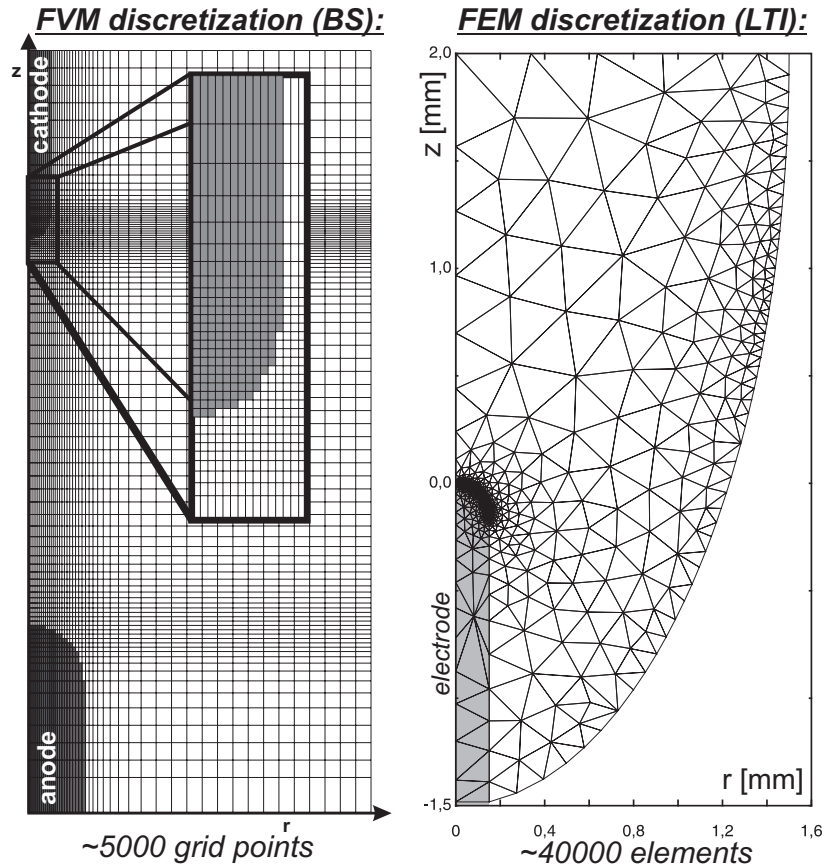


Figure 2.4: Finite volume (this work, Braunschweig: BS) and finite element (Lichttechnisches Institut, Karlsruhe: LTI) grids used for complete arc discharge modelling (only one half of the FEM grid is shown).

(see figure 2.4). The mesh elements scale down to a nanometer scale leading to a very large number of finite elements.

Both implementations (LTI and BS) may be regarded as less professional than commercial CFD/FEM software packages, but they allow for the prediction of electric arc behaviour, while commercial packages actually do not support this application.

In the future, easy to use and efficient arc modelling should be based on such commercial tools. The problem of these large codes is the unavailability of the sources and their algorithmic complexity (more than $10^5 \dots 10^6$ lines of code compared to the several 10^4 lines developed at LTI and BS). For the development of the basic technology, the test and evaluation of new physical concepts and in order to have development times of only several man years, only concepts like those realized by this work and the groups cited above, are realistic. The following section will provide a summary of the general numerical concept for electrode plasma linkage (*transfer function*) developed within this work.

The orthogonal FVM discretization used for this work was selected for a maximum efficiency in code development time. This work is focussing on the investigation of physically self con-

sistent and accurate cathode and anode layer models within the framework of a self consistent calculation of the overall arc discharge including convection effects.

2.4 The transfer function concept

The basic algorithm for solving coupled fluid flow and heat transport problems by the finite volume method is perfectly described by Patankar [Pat80]. The early implementations of this approach for an overall arc electrode model by a so-called *conjugate heat transport* method can be found in the literature [LMH97, ZLM92]. The solution of the 2D plasma equations (electric potential, flow- and temperature-fields) as well as the heat (and current) transport inside the electrodes can directly follow the Patankar approach. His method solves a system of equations of the type

$$\frac{\partial}{\partial t} (\rho\Phi) + \vec{\nabla} \cdot (\rho\vec{v}\Phi) = \vec{\nabla} \cdot \Gamma_{\Phi} \vec{\nabla} \Phi + S_{\Phi} \quad (2.1)$$

to which the set of arc plasma equations can be reorganized, e.g. (see section 3.5):

physical quantity	Φ	Γ_{Φ}	Source S_{Φ}
mass	1	0	0
axial momentum	u	μ	$-\frac{\partial p}{\partial z} + \frac{\partial}{\partial z} \left(\mu \frac{\partial u}{\partial z} \right) + \frac{1}{r} \frac{\partial}{\partial r} \left(\mu r \frac{\partial v}{\partial z} \right) + j_r B_{\Theta}$
radial momentum	v	μ	$-\frac{\partial p}{\partial r} + \frac{\partial}{\partial z} \left(\mu \frac{\partial u}{\partial r} \right) + \frac{1}{r} \frac{\partial}{\partial r} \left(\mu r \frac{\partial v}{\partial r} \right) - \mu \frac{2v}{r^2} - j_z B_{\Theta}$
energy	h	$\frac{\kappa}{c_p}$	$\frac{j_r^2 + j_z^2}{\sigma} - S_R + 5/2 \frac{k_b}{c_p e} \left(j_z \frac{\partial h}{\partial z} + j_r \frac{\partial h}{\partial r} \right)$
electric potential	Φ	σ	0

The major problem of the numerical concept is the development of a physically realistic and treatable boundary layer algorithm. In front of the electrodes, sheath effects occur (see chapter 3) and these are very difficult to implement into a 2D model. Because the size of the nonequilibrium layer is only about 10 μm (or even a few nanometers if the space charge layer is regarded as the boundary layer only), it can be treated as a 1D-layer forming a skin in front of the electrodes.

The finite volumes in front of the electrodes (resulting from the 2D meshing) require special attention. A numerically stable approach is to use a 1D layer model for the calculation of the *effective* electric and heat conductivity (figure 2.5). The result is a non smooth electric conductivity at the plasma electrode interface (figure 2.6). Negative anode sheath voltages (as resulting from the model described in the next chapter), will give even negative electric conductivities and can imply some numerical problems.

The effective conductivity approach works fine for some high current atmospheric argon arcs (see section 5.3.6), but it is not very realistic. Therefore the problem was generalized and found to be a special case of a general iterative scheme for the calculation of related boundary conditions for multidimensional regions linked by surfaces with additional physical processes to be modelled. This so called *transfer function* approach (figure 2.7) is very general and may also be used for other application areas or numerical schemes.

It is straightforward to get solutions for partial differential equations defined on multidimensional regions with well defined boundary conditions. Thus the electrode plasma system has to be divided into the 2D arc plasma and 2D electrode solid regions. The boundary conditions used for the 2D solutions are heat flux and voltage or current density. The layer between these regions is regarded as a black box *transferring* actual plasma and solid surface parameters to

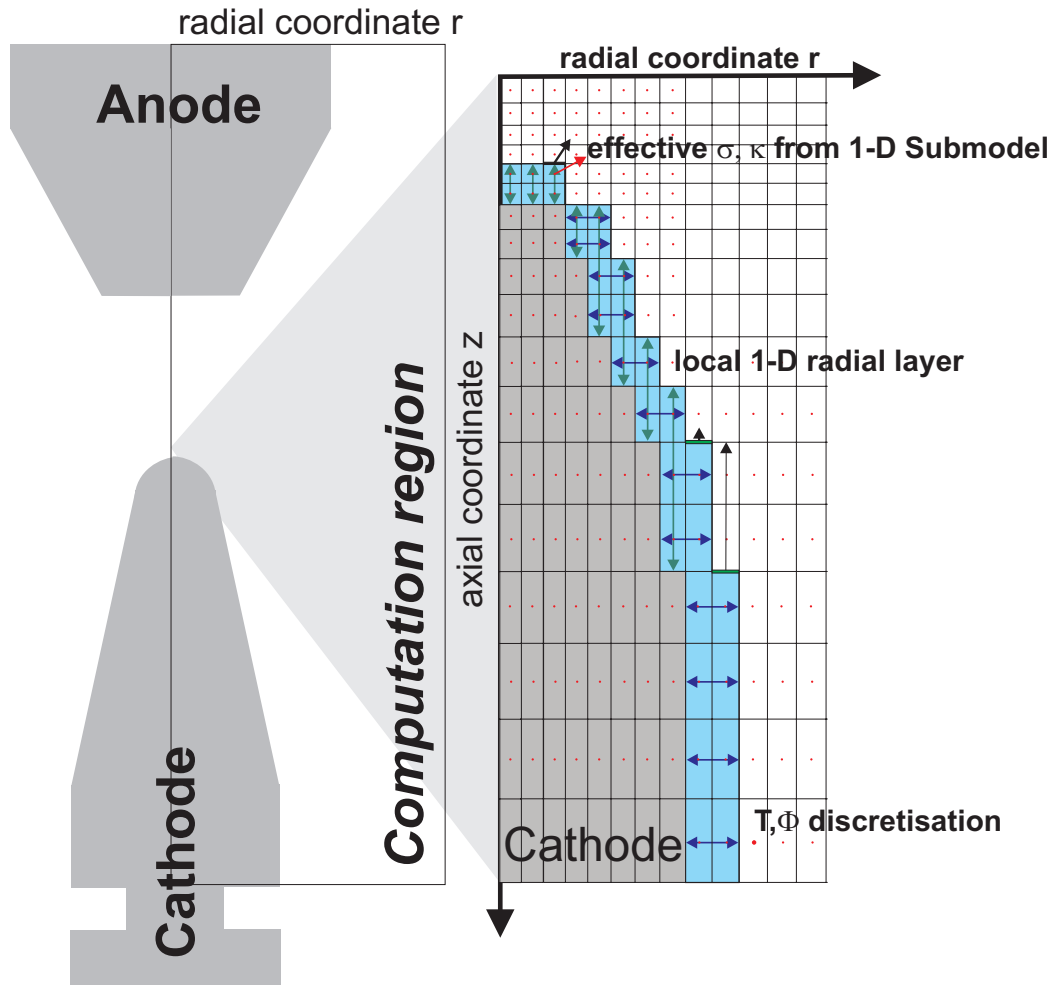


Figure 2.5: Integration of local 1-D sublayer models by the effective conductivity approach.

new boundary condition values for the next iteration step. As a result, the multidimensional regions are linked by a general scheme allowing for an implementation independent of a specific physical model of the processes inside the layer. It is a local concept allowing for a variation of the layer parameters and boundary conditions along the electrode surfaces. Regarding the plasma and solid heat balances, it simply transfers current values of the local plasma and surface temperatures to new heat flux boundary conditions.

2.5 Summary of the concept

As a matter of fact, electric arc discharges are not homogenous physical systems allowing for a description by a single set of equations. The internal boundaries between regions of different physical provenience and the long range interaction of the discharge parts form a self-organizing complex system. In the next chapter, the physical processes governing the individual regions

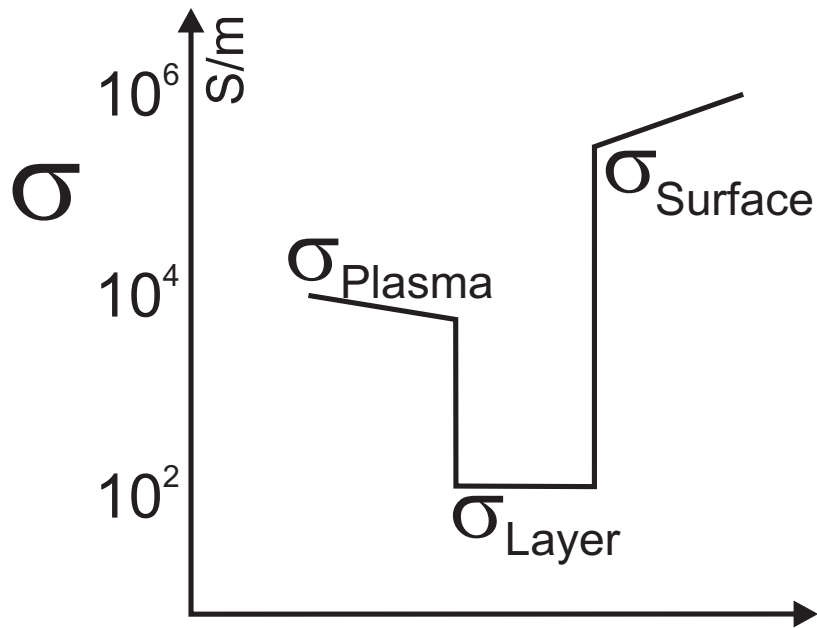


Figure 2.6: Electrical conductivity within the thermal plasma cathode system.

will be described by mathematical modelling. The numerical linkage of the regions is sketched in this chapter. Finally the software implementation of this concept will deliver a computer model allowing to predict most of the characteristic features of the electric arc discharge. Through the emergence of more and more complex structures resulting from specific operating conditions and depending on discharge pressure, electrode geometry and discharge medium, the real arc may be still regarded as unpredictable for a randomly chosen configuration. But the remainder of this work will show the predicablity of a large class of discharge parameters: the stationary, radial-symmetric electric arc.

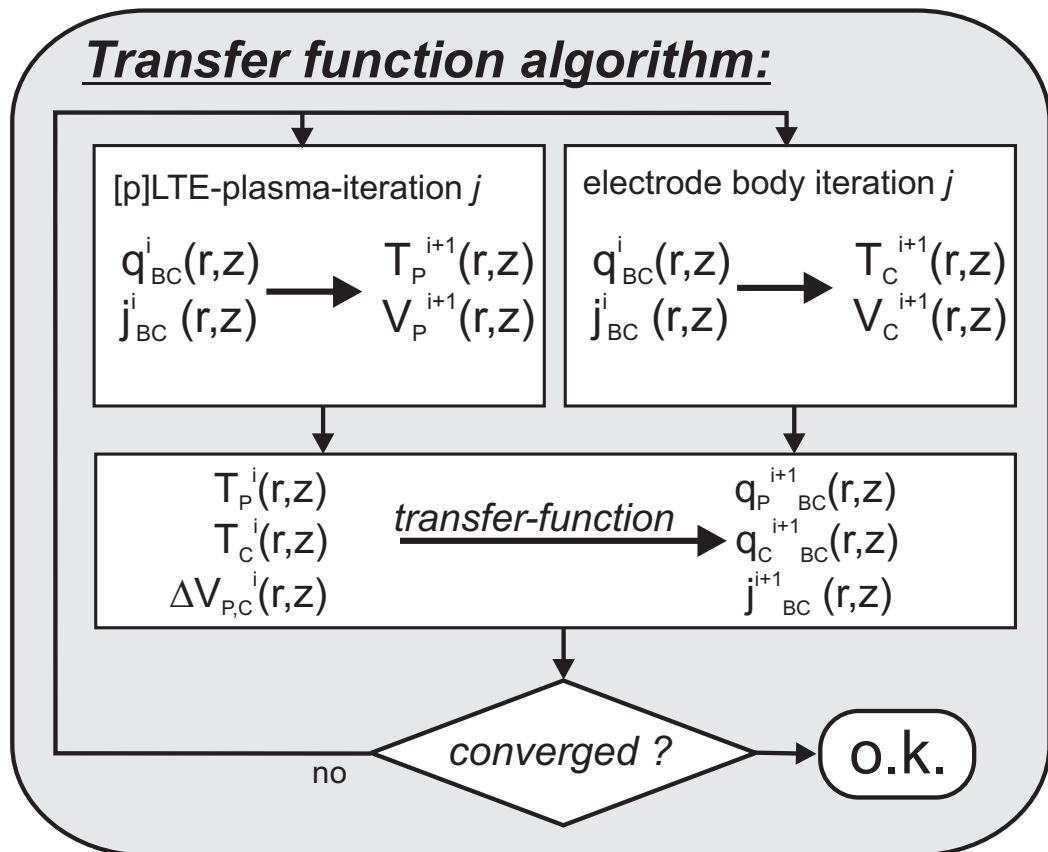


Figure 2.7: Transfer function algorithm (see text).

Das Ganze existiert aufgrund seiner Teile, und die Teile wiederum existieren wegen des Ganzen, um das Ganze zu erhalten. I. Kant

Chapter 3

Physics of the electric arc discharge

3.1 Introduction

The overall aim of this chapter is to develop a numerically treatable *ab initio* model for a (large) class of thermal plasma gas discharges. Such electric discharges are also called electric arcs. Within the variety of gas discharges, the electric arc is defined by the following typical behaviour:

- The discharge is self-sustaining with a relatively low voltage caused by a cathode fall voltage of only several volts and a high conductivity of the thermal plasma in the column.
- Special discharge ignition techniques like high voltage pulses, short circuit or the increase of pressure at constant current are generally needed.
- The cathode is at thermionic emission temperatures provided by the energy flow from the near cathode plasma or external heating.
- The current density in the cathode hot spot is 100-1000 times that of the corresponding glow discharge.
- The total discharge current is always above the corresponding glow discharge current (figure 3.2). There is a non-smooth transition from glow to arc with increasing current.

An introductory discussion of the different types of arc discharges can be found in the literature [Rai91, FM57]. Not all of them are treatable by the model described in this chapter or even any *ab initio* model to be developed in the near future. The model does not attempt to describe non-stationary multi-cathode-spot discharges (like vacuum arcs). Nevertheless, it can deliver the physical basis for future attempts to predict alternating current (AC) arcs used for lighting or welding.

3.1.1 Basic discharge features

As sketched in figure 3.1, a typical arc discharge consists of a (highly luminous) plasma column linked to the electrodes by small (skin like) non equilibrium layers. The basic arc behaviour observed experimentally and discussed in the following sections will be predictable by the quantitative *ab initio* model developed in this chapter.

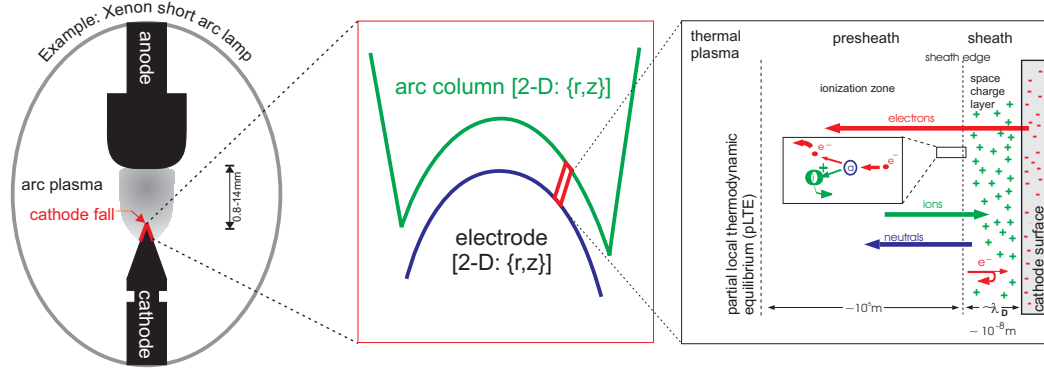


Figure 3.1: Scheme of an arc discharge.

3.1.1.1 Arc stabilization

In order to obtain numerical solutions for the model developed within this chapter, the arc discharge has to be stationary and cylindrical symmetric. Most practical applications require such stable burning conditions which are realized by the following means:

- The arc column is confined, i.e. by a quartz or alumina tube with a radius not larger than the natural arc radius, e.g. most HID-lamps, where the electrode separation is much larger than the electrode diameter.
- The arc is stabilized by the electrodes, i.e. the high current densities of the cathode and anode hot spots generate high magnetic compression forces. The resulting expansion jets dominate the arc flow field and temperature map stabilizing the overall discharge against external perturbations (e.g. in high pressure short arc lamps).
- The arc is stabilized by natural convection, e.g. the horizontally burning arc in air.

3.1.1.2 Current voltage characteristics

As shown in figure 3.2, the arc discharge is distinguished from the glow discharge by much lower voltages at higher current. The transition from glow to arc is in general non-smooth. The current voltage characteristics of the arc is generally falling. Above a certain current (about 10 times the glow to arc transition current), the variation of the cathode fall is rather small. The anode fall voltage is nearly constant with current. The following model will allow for the calculation of all these voltage variations.

3.1.1.3 Arc column properties

As shown in figure 3.3, the temperature profile in the column of (long) arc discharges is almost parabolic. Deviations of electron and heavy particles temperatures can be located (at least) in the arc fringes.

The electric field in the column of arc discharges is much lower than in glow discharges. This is due to the different ionization mechanisms. In the kinetic regime of the glow discharge plasma, the electric field must deliver electron energy up to the region of the ionization energy (E_{ion}), while in the equilibrium arc discharge, the ionisation is due to the high energy tail of the

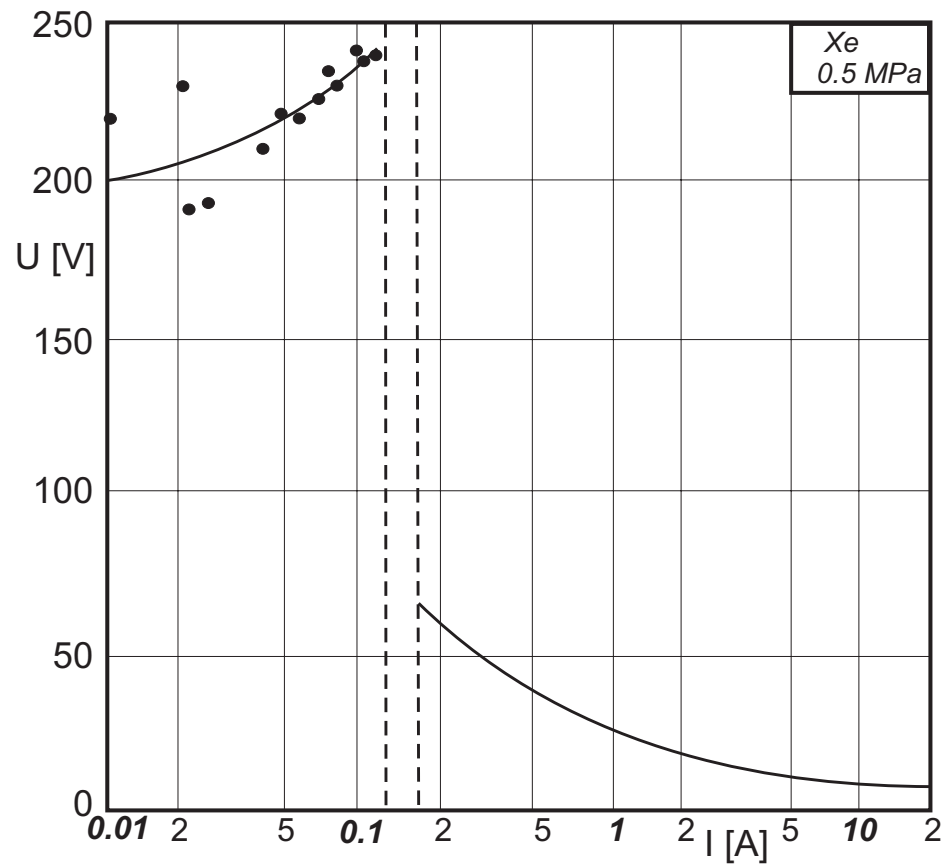


Figure 3.2: Voltage-current characteristic of a xenon lamp in the transition from glow to arc discharge [Mae51].

electron energy distribution function, thus the electric field must only deliver electron energy of $k_b T_e \ll E_{\text{ion}}$.

As shown in figure 3.4, the electric field in the center of the arc discharge increases with total discharge pressure (the mean free path to gain energy from the electric field decreases with increasing pressure) and the total current (heat loss by conduction, radiation and convection).

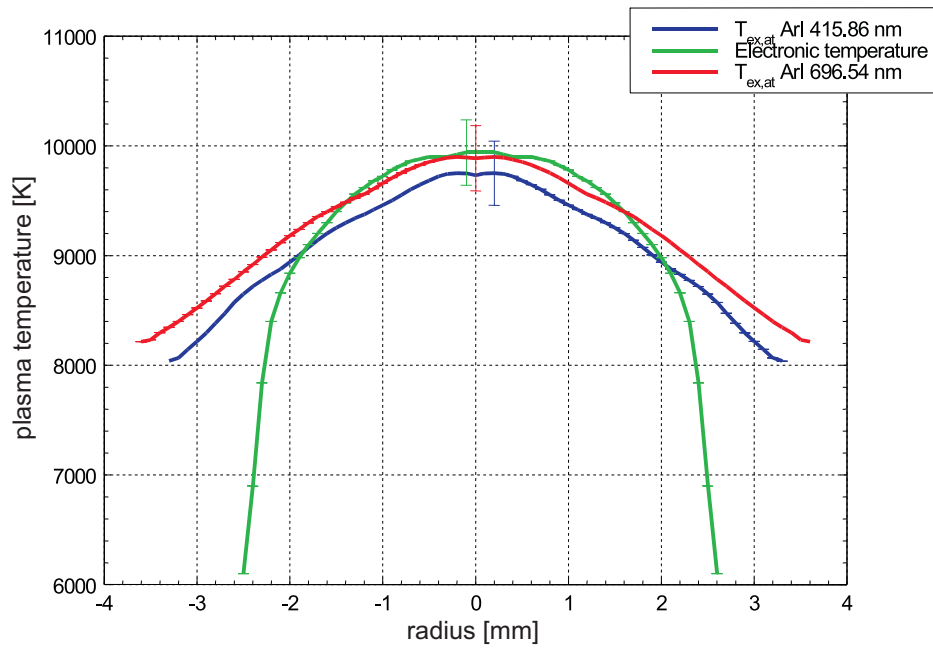


Figure 3.3: Measured plasma temperature distribution in the column of an atmospheric argon arc ($I = 30\text{A}$) [BCP99].

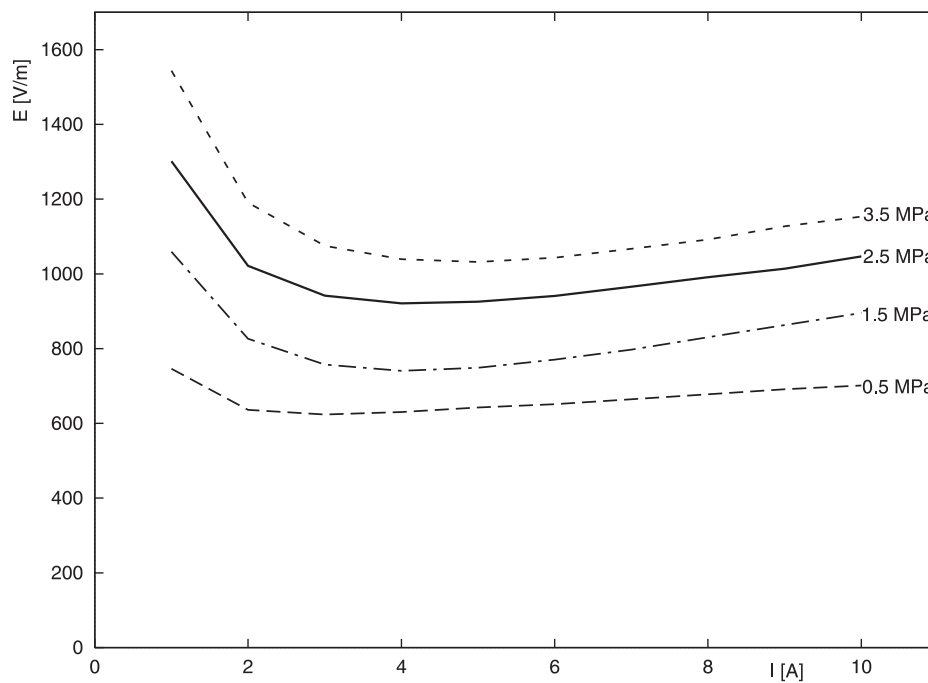


Figure 3.4: Measured electric field in the column of high pressure xenon arcs [BS54].

3.1.1.4 Cathode hot spot and fall voltage

Glow discharges need a high cathode voltage drop, because the electrode is not at thermionic emission temperatures. The ions are accelerated in the cathode fall in order to provide an electron current sustained by secondary emission from the cathode surface.

The cathode voltage drop of the arc discharge is much smaller and its task is to heat the cathode surface to thermionic emission temperatures and to accelerate the emitted electrons for gaining energy needed for ionization within the near cathode plasma layer. Below a certain saturation current, the cathode fall voltage strongly depends on total arc current and decreases with increasing pressure.

As an example, the strong current dependencies of the arc voltage, cathode- and anode fall voltages for a low current non LTE arc are plotted in figure 3.5. It can be seen, how the cathode heating required to reach thermionic emission temperatures is provided by the increasing fall voltage (located in the space charge layer) for total arc currents below 10A.

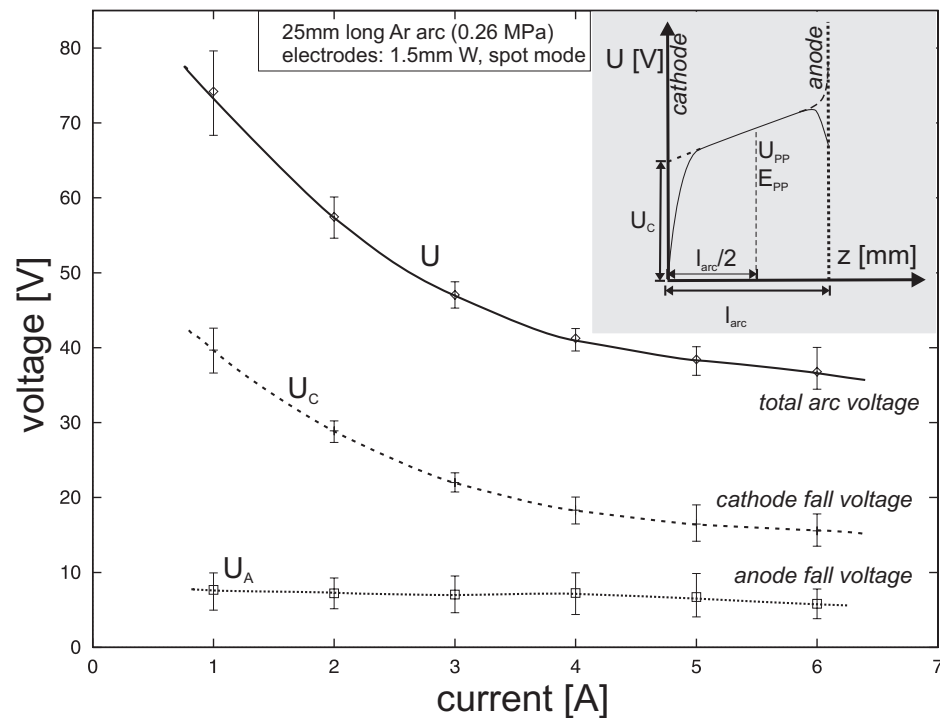


Figure 3.5: Measured total, cathode- and anode-fall voltage of a low current 0.26 MPa argon arc plotted against total arc current [LNBM99].

3.1.1.5 Anode hot spot and fall voltage

Analogous to the situation at the cathode, the anode attachment can be diffuse, i.e. the current is spread over a relatively large area at a density of about $10^{5\cdots 7}$ A/m². The energy flux densities are not very high compared to the spot mode and the material erosion is small as long as the evaporation temperature of the anode material is not reached.

If the increasing current is forced to occupy the edges or the anode surface structure is non-homogenous, the current density can increase locally by several orders of magnitude forming a single or numerous small hot spots.

Again, directly in front of the anode surface, a small space charge layer develops. If there is no need to supply additional energy for sustaining the electron current, i.e. the current density is below the electron saturation current density of the undisturbed column plasma, the fall voltage becomes negative.

In the case the anode surface area is smaller than the cross section of the column, there is also a plasma constriction near the anode resulting in an additional geometric fall voltage.

In most cases, the anode fall voltage does not vary appreciably with total discharge current (see figure 3.5).

3.1.2 Modelling tasks

In order to reproduce the basic features summarized above and to get accurate modelling software, at least the following physical phenomena have to be included in the discharge model:

1. Heat conduction within the (solid) electrodes.
2. Electron emission from the cathode surface.
3. Electrical and thermal transition from the electrode surface to the (equilibrium) thermal plasma.
4. Current and heat transport within the arc plasma column (plasma description as a conducting fluid).
5. The symmetry of arc discharges is at least cylindrical
 - an overall one-dimensional description is not possible.

As elaborated in the following sections, there are different models for different regions of the arc plasma. Very thin (skin like) non equilibrium layers in front of the electrodes are of special importance for the existence and formation of the arc itself. At least one of these layers, the space charge sheath, is small enough to be treated one-dimensional. Summarizing the results, the overall arc discharge model will consist of three sub-models linked by an iterative procedure:

- 2-D description of the heat conduction within the electrodes: section 3.2.
- 1-D description of the cathode sheath and presheath: section 3.3.
- 2-D description of the arc plasma (current transport, heat and fluid flow): section 3.5.
- 1-D description of the anode sheath and presheath: section 3.4.

Within the iteration algorithm, the data of the plasma and electrode surface is *transferred* to new boundary conditions for the next iteration cycle. The concept is thus called *transfer function approach* (see section 2.4). This approach can be implemented into the numerical simulation software independently of the specific details of the layer (1-D) or plasma/electrode (2-D) modelling and independent of the numerical procedures to be used for the 2-D regions (like finite volume or finite element methods).

3.2 Physical processes inside the electrodes and at the electrode surface

The electrodes are heated within a small current-carrying area, the so-called hot spot. This heat load is dissipated by conduction and thermal radiation of the surface. These losses and sources are boundary conditions for the heat conduction equation to be solved within the electrodes:

$$\rho c_p \frac{\partial T}{\partial t} = \vec{\nabla} \cdot [\lambda(T) \vec{\nabla} T] + \frac{\vec{j}^2}{\sigma(T)} .$$

The Joule heating term was included into the calculations, but was found to be negligible for most high pressure discharge situations, while it becomes important for very high current densities.

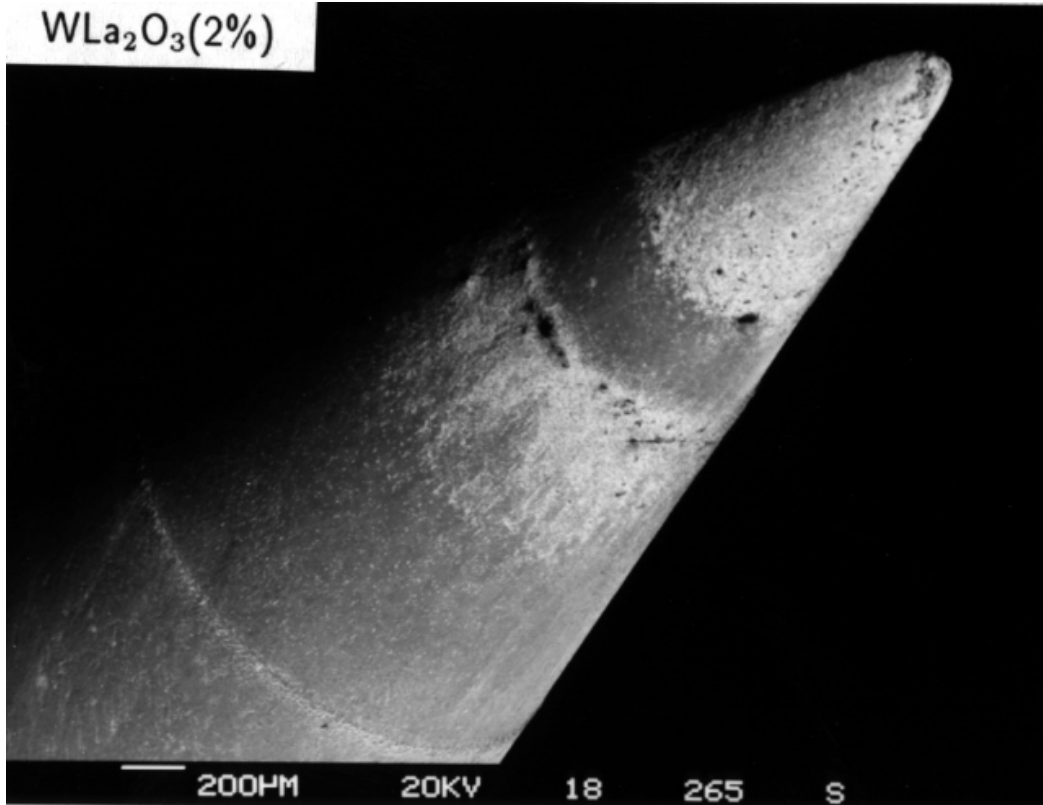


Figure 3.6: Cathode tip of a 200A welding arc.

A typical welding cathode tip is shown in figure 3.6. The active (electron emitting area) is easy to identify, because the electrode surface is influenced by the high heat loads during arcing. Because electron emission workfunction is one of the most important electrode material parameters, real electrodes are often doped with low workfunction materials. As a consequence, surface and bulk diffusion of the emitter material [Sel97] becomes important for the overall discharge behaviour and cathode lifetimes. Such non homogenous surface states imply spacially non uniform thermal radiation emissivities and work functions. In principle, the local radiation emissivity and electron emission work function therefore depends on local temperature and electrode composition. For a detailed investigation of the cathode surface structures and processes see [Sch99].

The heat and electric conductivity of typical electrode materials are plotted in figure 3.7. They are several orders of magnitude larger than the plasma conductivities. As a conclusion, current transport within the electrodes is not important for the overall discharge behaviour, while electrode geometry and heat conductivity significantly influences the hot spot formation at the cathode and thus the cathode fall voltage.

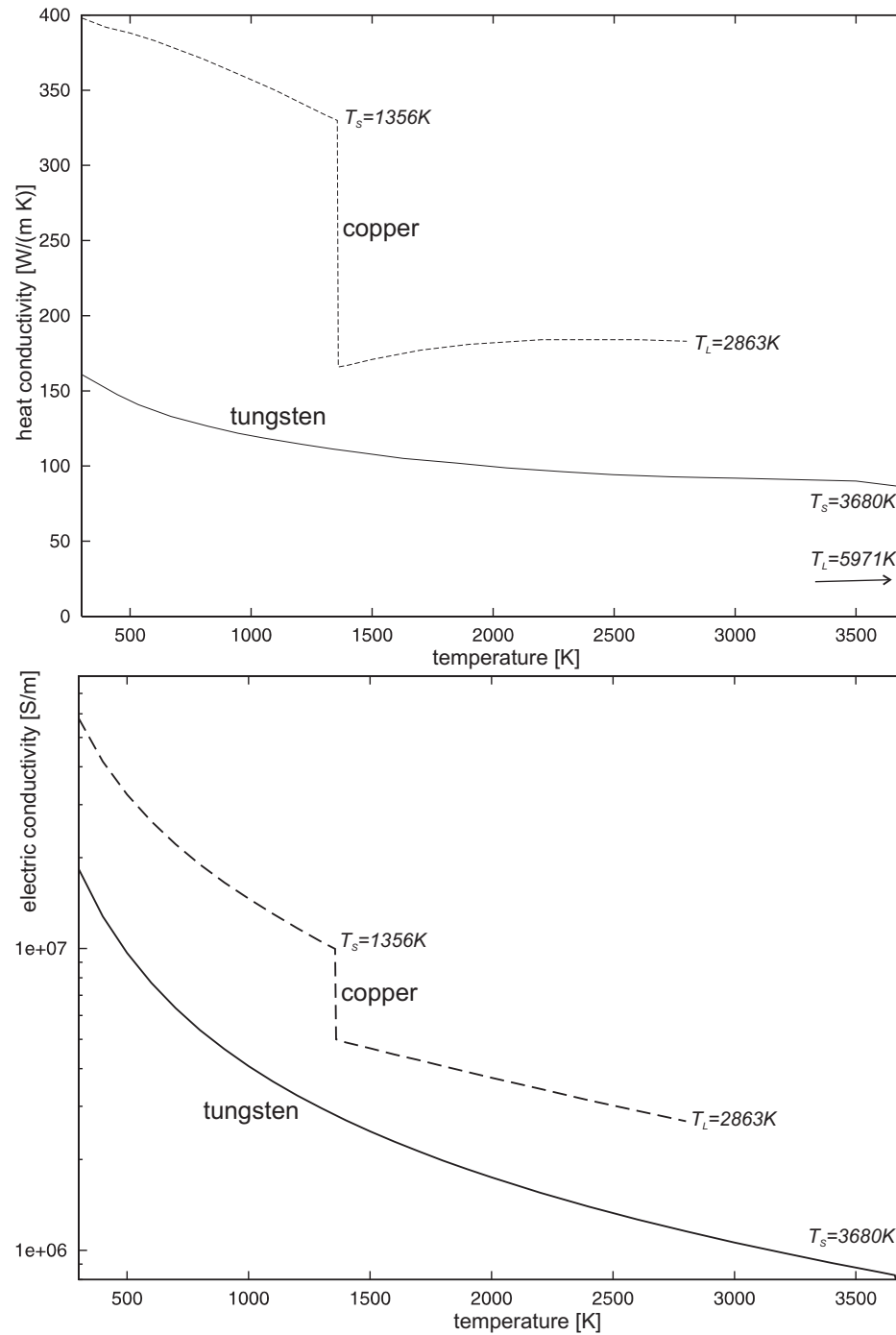


Figure 3.7: Electric and heat conductivity of copper and tungsten (T_s =melting temperature, T_L =evaporation temperature).

3.3 The cathode–plasma transition layers

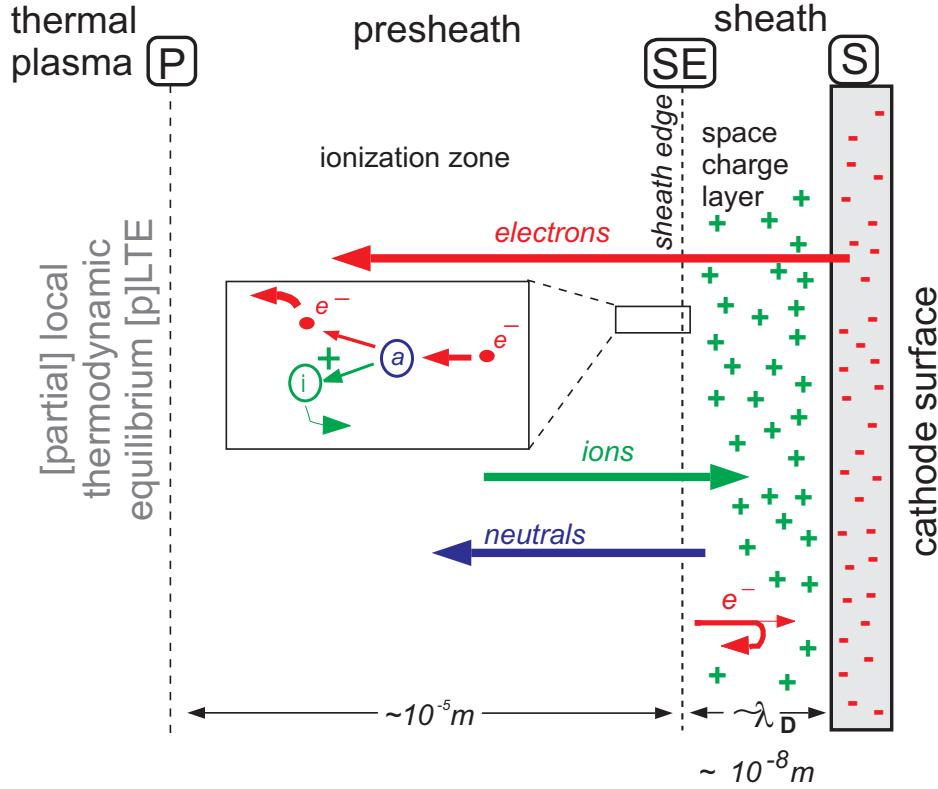


Figure 3.8: Physical processes inside the cathode layer.

As discussed above and sketched in figure 3.8, the transition from the electron emitting cathode surface to a plasma in (partial) LTE can be further divided into a space charge layer (sheath) and an ionization layer (presheath). The interface between the thermal plasma and the presheath is associated with the subscript P, physical quantities at the sheath-presheath interface will be identified by the subscript SE, surface quantities by the subscript S. The sheath and presheath sublayers and their linkage are described in the following sections.

3.3.1 Electron emission of the cathode surface

The local electron emission of the cathode surface depends on the local surface temperature T_S and the material property *work function* Φ . It is given by the Richardson emission formula [Ric03]:

$$j_{\text{RS}} = A_{\text{R}} T_{\text{S}}^2 \exp\left(-\frac{\Phi_{\text{eff}}}{k_{\text{b}} T_{\text{S}}}\right)$$

with the effective work function

$$\Phi_{\text{eff}} = \Phi + \delta\Phi_{\text{RS}}$$

and the Richardson *constant* A_{R} . Its theoretical value is $4\pi k_{\text{B}}^2 m_{\text{e}} e / h^3 \approx 1.2 \cdot 10^6 \text{ A}/(\text{K}^2 \text{ m}^2)$.

material	Φ [eV]	A_R [10^6 A/(K ² m ²)]	T_{melt} [K]
Re	4.74	7.2	3453
C	4.53	0.6	3823
Ta	4.09	0.3	3269
W (poly)	4.52...4.55	600	3653
W (xxx)	4.20...6.0	600	
W/ThO ₂ /Th	2.63	0.03	
W/Ba	2.66	1	
W/La	2.72	0.08	

Table 3.1: Electron emission properties of various materials [And90].

For practical applications, the influence of the surface electric field E_S on electron emission is given by the Schottky correction formula (in eV) [And90]:

$$\delta\Phi_{\text{RS}} = -\sqrt{\frac{eE_S}{4\pi\epsilon_0}}$$

The work functions of some non refractive cathode materials used for high intensity arc discharges are summarized in table 3.1. The Φ and A_R values in this table were determined experimentally (best fit to the Richardson equation). There seems to be a noticeable variation of A_R . The values provided for doped tungsten materials are estimated and may also depend on the surface state of the electrode and the local surface concentration of the dopant.

Secondary electron emission by the impinging ion current j_i is given by $j_{\text{SEE}} = \gamma_i \cdot j_i$ where $\gamma_i = 0.01 \dots 0.3$. It can be neglected for most arc discharge configurations. For low pressure discharges, γ_i becomes important. For argon with tungsten cathodes a value of 0.07 can be estimated [PPB+92].

In the case of high surface electric fields and cathode hot spot current densities, the emission current has to be calculated by the full thermo-field emission theory (see figure figure 3.9 and [PKS93]).

The strong temperature and work function dependence of the emission current density determines the cathode hot spot temperature and may result in a bifurcation of the cathode hot spot system: Choosing optimum cathode geometry and a reasonable large discharge current, the arc constricts to a diffuse hot spot with current densities of $10^6 \dots 10^8$ A/m² and several hundred microns in diameter (diffuse mode).

If the cathode is cooled by external means or by geometrical design, the hot spot may constrict below a critical current density and field electron emission becomes increasingly important (spot mode).

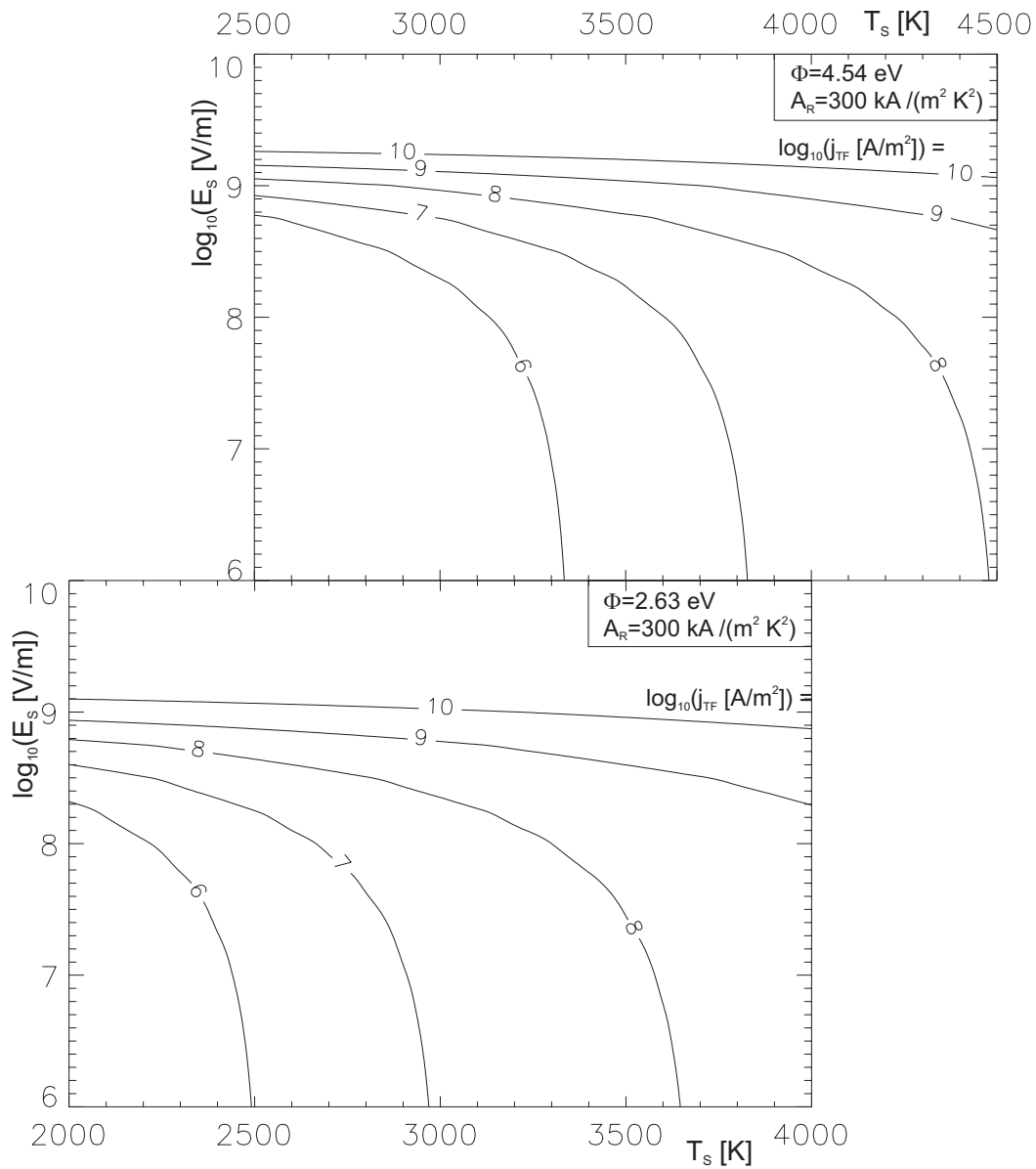


Figure 3.9: Calculated thermo field emission current density of pure and thoriated tungsten (to visualize the Φ -dependency only, the A_R value was chosen not in agreement with table 3.1).

3.3.2 Space charge layer (sheath)

For the discharge the space charge layer (sheath) has the following functions:

- limiting the back diffusion of the plasma electrons by a retarding electrical field which also isolates thermally the electron fluid from the surface – i.e. the diffusion of the electrons from the plasma is inhibited by a potential barrier,
- accelerating the ions heating the surface to thermionic emission temperatures,
- accelerating the emitted electrons in order to gain energy for ionization in the presheath,
- increasing electron emission by the high electric field at the surface.

The detailed potential and electric field distribution within the sheath is not relevant to the hot spot formation or overall discharge behaviour. The most important quantity, the voltage drop across the layer U_S , is calculated by the energy balance at the sheath edge in section 3.3.3.

For the calculation of the electric field at the surface a simplified model is used. In the case of a collision-free space charge sheath ($l_{ia} \gg \lambda_{\text{Debye}}$), the Poisson equation for the sheath can be solved analytically for the electric field strength at the cathode surface (see [Mac29, Wen90]):

$$E_S^{\text{MK}} = \sqrt{\frac{4}{\epsilon_o} \left(j_{\text{ion}} \cdot \sqrt{\frac{m_i U_S}{2 Z_{\text{eff}} e}} - j_{\text{RS}} \cdot \sqrt{\frac{m_e U_S}{2e}} \right)}.$$

Within an accuracy of $\sqrt{m_e/m_i}$ this simplifies to the so called McKeown formula

$$E_S^{\text{MK}} = \left(\frac{8 Z_{\text{eff}} m_i j_{\text{ion}}^2 U_S}{e \epsilon_o^2} \right)^{\frac{1}{4}}.$$

The influence of multiple charged ions was taken into account by using the effective ion charge Z_{eff} . As a conclusion, the electric field at the cathode surface depends on the voltage drop across the sheath U_S and the ion current density at the sheath edge j_{ion} . For a collision-dominated sheath (ion atom mean free path $l_{ia} \ll \lambda_{\text{Debye}}$), the electric field can be also be calculated by integrating a simplified Poisson equation for the sheath [War55, LA99]

$$E_S^{\text{W}} = \left(\frac{5 j_{\text{ion}} U_S}{3 \epsilon_o \xi} \sqrt{\frac{m_i}{e l_{ia}}} \right)^{\frac{2}{5}}$$

with $\xi = 1.143$.

For the overall current balance, the electron back diffusion current is calculated by

$$j_{e,\text{SE}}^{\text{back}} = 1/4 e n_e v_{e,\text{SE}}^{\text{th}} \cdot \exp\left(-\frac{e U_S}{k_b T_{e,\text{SE}}}\right)$$

where $T_{e,\text{SE}}$ is the electron temperature at the sheath edge and n_e the electron density at this position. The mean thermal velocity is given by

$$v^{\text{th}} = \sqrt{\frac{8 k_b T}{\pi m}}.$$

3.3.3 Energy balance and current continuity at the sheath edge

As known since the beginning of the century [Sta03], one of the main purpose of the space charge layer is to accelerate the emission electrons in order to sustain the ionization within the presheath. Approximately, the energy needed is given by the ion current density at the sheath edge times the ionization energy $j_{i,SE} \cdot E_{ion}/e$. Within this estimate, the sheath voltage drop is given by

$$U_S = \frac{j_i E_{ion}}{e j_{RS}}$$

Benilov and Marotta [BM95] formulated a more accurate electron energy balance at the sheath edge which is used for this work:

There are two sources, the flux of energy brought into the layer by the emitted electrons accelerated in the space charge sheath $j_{RS}/e \cdot (2k_b T_S + eU_S)$ and the work of the electric field over the electrons inside the layer calculated from the mean presheath electron current to $\overline{j_{e,PS}} \cdot U_{PS}$, where U_{PS} is the voltage drop across the presheath. In the following the electron temperature T_e means the electron temperature at the sheath edge.

The energy losses at the sheath edge are coming from the electron back diffusion current leaving the presheath for the sheath $j_{e,back}/e \cdot (2k_b T_e + eU_S)$ and the electron current leaving to the bulk plasma $j_{tot} \cdot (\frac{5}{2} + D_e^T) k_b T_e / e$ and the losses due to inelastic collisions required to sustain the ion current $j_i/e \cdot E_{ion}$. Together with the current continuity condition, the following equation system has to be solved for the current density j_{tot} and the space charge sheath voltage drop U_S :

$$j_{tot} = j_{ion} - j_{e,back} + j_{RS} \quad (3.1)$$

$$\begin{aligned} j_{RS}/e \cdot (2k_b T_S + eU_S) \\ + \overline{j_{e,PS}} U_{PS} &= j_{e,back}/e \cdot (2k_b T_e + eU_S) \\ &+ j_{tot}/e \cdot (\frac{5}{2} + D_e^T) k_b T_e \\ &+ j_i/e \cdot E_{ion} \end{aligned} \quad (3.2)$$

This equation system is solved for all positions along the cathode hot spot surface.

For single charged ions, using $D_e^T \approx 0.7$ and $\overline{j_{e,PS}} = \frac{1}{2} (j_{tot} + j_{RS} - j_{e,back})$, the space charge layer voltage drop can be calculated for a given ion current density j_{ion} , emission current density j_{RS} and electron back diffusion current density $j_{e,back}$, sheath edge electron temperature T_e and presheath voltage drop U_{PS}

$$\begin{aligned} U_S &= \frac{j_{ion} \cdot (E_{ion} + 3.2k_b T_e - 0.5eU_{PS})}{e \cdot (j_{RS} - j_{e,back})} \\ &- \frac{j_{RS} \cdot (2k_b T_S + eU_{PS} - 3.2k_b T_e)}{e \cdot (j_{RS} - j_{e,back})} \\ &- \frac{j_{e,back} \cdot (1.2k_b T_e - eU_{PS})}{e \cdot (j_{RS} - j_{e,back})} . \end{aligned}$$

3.3.4 Ionization layer (pre-sheath)

A detailed one-dimensional model of the cathode layer was developed by Rethfeld and Wendelsdorf [RWKS96] based on the work of Hoffert and Lien [HL67] also continued by Hsu and Pfender [HP83a, Hsu82]. The presheath was identified as a stiff boundary value problem. The spatial

variation of the plasma parameters can be adapted to almost every set of plasma and sheath boundary conditions.

For modelling the overall cathode hot spot self consistently, only two parameters are important: the presheath potential drop and the sheath edge ion current density. First, the actual ion current j_i at the sheath edge can be calculated from the local current density in the plasma j_P , the electron emission current density j_{RS} and the electron back diffusion current $j_{e,b}$

$$j_i = j_P - j_{RS} + j_{e,b} .$$

The velocity of the ions at the sheath edge is given by the Bohm criterion [Boh49, Rie89]:

$$v_{i,Bohm} = \sqrt{\frac{k_b(T_i + Z_{eff}T_e)}{m_i}} .$$

The effective ion charge Z_{eff} is again used as a crude approximation for the influence of multiple charged ions. Using this ion current, the electron and ion density at the sheath edge can be calculated:

$$n_{i,SE} = n_{e,SE} = \frac{j_{ion}}{e v_{i,Bohm}} .$$

Assuming the electrons are in Boltzmann equilibrium with the presheath electric field, the presheath potential drop can be calculated:

$$\frac{eU_{PS}}{k_bT_e} = \log \frac{n_{e,P}}{n_{e,SE}} . \quad (3.3)$$

3.3.5 A simple presheath control model

The cathode layer model sketched above allows for the calculation of all discharge relevant data without prior knowledge of the detailed spatial variation of the physical quantities in the presheath. For controlling the physical validity of the results, the presheath voltage drop can be computed by the model of Benilov and Marotta [BM95]. The presheath voltage drop is again calculated from equation 3.3, but the sheath edge electron density is calculated by a presheath model to

$$n_{e,SE}^{BM} = n_{e,P} \cdot \frac{0.8}{2 + \alpha}$$

with

$$\alpha = \sqrt{\frac{k_bT_h}{m_i D_{ia} \alpha_{rek} n_{e,P}^2}} .$$

The heavy particles temperature T_h and ion-atom diffusivity D_{ia} are calculated for an average presheath heavy particles temperature T_h . The recombination coefficient α_{rek} is calculated in section 4.10. Using this sheath edge electron density, the sheath edge ion current density becomes

$$j_{SE}^{BM} = e n_{e,SE}^{BM} \cdot v_{Bohm} .$$

The ion current density calculated from this equation agrees perfectly with the ion current densities calculated self consistently using the scheme from the previous subsection (see also figure 5.9).

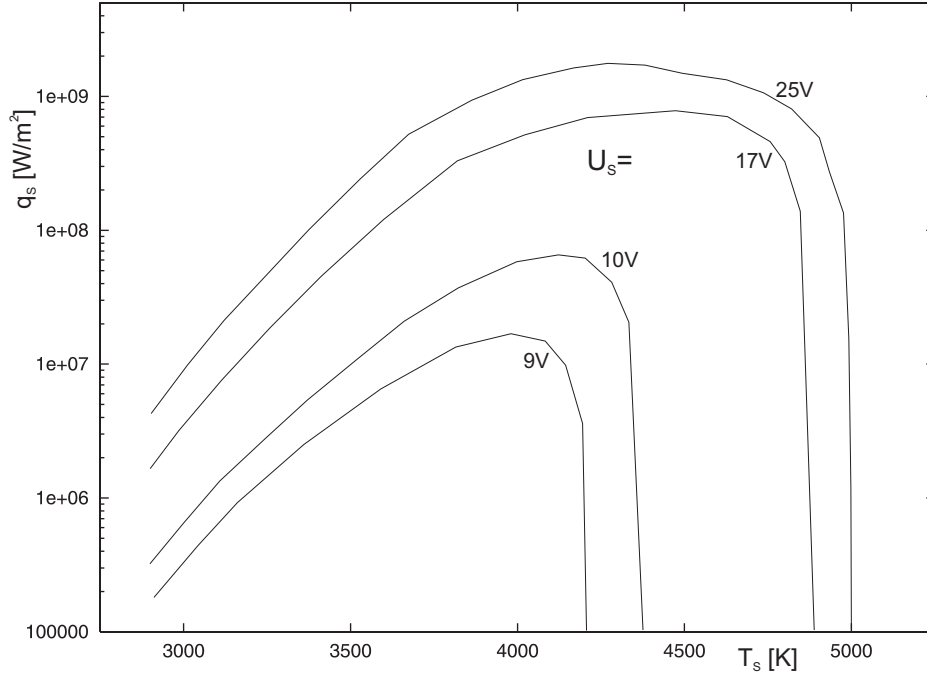


Figure 3.10: Energy flux density to the cathode surface as a function of surface temperature [BM95].

3.3.6 Sheath-surface boundary conditions

The local net heating or cooling of the cathode surface is given by a summation over all possible contributions

$$q_S = q_{S,i} + q_{S,em} + q_{S,rad} + q_{S,e,back} + q_{S,a} + q_{S,a,back} \quad (3.4)$$

with

$$\begin{aligned} q_{S,i} &= j_i/e \cdot \left(2k_b T_{h,SE} + \frac{1}{2} Z_{eff} k_b T_{e,SE} + Z_{eff} e U_S + E_{ion} - Z_{eff} \Phi_{eff} \right) \\ &\quad \text{(ion heating)} \\ q_{S,em} &= -j_{RS} \Phi_{eff} \\ &\quad \text{(emission cooling)} \\ q_{S,rad} &= \epsilon_{SB} C_{SB} T_S^4 \\ &\quad \text{(thermal radiation cooling)} \\ q_{S,e,back} &= j_{e,back}/e \cdot (2k_b T_{e,SE} + \Phi_{eff}) \\ &\quad \text{(electron back diffusion heating)} \\ q_{S,a} &= -\lambda_a \vec{\nabla} T_h \\ &\quad \text{(neutrals heat conduction)} \\ q_{S,a,back} &= -j_i/e \cdot (2k_b T_S) \\ &\quad \text{(back flow of recombined ions)} \end{aligned} \quad (3.5)$$

The Stefan-Boltzmann constant is given by $C_{\text{SB}} \approx 5.67 \cdot 10^{-8} \text{ W/m}^2$ and the temperature dependence of the (tungsten) surface emissivity is given by [YW79]:

$$\epsilon_{\text{SB}} = -0.0266 + 1.8197 \cdot 10^{-4} \cdot T_{\text{S}} - 2.1946 \cdot 10^{-8} \cdot T_{\text{S}}^2$$

where the local surface temperature T_{S} is given in K.

Within the cathode hot spot, q_{S} is mainly given by ion heating balanced by emission cooling. The typical behaviour of this net energy flux density for different values of the sheath voltage drop is plotted in figure 3.10. From these plots, one can estimate the upper limit for the cathode hot spot temperature that is possible for a specific work function of the cathode material: 3630..4610K for thoriated tungsten ($\Phi = 2.7\text{eV}$) and 4340..4905K for pure tungsten ($\Phi = 4.5\text{eV}$) [EFF⁺91].

3.3.7 Presheath-plasma boundary conditions

While the boundary conditions for the cathode surface are determined by equation 3.4, the electron energy balance of the plasma in front of the cathode surface is dominated by the Joule heating term and thus the major boundary condition is coming from the calculation of the local layer current density (equation 3.1).

Additionally, the following source term is included into the energy balance within the cathode layer:

$$S = j_{\text{RS}}(2k_{\text{b}}T_{\text{C}}/e + U_{\text{S}}) + j_{\text{tot}}U_{\text{PS}} - j_{\text{i}}E_{\text{ion}}/e - j_{\text{e,b}}(2k_{\text{b}}T_{\text{e,SE}}/e + U_{\text{S}})$$

Within the anode layer, the source term

$$S = -j_{\text{e,b}}(5/2 k_{\text{b}}T_{\text{e,SE}}/e + U_{\text{S}})$$

is used.

3.4 The anode–plasma transition layers

Analogous to the cathode layer, the anode layer is divided into a sheath and a presheath structure. The distribution of the electric potential within this system is a bit different to the one at the cathode. As sketched in figure 3.11, the voltage drop of the space charge layer is negative. Assuming the anode is not emitting electrons, the current transport is mainly due to the plasma electrons diffusing to the anode surface against the (negative) space charge voltage drop (the nomenclature is the same as for the cathode):

$$j_{\text{e,SE}}^{\text{back}} = 1/4 e n_{\text{e}} v_{\text{e,SE}}^{\text{th}} \exp\left(-\frac{eU_{\text{S}}}{k_{\text{b}}T_{\text{e,SE}}}\right)$$

The voltage drop U_{S} is about several volts (3-8V) because the electron saturation current ($U_{\text{S}} = 0$) is above the usual current densities in the plasma.

As can be seen from figure 3.11, there must be a location in the layer, where the electric field is zero. At this position, the electric current is only diffusive (see also section 3.5.3):

$$j_{\text{e}} = \sigma \cdot \frac{k_{\text{b}}T_{\text{e}}}{e} \cdot \frac{\vec{\nabla} n_{\text{e}}}{n_{\text{e}}} .$$

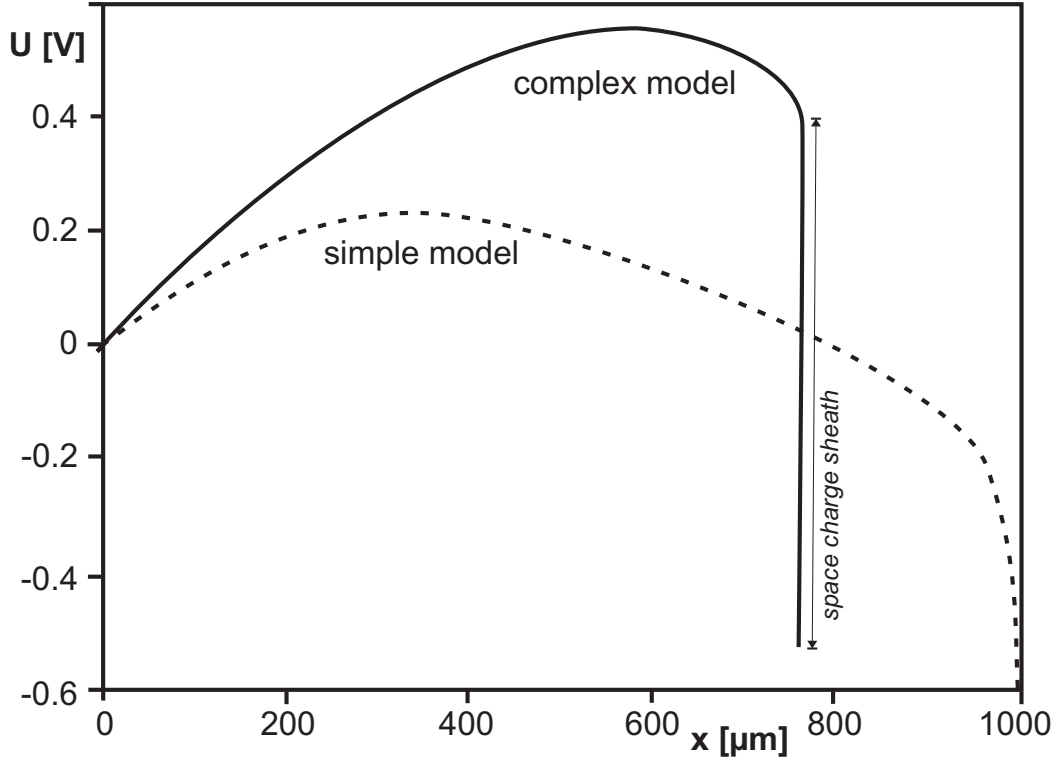


Figure 3.11: Voltage distribution in the anode layer for a diffuse anode attachment in a 0.1 MPa argon arc [Pan94].

Assuming a linearly descending $n_e(x)$, the sheath edge electron density becomes

$$n_{e,SE} = n_{e,P} \cdot \left(1 + \frac{e d_{\text{layer}} j_{\text{tot}}}{k_b \sigma T_e} \right)^{-1}.$$

The presheath voltage drop U_{PS} is then calculated by equation 3.3 and the sheath voltage drop U_S reads

$$U_S = \frac{k_b T_e}{e} \log \left(\frac{e n_{e,SE} v_e^{\text{th}}}{4 j_{\text{tot}}} \right).$$

Finally, the local net heating of the anode surface is analogous to the cathode given by

$$q_S = q_{S,\text{rad}} + q_{S,e,\text{back}} + q_{S,a} \quad (3.6)$$

with

$$\begin{aligned} q_{S,\text{rad}} &= \epsilon_{SB} C_{SB} T_S^4 && \text{(thermal radiation cooling)} \\ q_{S,e,\text{back}} &= j_{e,\text{back}}/e \cdot (2k_b T_{e,SE} + \Phi_{\text{eff}}) && \text{(electron back diffusion heating)} \\ q_{S,a} &= -\lambda_a \vec{\nabla} T_h && \text{(neutrals heat conduction)} \end{aligned} \quad (3.7)$$

The surface energy balance within the hot spot region of the anode is dominated by condensation of the current carrying electrons at the surface ($q_{S,e,back}$).

Compared to the cathode layer model in section 3.3, this anode layer model is rather crude. For enhancement, there may be the need to perform a detailed local 1-D calculation instead of the pure analytical model used here.

Additionally, the role of energetic photons (UV resonance radiation, see also [CPR88]) in the cathode and anode layers is currently not included into any self-consistent model, but can change the ionization balance in the presheath. The models used in this section does not require a detailed calculation of the presheath properties.

3.5 The thermal arc plasma

Electric arcs are rather complex entities because of their spatial inhomogenities and the amount of plasma physics necessary for a description of the discharge. While low pressure discharges require a more or less kinetic treatment, because at least the electron distribution function is non-Maxwellian, the thermal plasma of the arc can be treated by a multi-fluid approach. Additionally, the full multi-fluid theory [Bra65] can be simplified to a one-fluid treatment regarding flow phenomena and a coupled two-fluid model regarding energy transport.

While the layer physics presented in the preceeding sections, provide the boundary conditions for the thermal arc plasma, the multidimensional description of this region (often called the arc column, but also valid for the near electrode plasma regions) is provided in the following subsections.

The thermal arc plasma is treated as a quasineutral ($n_e = n_i$) conducting fluid. Except for the energy balance, the electrons and heavy particles are treated as a single fluid.

3.5.1 Modelling the flow of the conducting plasma fluid

3.5.1.1 Mass continuity

First, the equation of mass continuity (written in the *conservation form*)

$$\frac{\partial}{\partial t}\rho + \vec{\nabla} \cdot (\rho\vec{v}) = 0, \quad (3.8)$$

has to be fulfilled. For small Mach-numbers ($\text{Ma} = |\vec{v}|/v_c < 0.3$, i.e. the flow speed is well below the local speed of sound [Pan93]), the plasma fluid can be regarded as *incompressible*

$$\vec{\nabla} \cdot \vec{v} = 0 \quad , \quad (3.9)$$

a well-justified assumption actually used by all authors. In this work, equation 3.8 is solved.

3.5.1.2 Momentum balance

From Newtons second law, the momentum equation is derived ([Pan93] and [BSL60]):

$$\begin{array}{l} \rho \frac{\mathbf{D}}{\mathbf{D}t} \vec{v} = \quad - \quad \vec{\nabla} p \quad + \quad \vec{\nabla} \cdot (\eta \underline{\pi}) \\ \text{momentum change per} \quad \text{force of the scalar} \quad \text{friction loss per} \\ \text{time interval and} \quad \text{pressure per} \quad \text{volume} \\ \text{convection loss per} \quad \text{volume} \\ \text{volume} \end{array} \quad (3.10)$$

$$\begin{array}{l} + \quad \vec{j} \times \vec{B} \quad + \quad \rho \cdot \vec{g} \\ \text{Lorenz force per} \quad \text{gravity force per} \\ \text{volume} \quad \text{volume} \end{array} .$$

The total time derivative is defined as usual¹. The strain-rate tensor $\underline{\pi}$ is described in [Pan93]. For cylindrical coordinates, $\underline{\pi}$ can be found in [BSL60]. The dynamic viscosity η is the proportionality factor between momentum current and velocity gradient and is calculated and

¹ $\frac{\mathbf{D}}{\mathbf{D}t}(\dots) = \frac{\partial}{\partial t}(\dots) + \vec{v} \cdot \vec{\nabla}(\dots)$

discussed in section 4.6. Natural convection forces become important for high pressure arc lamps or gas shielding effects occurring in welding applications.

Regarding momentum transport, the type of the flow is determined by the viscosity η , velocity u and characteristic dimension l of the problem. From these quantities, a characteristic dimensionless number can be derived, the *Reynolds number*:

$$\text{Re} = \frac{\rho u l}{\eta}$$

Flows with equal Reynolds numbers are similar. In thermal plasma gas discharges, Re is not small (> 1), but well below the critical values for turbulence (≈ 1000).

3.5.2 Modelling the energy transport within the plasma

3.5.2.1 Equilibrium (LTE) heat balance

Heat is generated in the plasma by Joule heating and carried away by radiation (net radiation loss coefficient S_R , section 4.9), conduction (heat conductivity λ , section 4.7) and convection. The compression work $\vec{\nabla} \cdot \vec{\nabla} p$ and viscous dissipation $\vec{\nabla} : \underline{\underline{\pi}}$ can be neglected, because the Mach-Number is about 0.1 and Prandtl-Numbers² $\text{Pr} = c_p \eta / \lambda$ are small (0.03...0.7). Because the total pressure in the discharge region is mainly constant, the energy balance is formulated in terms of the plasma enthalpy h and reads

$$\rho \frac{\text{D}}{\text{D}t} h = \underbrace{\vec{\nabla} \cdot \vec{\mathbf{q}}}_{\text{heat flux}} + \underbrace{\vec{\mathbf{j}} \cdot \vec{\mathbf{E}}}_{\text{Joule heating}} - \underbrace{S_R}_{\text{radiation loss}} \quad (3.11)$$

enthalpy change and
convection loss per unit
volume

(For the Joule heating term one can often find the equivalent forms j^2/σ or σE^2). The heat flux is given by conduction, enthalpy transport by the (current carrying) electrons and the diffusion–thermo (Dufour) effect from the (de)mixing of different plasma components [Ete93]:

$$\vec{\mathbf{q}} = \frac{\lambda}{c_p} \vec{\nabla} h + \frac{5k_b}{2e} \frac{\vec{\mathbf{j}}}{c_p} h + \vec{\nabla} \cdot \left[\sum_i \left(\rho D - \frac{\lambda}{c_p} \right) (h_i) \vec{\nabla} C_i \right]. \quad (3.12)$$

For simple one gas component plasmas, the Dufour effect vanishes and for numerical convenience, the temperature formulation is introduced ($\vec{\nabla} h = c_p \vec{\nabla} T$):

$$\rho c_p \frac{D}{Dt} T = \vec{\nabla} \cdot \left(\lambda \vec{\nabla} T + \frac{5k_b}{2e} \vec{\mathbf{j}} \cdot T \right) + \vec{\mathbf{j}} \cdot \vec{\mathbf{E}} - S_R$$

Even for modelling discharge configurations showing negligible deviations from LTE, the electron enthalpy flow term $5k_b/(2e) \vec{\mathbf{j}} \cdot T_e$ becomes undefined near the cathode layer, where a temperature split ($T_e \neq T_h$) takes place in *every* discharge situation and the LTE model has to fulfill boundary conditions at the electrode coming from the heavy particle / electrode surface interaction³, while the electrons are thermally isolated by the space charge layer voltage drop.

²describing the relation of momentum diffusivity to thermal diffusivity [And90, p.67].

³With decreasing size of the layer, there are circumstances where the temperature split can be modeled by the cathode layer model only.

3.5.2.2 Two temperature (pLTE) heat balances

Typical for thermal plasmas is the phenomenon of temperature split at pressures below 0.1 MPa, at temperatures below 9000K and near the electrodes. The electrons become decoupled from the heavy particles. For this reason, accurate modelling requires the electrons and the heavy particles to be treated as different fluids (two-fluid model). The energy balance of the electrons becomes

$$\rho_e \frac{\mathbf{D}}{\mathbf{D}t} h_e = \vec{\nabla} \cdot \vec{\mathbf{q}}_e + \vec{\mathbf{j}} \cdot \vec{\mathbf{E}} - S_R - \dot{E}_{eh} \quad (3.13)$$

with the electron heat flux

$$\vec{\mathbf{q}}_e = \frac{\lambda_e}{c_{p,e}} \vec{\nabla} h_e + \frac{5k_b}{2e} \frac{h_e}{c_{p,e}} \vec{\mathbf{j}} \quad (3.14)$$

and the energy exchange term \dot{E}_{eh} as discussed in section 4.4.

Analogously, neglecting transport of ionization energy [Kru70], the enthalpy balance of the heavy particles becomes

$$\rho_h \frac{\mathbf{D}}{\mathbf{D}t} h_h = \vec{\nabla} \cdot \vec{\mathbf{q}}_h + \dot{E}_{eh} \quad (3.15)$$

with the heavy particles heat flux

$$\vec{\mathbf{q}}_h = \frac{\lambda_h}{c_{p,h}} \vec{\nabla} h_h + \vec{\nabla} \cdot \left[\sum_i \left(\rho_i D_i - \frac{\lambda_{h,i}}{c_{p,h,i}} \right) (h_i) \vec{\nabla} C_i \right].$$

The heat conductivity is discussed in section 4.7. Incidentally, one has to distinguish between the general (3D) formulation given above, the (published) 2-D equations and the equations really treated by the individual computer code.

For this work (chapter 5), the full set of the equations is solved (without the Dufour term, because no complex gas mixtures are investigated).

3.5.3 Modelling the electric current transport

Regardless the importance of hydrodynamic transport phenomena, the arc is mainly an electrical phenomenon. Taking into account that the plasma column is electrical neutral (quasineutrality, $\rho_{el} \approx 0$), the generalized Ohm's law becomes [FM57, Vil82]

$$\vec{\mathbf{j}} = \sigma \cdot \left\{ \vec{\mathbf{E}} + \vec{\mathbf{v}} \times \vec{\mathbf{B}} - \frac{1}{n_e e} \vec{\mathbf{j}} \times \vec{\mathbf{B}} + \frac{1}{2en_e} \vec{\nabla} p_e + 0.41 \cdot \frac{k_b}{2e} \vec{\nabla} T_e \right\}, \quad (3.16)$$

The second and third terms (induction and Hall current) can be safely neglected. The fourth term, the diffusion current can influence the current transport within the electric arc [FM57]:

- In the outer regions of the arc, there is a diffusive current towards the axis and thus a space charge compensating electric field.
- On the axis, the diffusion current contributes about 10% to the overall electric current density.
- Near the anode, the diffusive current density can become as large as the *normal* one.

The (last) thermodiffusion term is in general significantly smaller than the diffusion current and may be neglected (for its derivation and the 0.41 factor see [Bra65, Vil82]).

Because of the numerical difficulties of using this generalized Ohm's law and because diffusion current contribute less than 10% to the total current density (except near the anode), most authors use the conventional Ohm law

$$\vec{j} = \sigma \vec{E}$$

where σ denotes the electric conductivity depending on the local electron temperature. Recently, 2-D modelling results without this simplification were published [AJHP98]. The results give additional evidence of the diffusive current transport for the plasma anode transition region (anode attachment modes), while it can be neglected in the main plasma column and the cathode attachment region. Thus, current continuity law

$$\nabla \cdot \vec{j} = 0 \quad (3.17)$$

gives a Laplace-type equation

$$\vec{\nabla} \cdot (\sigma \vec{\nabla} \Phi) = 0. \quad (3.18)$$

for the electric potential Φ . This equation is solved in the main arc plasma throughout this work.

3.5.3.1 Magnetic field calculation

Starting with Ampere's law

$$\vec{\nabla} \times \vec{H} = \vec{j} + \dot{\vec{D}}$$

and using

$$\nabla \cdot \vec{B} = 0 \quad , \quad \vec{B} = \mu_0 \mu_r \vec{H} \quad , \quad \vec{B} = \vec{\nabla} \times \vec{A}$$

the well known equation for the vector potential \vec{A} is found in the form

$$\Delta \vec{A} = -\mu_0 \vec{j}$$

with the solution

$$\vec{A}(\vec{r}) = \frac{\mu_0}{4\pi} \int \frac{\vec{j}(\vec{r}')}{|\vec{r} - \vec{r}'|} d^3 r' .$$

The displacement current may be neglected as $|\dot{\vec{D}}| \ll |\vec{j}|$ and the Coulomb gauge

$$\vec{\nabla} \times \vec{A} = 0$$

is used. Application of curl yields Biot-Savart's law

$$\vec{B}(\vec{r}) = \frac{\mu_0}{4\pi} \int \frac{\vec{j}(\vec{r}') \times (\vec{r} - \vec{r}')}{|\vec{r} - \vec{r}'|^3} d^3 r' .$$

For this work, the plasma geometry is radial-symmetric and the axial current density component j_z is much larger than the radial one j_r . The magnetic field is simply given by $\vec{B} = \{0, 0, B_\theta\}$. Neglecting the displacement current and with $\mu_r \approx 1$, Ampere's law reduces to

$$\frac{1}{r} \frac{\partial}{\partial r} (r B_\theta) = \mu_0 j_z .$$

This equation can be integrated from $\rho = 0$ (where $B_\theta = 0$) to $\rho = r$. Finally, the azimuthal magnetic field $B_\theta(r, z)$ is obtained by a simple integration over the axial electric current density:

$$B_\theta(r, z) = \frac{\mu_0}{r} \int_0^r j_z(\rho, z) \rho d\rho. \quad (3.19)$$

3.5.4 Diffusion and other transport phenomena

3.5.4.1 Ambipolar diffusion

In high pressure discharges, diffusion of charged particles is not free. There is a strong coupling between the electrons and ions. This phenomenon is called *ambipolar* diffusion. For the electric arc, the corresponding diffusivity D_{amb} is almost identical to the ion-atom diffusivity D_{ia} (see section 4.5). The additional equation to be solved within the (2 or 3D) plasma region reads:

$$\frac{\mathbf{D}}{\mathbf{D}t}n_e + \vec{\nabla} \cdot \left[\frac{en_e D_{\text{ia}}}{k_b T_h} \left(\vec{\mathbf{E}} - \frac{1}{en_e} \vec{\nabla} p_i \right) \right] = \dot{n}_e .$$

The heavy particles (ions and atoms) are described by a single local temperature $T_h = T_i = T_a$. $p_i = n_i k_b T_h$ is the partial pressure of the ions ($n_i = n_e$, [Din79]) and \dot{n}_e the net ionization rate (see section 4.10). The major application of this additional diffusion equation is detailed modelling of the anode attachment [AJHP98].

An alternative approach more applicable for arcs producing large plasma jets or influenced by external gas flow, is to model the neutral atom balance equation

$$\frac{\mathbf{D}}{\mathbf{D}t}n_0 = -\dot{n}_e$$

together with Dalton's law and charge neutrality condition (see section 4.2 and [Hai99]).

3.5.4.2 Turbulent plasmas

Some applications like plasma gas cutting result in turbulent plasma flows. The inclusion of turbulence into the arc column model is reviewed in [WDWS97b] and not used or discussed here.

3.6 Summary of the arc discharge physics

Applying the physical models of the discharge regions sketched above, means making a number of basic assumptions, which are well justified and accepted:

- The fluid flow in the arc column is laminar ($Re < 400$).
- The arc column is in partial local thermodynamic equilibrium (pLTE), i.e. locally determined by the variables velocity \vec{v} , electron temperature T_e , heavy particles temperature T_h , pressure p and the electromagnetic quantities current density \vec{j} , electric potential Φ and magnetic field \vec{B} . This is called two-fluid ($T_e(\vec{r}) \neq T_{i,a} \equiv T_h(\vec{r})$) hydrodynamic treatment.
- The arc column plasma is quasi-neutral, i.e. free of space charges.
- The non equilibrium layers (sheaths) in front of the electrodes are small against the overall electrode arc attachment region – they are skin like. This is always valid for the space charge layer (sheath), but sometimes questionable for the ionization layer (presheath).

These assumptions are valid for most discharge situations not too far away from LTE. This physical model requires additional computation of the plasma composition and transport coefficients depending mainly on electron temperature, as described in the next chapter.

Finally, the model will allow predictions for the overall discharge behaviour and the detailed spatial distributions of the physical parameters like plasma and electrode temperature. Results for a number of typical applications are provided in chapter 5.

It is evident from the different physical processes governing the main arc plasma and the sheaths, that the discharge cannot be described by a single set of equations. For physical self consistence, a proper definition of the internal boundaries and an iterative linkage of the submodels is crucial – as provided by this and the preceding chapter.

Low at my problem bending
Another problem comes -
Larger than mine - serener -
Involving statelier sums

E. Dickinson

Chapter 4

Plasma properties and transport coefficients

4.1 Introduction

The composition, thermodynamic properties and transport coefficients of thermal plasmas strongly vary with temperature. Their calculation in local thermodynamic equilibrium (LTE, $T_e = T_h$) is based on the work of Hirschfelder, Curtis and Bird [HCB64] using tabulated partition functions [DF65]. Significant efforts were dedicated to the transport theory foundations since the early work of Devoto [Dev65]. Starting 1977 [KB77], non equilibrium effects within the partial LTE concept (pLTE, $T_e \neq T_h$) were introduced [Hsu82, Bon83].

Focussing the efforts on modelling the overall arc discharge, the results of these references were selected and applied on the basis of the current knowledge from major working groups. The approach is to focus on LTE discharges, but to use the two-temperature model in order to identify parameter ranges, where identical electron and heavy particles temperature in the main arc plasma (column) is not a valid assumption.

An *ab initio* description of arc discharges more far away from LTE requires a closer look to the excitation equilibria [vdM90] and is regarded not to be within the range of current modelling resources.

As summarized below, the plasma composition and transport coefficients show a strong variation with *electron temperature*, while the effects of temperature split ($\Theta = T_e/T_h > 1$) are relatively weak. This does not justify the use of LTE models for discharges not in LTE, because deviations of electron temperature from the heavy particles temperature will imply important variations of plasma parameters and transport coefficients through the T_e dependencies. As an example, the LTE electric conductivity of an atmospheric argon plasma at 5000K is almost zero, but allowing for an electron temperature of 10000K will give a conductivity of 2000 S/m. Such temperature split effects are important for *all* electric arc discharges within a small layer in front of the electrodes, where LTE is almost impossible (except for some sodium vapour lamps) because the heavy particles equilibrate with the surface but the electrons are thermally isolated through a potential barrier (space charge sheath). Using a two temperature model will permit a self-consistent computation of this thermal boundary layer and enables the inclusion of electron enthalpy flow into the overall energy balance, because this term requires the electron temperature gradient, especially near the electrodes.

In the following sections, the plasma composition and thermodynamic properties are calculated (section 4.2) and the basic collision integrals are provided (section 4.3). These are needed to calculate the transport coefficients used within the macroscopic models discussed in chapter 3:

- The energy exchange rate coefficient linking the electron and heavy particles energy balances (4.4).
- The diffusivities required to calculate demixing, ambipolar diffusion and used as a basis for the other transport coefficients (4.5).
- The dynamic viscosity required to calculate the hydrodynamic plasma flow (4.6).
- The electron- and heavy particles heat conductivity (4.7).
- The variation of electric conductivity with electron temperature (4.8).
- The net plasma radiation emission coefficient is briefly discussed (4.9).
- The net recombination coefficient needed to calculate deviations from ionization equilibrium (4.10).

4.2 Plasma composition and thermodynamic properties

The foundation for the calculation of all plasma transport coefficients is the determination of the plasma composition as a function of electron temperature T_e and heavy particles temperature T_h . The particle densities of the individual components are determined by the condition of quasineutrality, Daltons law and the Saha-Eggert equations.

4.2.1 The condition of quasineutrality

Deviations from electrical neutrality (space charges) will produce high electric fields efficiently restoring electrical neutrality. On macroscopic scales, the plasma is thus electrical neutral (*quasineutral*). The electron density is equal to the sum of all ion densities times their ionization state:

$$n_e = \sum_{(i,j)} Z_{i,j} \cdot n_{i,j}$$

where i is the sum over all plasma components and j the sum over all ionization states taken into account.

4.2.2 Daltons law

Real gas effects (virial corrections) can be neglected within the temperature and pressure range of thermal plasmas [BFP94]. The total discharge pressure is described by the ideal gas law. The summation of the contributions from the individual plasma components gives:

$$p = \sum_j n_j k_b T_h + n_e k_b T_e .$$

Due to the effectiveness of charge-exchange collisions and the low ionisation degree of most high pressure discharges, ion temperature is assumed to be equal to the gas temperature.

At total discharge pressure levels above 10 MPa, the plasma becomes non-ideal. For a weak non-ideality, the Debye pressure correction can be introduced [Gri62]

$$p_{\text{Debye Correction}} = -\frac{e^2 n_e}{12\pi\epsilon_0\lambda_{\text{Debye}}}$$

The total discharge pressure is given by external conditions and thus one of the input parameters. The hydrodynamic pressure variations are usually less than 1% and therefore neglected for the calculation of the plasma composition and transport coefficients.

4.2.3 Saha-Eggert equation

The ionization equilibrium of the plasma is described by a system of Saha-Eggert equations [vdM90, vdSS91]

$$n_e \left(\frac{n_z}{n_{z-1}} \right) = \frac{\mathcal{Z}_e \mathcal{Z}_z}{\mathcal{Z}_{z-1}} \exp\left(-\frac{E_z - \delta E_z}{k_b T_e}\right)$$

describing the ratio of the densities of the different ionization states by a Boltzmann term with the excitation temperature equal to the electron temperature. This approximation is still under discussion [CH99, Bak90], but well accepted by most groups. Some minor modifications of the excitation temperature can be introduced, but are not crucial for the overall discharge behaviour [GCG99].

The partition function \mathcal{Z} is given by its translational, rotational, vibrational and internal contributions:

$$\mathcal{Z} = \mathcal{Z}_{\text{tr}} \cdot \mathcal{Z}_{\text{rot}} \cdot \mathcal{Z}_{\text{vib}} \cdot \mathcal{Z}_{\text{int}}$$

where rotational and vibrational contributions are unity for the monatomic gases used for this work. The translational partition function is

$$\mathcal{Z}_{\text{tr}} = \left(\frac{m_e k_b T_e}{2\pi\hbar^2} \right)^{3/2}$$

and the internal partition function is determined by the Energy E_n and degeneration δ_n of the excited levels of the individual atom or ion:

$$\mathcal{Z}_{\text{int}} = \sum_n^{E_n \leq E_z - \delta E_z} \delta_n \cdot \exp\left(-\frac{E_n}{k_b T_e}\right).$$

The exact energy levels of the ions and atoms within the plasma cannot be computed ab initio, thus the undisturbed energy levels of the free atoms and ions are used. The divergence of the partition function is avoided by a so called cut-off criterion (figure 4.1) [Gri64], allowing to calculate the lowering of the ionization energy:

$$\delta E_z = \frac{Z e^2}{4\pi\epsilon_o\lambda_{\text{Debye}}}$$

with the Debye length of the plasma

$$\lambda_{\text{Debye}} = \left(\frac{e^2}{\epsilon_o k_b} \sum_{\alpha} \frac{Z_{\alpha}^2 n_{\alpha}}{T_{\alpha}} \right)^{-1/2}. \quad (4.1)$$

The calculated particle densities are in good agreement with the values published in the literature (figure 4.2). The cut-off criterion has significant effects on viscosity and reactive heat conductivity only [Cap72, Mon99].

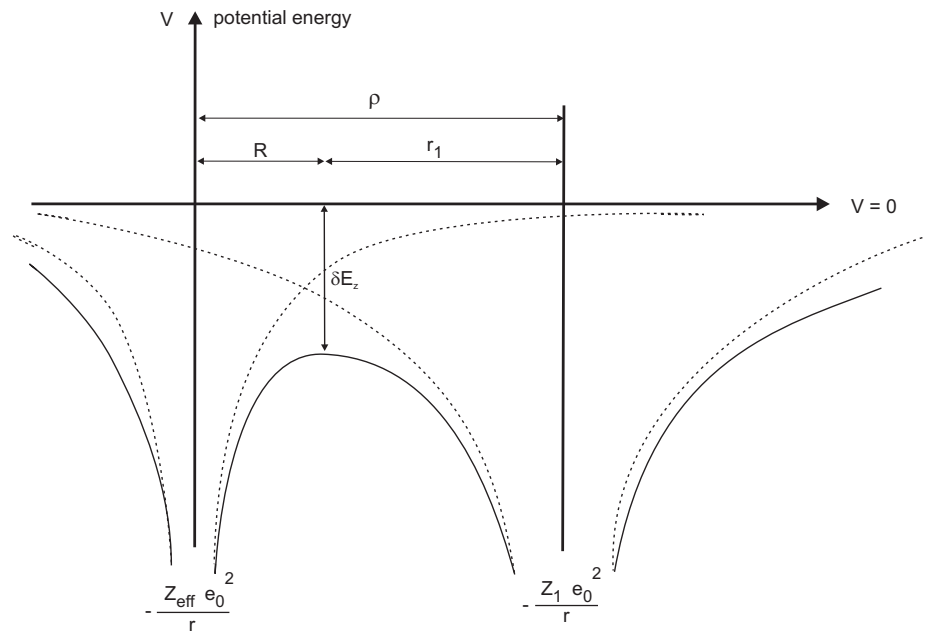


Figure 4.1: Lowering of ionization energy in a plasma [DF65].

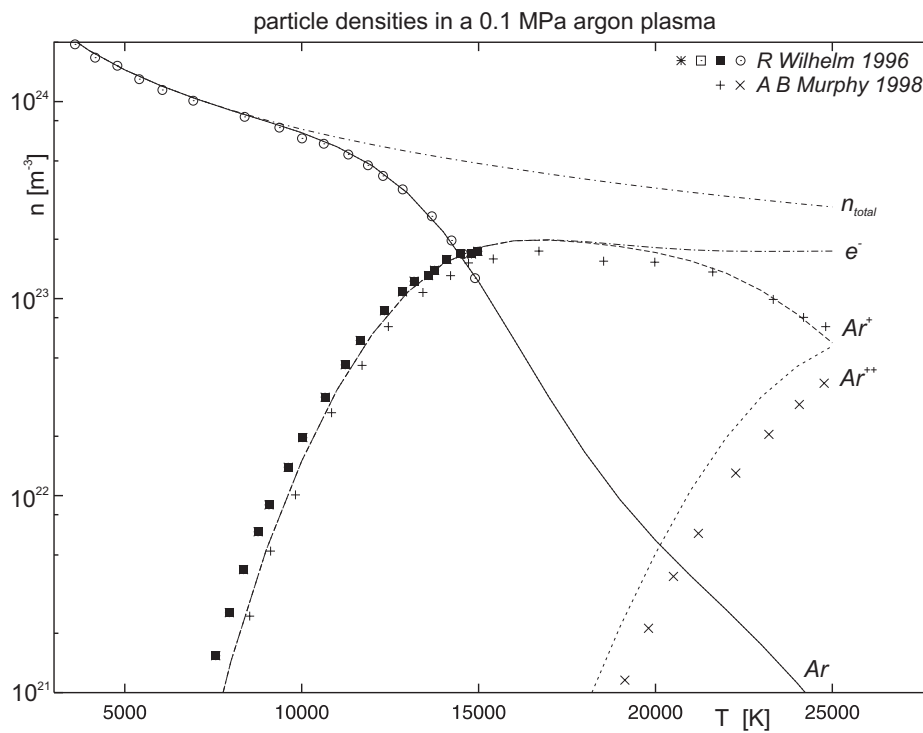


Figure 4.2: Particle densities in an atmospheric argon plasma (compared with the results from [Wil96b, Mur98]).

4.2.4 Mass density

The specific mass density of the plasma is computed from the individual particle densities and masses by

$$\rho \equiv \sum_{i=1}^N n_i \cdot m_i$$

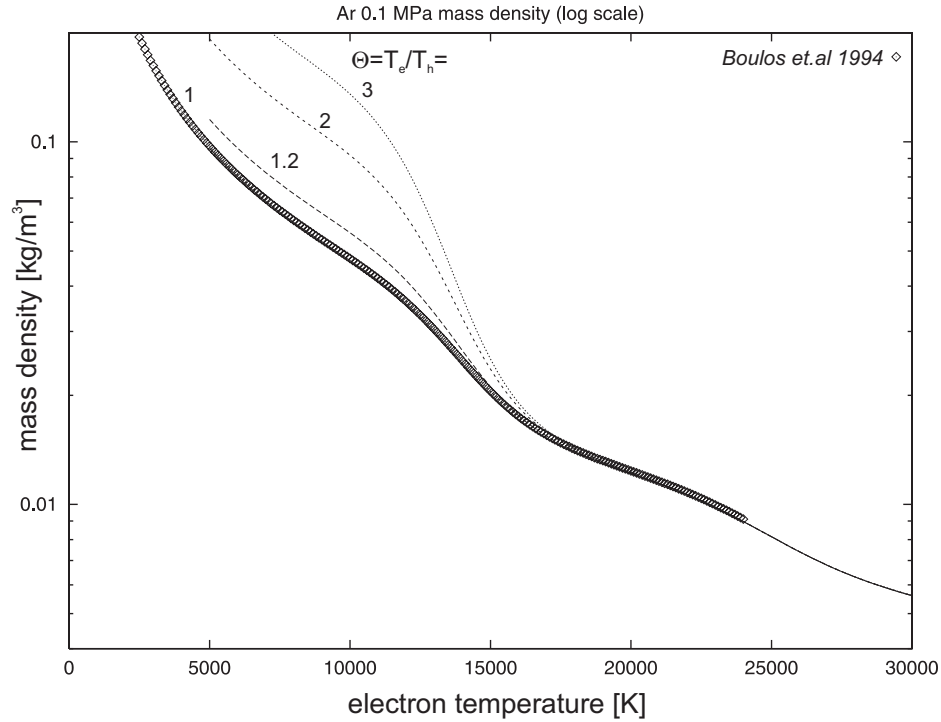


Figure 4.3: Specific mass of a 0.1 MPa argon plasma plotted against electron temperature (for comparison, the data from [BFP94] are also plotted).

As shown in figure 4.3, the mass density is sensitive to the non equilibrium parameter $\Theta = T_e/T_h$. This is due to Daltons law. As the total particle number increases with the onset of ionization, the ideal gas scaling $\rho \sim 1/T$ is not valid above the onset of ionization (e.g. above $T_e = 9000\text{K}$ for 0.1 MPa argon).

4.2.5 Enthalpy

The specific plasma enthalpy $h = u + pv$ is computed from the translational, excitational and chemical contributions [Hsu82]:

$$h = h_{\text{trans}} + h_{\text{excit}} + h_{\text{chem}}$$

with

$$h_{\text{trans}} = \frac{5}{2} \frac{k_b}{\rho} \left(n_e T_e + \sum_{\xi=\alpha,a} n_{\xi} T_{\xi} \right)$$

$$h_{\text{excit}} = \frac{k_b}{\varrho} \sum_{\xi=\alpha,a} T_\xi^2 n_\xi \frac{\partial \ln Z_\xi}{\partial T_e}$$

$$h_{\text{chem}} = \frac{1}{\varrho} \sum_{\alpha} n_\alpha \cdot (E_\alpha - \delta E_\alpha) .$$

where α denotes the different ions and a the different atoms within the plasma gas mixture.

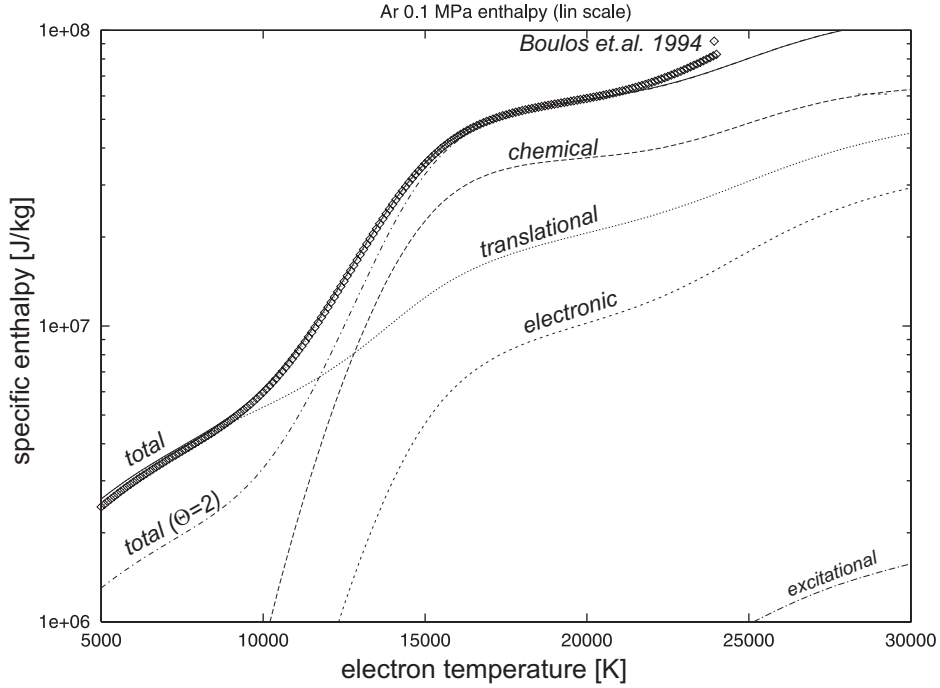


Figure 4.4: Specific enthalpy of a 0.1 MPa argon plasma plotted against electron temperature (for comparison, the data from [BFP94] are also plotted).

The high temperature enthalpy (figure 4.4) is dominated by chemical and translational enthalpy, while excitational enthalpy can be neglected.

4.2.6 Specific heat

Using the enthalpy computed above, the isobaric specific heat is given by

$$c_p = \left. \frac{\partial h}{\partial T} \right|_p \quad (4.2)$$

The temperature dependence of the specific heat reflects the different ionization levels within the plasma (figure 4.5).

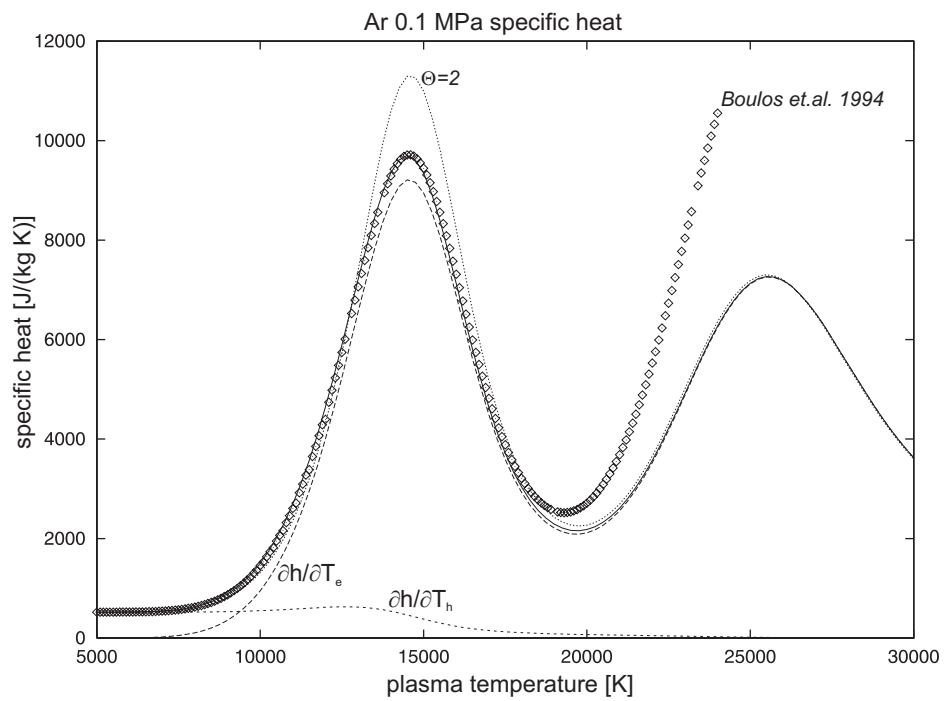


Figure 4.5: Specific heat of a 0.1 MPa argon plasma plotted against plasma temperature (for comparison, the data from [BFP94] are also plotted).

4.3 Particle collision integrals

The basic particle interactions (collisions) within the plasma are modeled by the calculation of so-called collision integrals. The interaction between the different particles within the plasma (atoms, ions and electrons) can be described by an interaction potential depending on the relative (kinetic) energy of the collision partners. The calculations assume binary instantaneous collisions. Details are described by Hirschfelder, Curtis and Bird [HCB64]. The collision integral of the order (l, s) is defined by [AF83]:

$$\bar{\Omega}^{(l,s)} = \frac{\bar{Q}^{(l,s)}}{\pi} = \frac{2(l+1)}{\pi(s+1)![2l+1-(-1)^l]} \times \int_0^\infty \exp(-X) X^{s+1} Q^l(\mathcal{E}) dX$$

where

$$\begin{aligned} X &\equiv \mathcal{E}/k_b T, \\ \mathcal{E} &\equiv \text{relative energy of the collision partners,} \\ Q^l(\mathcal{E}) &\equiv \text{elastic collision cross section.} \end{aligned}$$

For a number of simple interaction potentials, the collision integrals are tabulated relative to the hard sphere values or given by analytic approximations. Otherwise, the collision integrals are computed by numerical integration. In the following subsections, the different collision categories are discussed.

4.3.1 Neutral particle interaction

Collisions between neutral particles are modeled by a Lenard–Jones interaction potential

$$V(r) = 4k_b \tau_{LJ} \left[(\rho_{LJ}/r)^{12} - (\rho_{LJ}/r)^6 \right]$$

using tabulated values for the parameters τ_{LJ} and ρ_{LJ} [HCB64]. The advantage of this crude approximation is the availability of the interaction potential parameters for a large number of different plasma gases.

Compared to other estimates, the collision integrals for temperatures above 1600K (for Argon) deviate by less than 20% (see table 4.2 and [Kul71]). This will give slightly wrong values for the low temperature viscosity but has no remarkable effects regarding electrical and heat conductivity. For this interaction potential, the collision integrals can be related to the corresponding hard sphere values

$$\bar{Q}^{(l,s)} = \pi \rho_{LJ}^2 \cdot \Omega^{(l,s)*} \left(\frac{T}{\tau_{LJ}} \right)$$

using the $\Omega^{(l,s)*}$ function tabulated in [HCB64].

4.3.2 Charged particle interaction

Collisions between charged particles are modeled using a screened Coulomb potential. The collision integrals are tabulated [MMS67, Dev73]. Allowing for a deviation of about 15%, an analytical approximation can be used [Lib59]:

$$\bar{Q}_{ei}^{(1,s)} = \frac{4\pi b_0^2}{s(s+1)} \left(\log \frac{2\lambda_{\text{Debye}}}{b_0} - 2\bar{\gamma} + \sum_{i=1}^{s-1} \frac{1}{i} - 1/2 \right)$$

plasma gas:	Ar	Xe	Hg	Tl	I
Z [1]	18	54	80	81	53
m [u]	39.948	131.29	200.59	204.383	126.904
E^* [eV]	11.660	8.313	4.670		
E_{ion}^1 [eV]	15.755	12.130	10.434	6.1083	10.44
E_{ion}^2 [eV]	27.626	27.626	18.761	20.428	19.0
E_{ion}^3 [eV]	40.911	40.911	34.21	29.83	31.4
$\rho_{\text{LJ}} [10^{-10} \text{m}]$	4.055	3.465	2.898	4.055	4.320
$\tau_{\text{LJ}} [\text{K}]$	229	116	851	116	210.7
$Q_{0,\text{CT}} [10^{-20} \text{m}^2]$	7.5	48	12	17	5.6
$a_{\text{CT}} [1]$	0.13	0.14	0.11	0.12	0.16
$Q_{\text{en}}(E)$ ref.	[PP99]	[FP64]	[NL78]	[NL78]	[RG67]

Table 4.1: Basic plasma gas properties [And90, HCB64].

$$\bar{Q}_{\text{ei}}^{(2,s)} = \frac{12\pi b_0^2}{s(s+1)} \left(\log \frac{2\lambda_{\text{Debye}}}{b_0} - 2\bar{\gamma} + \sum_{i=1}^{s-1} \frac{1}{i} - 1 \right)$$

with $\bar{\gamma} = 0.577\dots$, $b_0 = \frac{Z_i Z_j e^2}{8\pi\epsilon_0 k_b T_e}$ and λ_{Debye} from equation 4.1.

4.3.3 Ion atom interaction

Charge exchange collisions between ions and atoms can be modeled by the heuristic interaction potential

$$Q_{\text{in}}(E[\text{eV}]) = Q_{0,\text{CT}} \cdot \left(1 + a_{\text{CT}} \cdot \log \frac{E_0}{E} \right)^2$$

where $Q_{0,\text{CT}}$ and a_{CT} are tabulated [And90] ($E_0 = 1\text{eV}$). While the sources of these data are not known to the author, the same principal dependencies investigated by [RF62] and compiled by [Wil96b] are used for this work.

These collisions dominate the collision integrals $\bar{Q}^{(l,*)}$ for even l . For odd l , Devoto has computed some values for argon. A comparison with the even l charge-exchange collision integrals gives a scaling factor of $1/4$, avoiding the extensive calculations done by Devoto and without the requirement of detailed atomic data. Alternatively, a simple polarisation model (dipole interaction) can be used [Wil96b].

4.3.4 Electron atom interaction

Electron atom collisions are highly affected by quantum mechanical matter wave inflection (Ramsauer effect). The cross sections can be measured [Iti78] or calculated [AC97]. The collision integrals are calculated numerically using cross section data from the literature (see figure 4.6).

4.3.5 Summary of particle collision modelling

Using the simplifications discussed above and the fundamental data provided in table 4.1, reasonable agreement with the more detailed computations of Devoto where found (table 4.2).

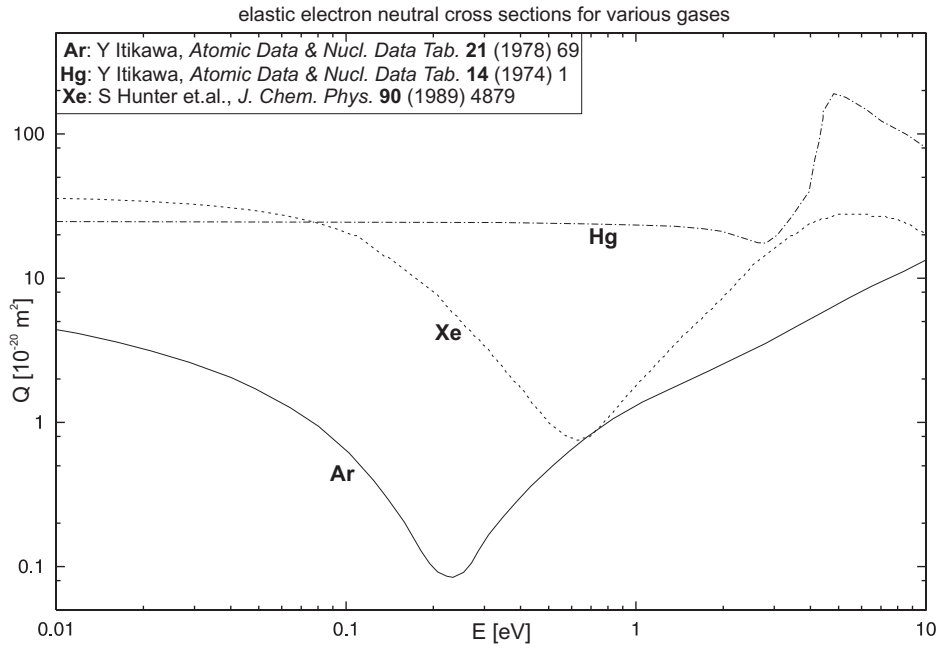


Figure 4.6: Elastic electron atom cross sections as a function of electron impact energy for Ar, Xe and Hg.

$T[\text{K}]$	$Q_{e,\text{Ar}^+}^{(1,1)}$		$Q_{\text{Ar},\text{Ar}}^{(2,2)}$		$Q_{\text{Ar},\text{Ar}^+}^{(1,1)}$		$Q_{\text{Ar},\text{Ar}^+}^{(2,2)}$		$Q_{e,\text{Ar}}^{(1,1)}$	
	Devoto	this work	Devoto	t.w.	Devoto	t.w.	Devoto	t.w.	Devoto	t.w.
5000	12200	11467	20.4	25.1	98.5	96	28.7	23	1.48	1.7
10000	1510	1281	17.6	22.7	87	89	23.2	21	3.46	3.5
20000	358	305	15	20.7	76.2	83	18.7	19.8	7.11	6.9

Table 4.2: Comparison of some collision integrals (in 10^{-20} m^2) with the values obtained by Devoto [Dev73] (Ar, $p=0.1 \text{ MPa}$).

This gives a sufficient accuracy for a large number of plasma gases where the basic data needed is available, while more sophisticated calculations like those of Devoto will require unaffordable efforts or will be even impossible due to missing fundamental data.

4.4 Energy exchange term for the pLTE model

4.4.1 Elastic energy exchange rate

The elastic energy exchange between electrons and heavy particles is computed by a mean collision frequency approach [BVY87, CZA96]:

$$\dot{E}_{eh}^{\text{elastic}} = 3/2 k_b(T_e - T_h) \cdot n_e \cdot \bar{v}_e^{\text{th}} \cdot \sum_i \left(\frac{2m_e}{m_i} \cdot n_i \bar{Q}_{ei} \right) .$$

Due to their small mass, the mean thermal velocity of the electrons is much higher and the heavy particles can be treated at rest. The sum is taken over all atom and ion plasma components and $\bar{v}_e^{\text{th}} = \sqrt{8k_b T_e / (\pi m_e)}$ is the electron mean thermal velocity.

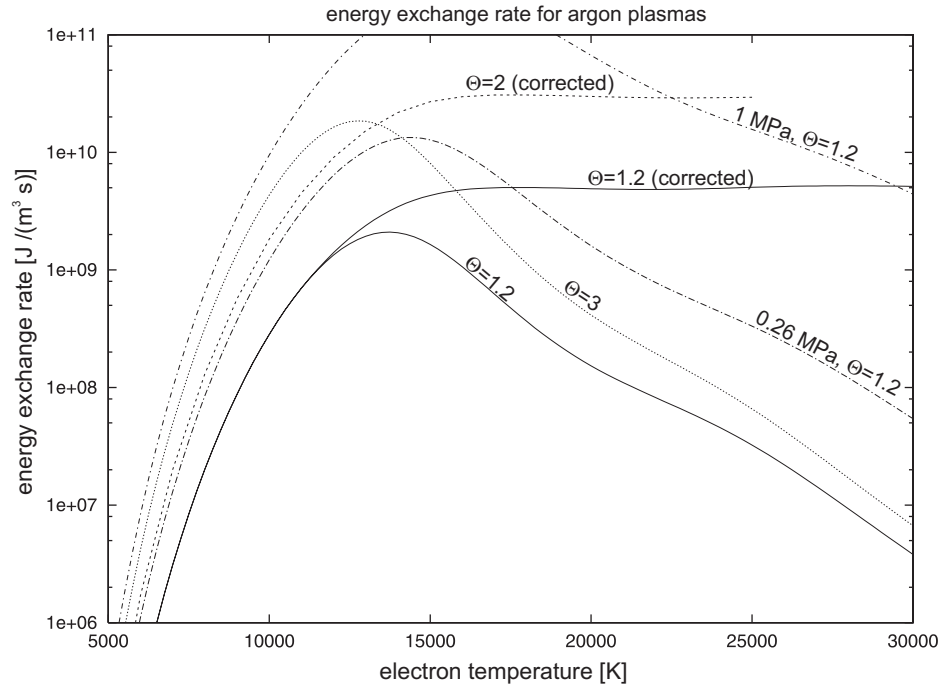


Figure 4.7: Energy exchange between the heavy particle and electron fluid (if not otherwise stated, the discharge pressure is 0.1 MPa).

The energy exchange (see figure 4.7) between the electron fluid and the heavy particles drastically increases with pressure.

4.4.2 Inelastic energy exchange rate

With increasing electron temperature, inelastic energy exchange between electrons and heavy particles should be taken into account. The detailed computation of this rate coefficient is extremely difficult. The principal dependency is

$$\dot{E}_{eh}^{\text{inelastic}} \sim n_e T_e^{-1/2} E_k$$

where E_k is the atomic or ionic energy level to be excited [BVY87]. Because these processes are important only for highly ionized plasmas, the total energy exchange rate is assumed to be increasing with temperature. The elastic decrease beyond a certain temperature (typically 15000K, see figure 4.7) is thus corrected.

4.5 Diffusities

The principal parameter dependencies of the diffusivities are [Wil96b]:

$$D \sim \frac{1}{p \cdot Q} \sqrt{\frac{T^3}{m}} \approx 10^{-5} \text{m}^2/\text{s}$$

The binary diffusion coefficient of two plasma species is given by [HCB64]:

$$D_{ij}^{\text{bin}} = \frac{3}{8} \cdot \frac{\sqrt{\pi}}{p \bar{Q}_{ij}^{(1,1)}} \cdot \sqrt{\frac{(k_b T)^3}{2\mu}}$$

with the reduced mass $\mu = (m_i \cdot m_j)/(m_i + m_j)$ and the total pressure p . From the binary diffusivities, the total diffusivity can be computed [HCB64]:

$$D_{ij} = \frac{\sum_{k=1}^N x_k m_k}{m_j} \cdot \frac{|K_{ji}| - |K_{ii}|}{|K|}$$

using

$$K_{ij} = \begin{cases} \frac{x_j}{D_{ij}^{\text{bin}}} + \frac{m_j}{m_i} \sum_{k \neq i} \frac{x_k}{D_{ik}^{\text{bin}}} & \text{for } i \neq j \\ 0 & \text{for } i = j \end{cases}$$

$|K_{ij}|$ is the sub determinant of the K matrix constructed by canceling the i th column and the j th row and multiplying with $(-1)^{j+i}$.

Ambipolar diffusivity

Because macroscopic space charge formation is not possible (quasineutrality condition), the flux of electrons and ions out of any region must be equal (neglecting the net total current). This coupling avoids independent diffusion of charged particles. The coupled diffusivity is called ambipolar diffusivity and given by [LL94]:

$$D_A = \frac{D_i \mu_e + D_e \mu_i}{\mu_e + \mu_i} .$$

Using the Einstein relation for the mobility and diffusivity ratio $\mu_\alpha/D_\alpha = e/(k_b T)$ and the fact of much higher electron mobility $\mu_e \gg \mu_i$, we get

$$D_A = D_i(1 + T_e/T_i)$$

For practical applications in high pressure discharges, the ambipolar diffusivity is almost identical to the ion-atom diffusivity D_{ia} .

4.6 Viscosity

The proportionality factor between momentum current and velocity gradient is called dynamic viscosity. The principal dependence on plasma parameters is as follows [Wil96b]:

$$\eta \sim \frac{\sqrt{mT}}{Q} \approx 10^{-5} \text{kg}/(\text{m s})$$

(viscosity is related to the self diffusivity by $D/\eta = \varrho$). The ratio of the dynamic viscosity and the mass density $\nu = \eta/\varrho$ is called kinematic viscosity. Here, we use the first approximation given by Hirschfelder *et.al.* [HCB64]:

$$\eta = \sum_{i=1}^N \frac{x_i^2}{\frac{x_i^2}{\eta_i} + 1.385 \sum_{\substack{k=1 \\ (k \neq i)}}^N x_i x_k \frac{k_b T_p}{p m_i D_{ik}}} \quad (4.3)$$

where p is the total pressure, x_i the molar fraction of the component i and η_i the viscosity of the pure gas component i .

$$\eta_i = \frac{5}{16} \sqrt{\pi k_b T_h m_i} \cdot \frac{1}{Q_{ii}^{(2,2)}}$$

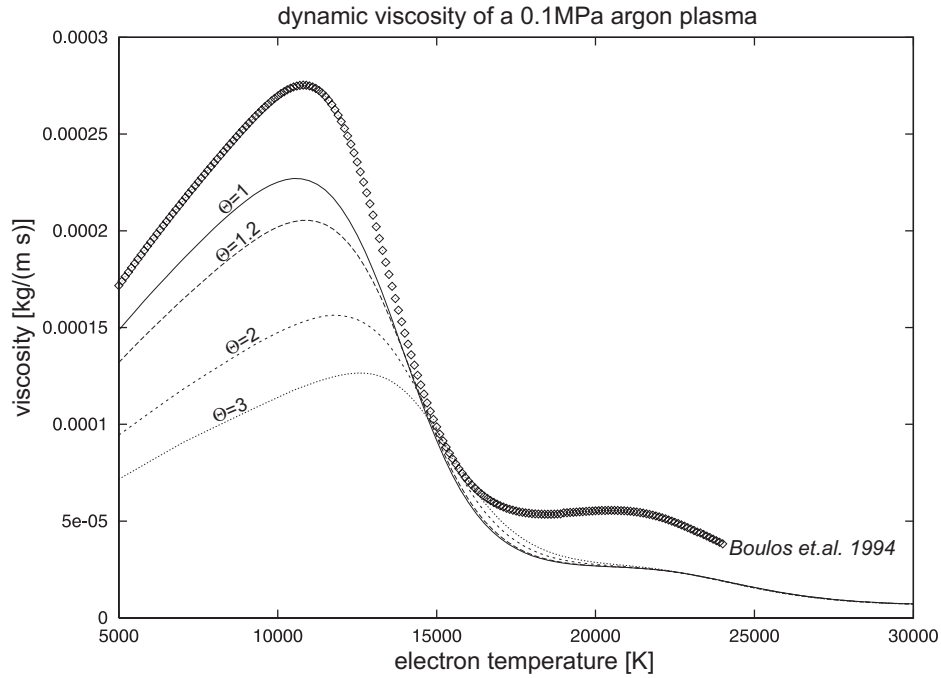


Figure 4.8: Viscosity of an atmospheric argon plasma (for comparison, the data from [BFP94] are also plotted).

The electronic contribution is less than 2 % and thus neglected [BFP94]. Due to this small influence of the electrons, viscosity decreases with increasing non-equilibrium parameter Θ (figure 4.8). The difference of the calculated viscosity to that provided by Boulos [BFP94] is due to different treatment of the atom-atom interaction.

4.7 Heat conductivity

Heat transport in thermal plasma gas discharges can be split into an electron contribution λ_e dominating the high temperature regime and a heavy particles contribution λ_h dominating the low temperature regime:

$$\lambda = \lambda_e + \lambda_h$$

Using only the dominating translational heat conductivity, the principal dependence on plasma parameters is as follows:

$$\lambda \sim \frac{1}{Q} \cdot \sqrt{\frac{T}{m}} \approx 1\text{W}/(\text{m K})$$

4.7.1 Electron heat conductivity

The electron heat conductivity is translational only and calculated using Devoto's 3rd approximation [Dev67]:

$$\lambda_e = \frac{75}{8} n_e^2 k_b \sqrt{\frac{2\pi k_b T_e}{m_e}} \cdot \frac{q^{(2,2)}}{q^{(1,1)}q^{(2,2)} - (q^{(1,2)})^2}$$

where

$$\begin{aligned} q^{(1,1)} &= 8\sqrt{2} n_e^2 \overline{Q_{ee}^{(2,2)}} + 8n_e \sum_{i=2}^N n_i \left(\frac{25}{4} \overline{Q_{ei}^{(1,1)}} - 15 \overline{Q_{ei}^{(1,2)}} + 12 \overline{Q_{ei}^{(1,3)}} \right), \\ q^{(1,2)} &= 8\sqrt{2} n_e^2 \left(\frac{7}{4} \overline{Q_{ee}^{(2,2)}} - 2 \overline{Q_{ee}^{(2,3)}} \right) \\ &\quad + 8n_e \sum_{i=2}^N n_i \left(\frac{175}{16} \overline{Q_{ei}^{(1,1)}} - \frac{315}{8} \overline{Q_{ei}^{(1,2)}} + 57 \overline{Q_{ei}^{(1,3)}} - 30 \overline{Q_{ei}^{(1,4)}} \right), \\ q^{(2,2)} &= 8\sqrt{2} n_e^2 \left(\frac{77}{16} \overline{Q_{ee}^{(2,2)}} - 7 \overline{Q_{ee}^{(2,3)}} + 5 \overline{Q_{ee}^{(2,4)}} \right) \\ &\quad + 8n_e \sum_{i=2}^N n_i \left(\frac{1225}{64} \overline{Q_{ei}^{(1,1)}} - \frac{735}{8} \overline{Q_{ei}^{(1,2)}} + \frac{399}{2} \overline{Q_{ei}^{(1,3)}} - 210 \overline{Q_{ei}^{(1,4)}} + 90 \overline{Q_{ei}^{(1,5)}} \right). \end{aligned}$$

The $i = 2 \dots N$ summation is taken over all heavy particles.

The heavy particles heat conductivity is calculated from the translational, reactive and internal contributions

$$\lambda_h = \lambda_h^{\text{trans}} + \lambda_h^{\text{react}} + \lambda_h^{\text{int}}$$

provided within the following subsections.

4.7.2 Heavy particles translational heat conductivity

Using the second approximation from [MC58], the translational heat conductivity of a multi-component plasma is given by

$$\lambda_h^{\text{trans}} = 4 \cdot \left| \begin{array}{cccc} L_{22} & \cdots & L_{2N} & x_2 \\ \vdots & \ddots & \vdots & \vdots \\ L_{N2} & \cdots & L_{NN} & x_N \\ x_2 & \cdots & x_N & 0 \end{array} \right| \bigg/ \left| \begin{array}{ccc} L_{22} & \cdots & L_{2N} \\ \vdots & \ddots & \vdots \\ L_{N2} & \cdots & L_{NN} \end{array} \right|$$

with

$$\begin{aligned}
x_i &= n_i/n_{\text{h,tot}} \quad \text{heavy particles molar ratio,} \\
L_{ii} &= -\frac{4x_i^2}{\lambda_{ii}} - \sum_{k=2}^N \frac{2x_i x_k}{A_{ik}^* \lambda_{ik} (m_i + m_k)^2} \left(\frac{15}{2} m_i^2 + \frac{25}{4} m_k^2 - 3m_k^2 B_{ik}^* + 4m_i m_k A_{ik}^* \right), \\
L_{ij} &= \frac{2x_i x_j m_i m_j}{A_{ik}^* \lambda_{ik} (m_i + m_j)^2} \left(\frac{55}{4} - 3B_{ij}^* - 4A_{ij}^* \right), \\
\lambda_{ij} &= \frac{75}{64} k_b \sqrt{\frac{\pi k_b T (m_i + m_j)}{2m_i m_j}} \cdot \frac{1}{\overline{Q}_{ij}^{(2,2)}}, \\
B_{ij}^* &= \frac{5\overline{Q}_{ij}^{(1,2)} - 4\overline{Q}_{ij}^{(1,3)}}{\overline{Q}_{ij}^{(1,1)}}, \\
A_{ij}^* &= \frac{\overline{Q}_{ij}^{(2,2)}}{\overline{Q}_{ij}^{(1,1)}}.
\end{aligned}$$

4.7.3 Heavy particles internal heat conductivity

Due to the variation of the excitation of the internal degrees of freedom of the plasma components with temperature, a corresponding heat conductivity can be defined [AF83]:

$$\lambda_{\text{h}}^{\text{int}} = \sum_{i=2}^N (\lambda_{\text{I}})_i \left(\sum_{j=2}^N \frac{x_j D_{ii}}{x_i D_{ij}} \right)^{-1}$$

with

$$\begin{aligned}
(\lambda_{\text{I}})_i &= \frac{n D_{ii}}{N_{\text{av}}} \left(c_p(i) - \frac{5}{2} R \right) \quad i\text{-th internal heat conductivity} \\
D_{ii} &\quad \text{binary diffusivity} \\
c_p(i) &\quad \text{specific heat of the } i\text{-th component.}
\end{aligned}$$

This contribution is at least one order of magnitude below translational and reactive heat conductivity and can be safely neglected.

4.7.4 Heavy particles reactive heat conductivity

Diffusive particle transport in a fluid with chemical reactions (like ionization and recombination) lead to the transport of chemical enthalpy. The corresponding heat conductivity is taken from [BB57, Bro60]. Taking R chemical reactions (incl. ionization) into account, it is given by:

$$\lambda_{\text{h}}^{\text{react}} = -\frac{\Theta}{RT_e^2} \left| \begin{array}{cccc} A_{11} & \cdots & A_{1R} & h_1 \\ \vdots & \ddots & \vdots & \vdots \\ A_{R1} & \cdots & A_{RR} & h_R \\ h_1 & \cdots & h_R & 0 \end{array} \right| \bigg/ \left| \begin{array}{ccc} A_{11} & \cdots & A_{1R} \\ \vdots & \ddots & \vdots \\ A_{R1} & \cdots & A_{RR} \end{array} \right|$$

with

$$\Theta = T_e/T_h \text{ (introduced by [BAM85])}, \quad (4.4)$$

$$A_{ij} = A_{ji} = \sum_{k=1}^{R-1} \sum_{l=k+1}^R \frac{R T_e x_k x_l}{p D_{kl}^{\text{bin}}} \left(\frac{r_{ik}}{x_k} - \frac{r_{il}}{x_l} \right) \left(\frac{r_{jk}}{x_k} - \frac{r_{jl}}{x_l} \right),$$

$$h_i = \sum_{k=1}^N r_{ik} h_k m_k N_{\text{Av}} \quad i \in [1, \mu] \quad \text{reaction enthalpy per mol,}$$

$$r_{ik} \quad \text{reaction matrix.}$$

As shown in figure 4.9, the total plasma heat conductivity $\lambda_e + \lambda_h$ is in reasonable agreement with literature data and not strongly affected by the non-equilibrium parameter Θ . The heavy particles heat conductivity is strongly affected by the reactive peak due to the onset of ionization.

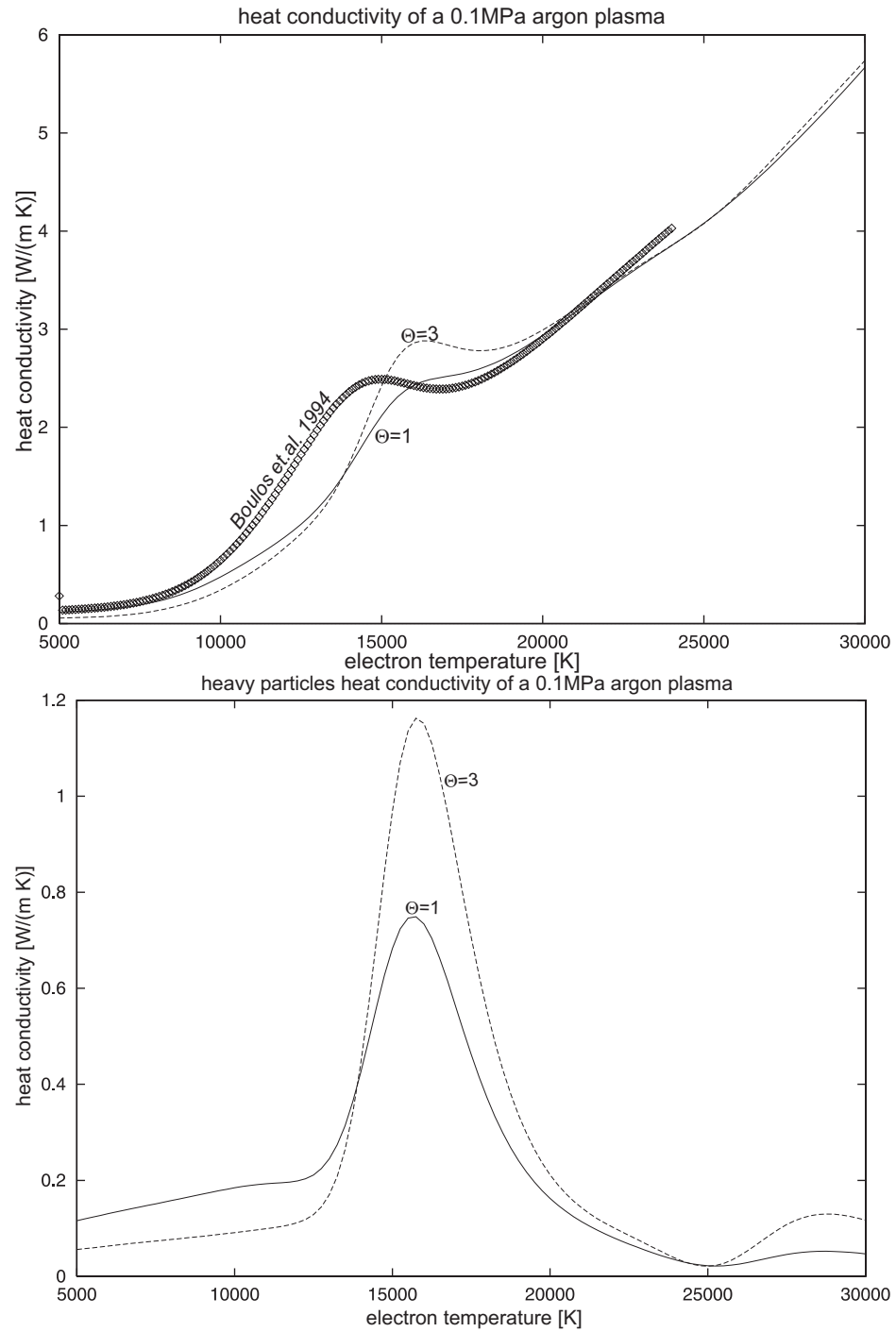


Figure 4.9: Total (top) and heavy particles (bottom) heat conductivity of an atmospheric argon plasma.

4.8 Electric conductivity

In high density plasmas with low ionization degree, the electric conductivity is determined by electron mobility and electron density, thus the principal dependencies are:

$$\sigma \sim \frac{n_e \cdot \sqrt{T}}{p \cdot Q_{ea}} \leq 5 \cdot 10^4 \text{S/m}$$

Here, the electric conductivity is calculated using the approximations of Devoto [Dev67]:

$$\sigma = {}^{3/2} \sqrt{\frac{2\pi}{m_e k_b T_e}} \cdot e^2 \cdot n_e^2 \cdot \frac{1}{q^{(1,1)} q^{(0,0)} - (q^{(0,1)})^2}$$

where

$$\begin{aligned} q^{(0,0)} &= 8n_e \sum_{i=2}^N n_i \overline{Q_{ei}^{(1,1)}} , \\ q^{(0,1)} &= 8n_e \sum_{i=2}^N n_i \left(\frac{5}{2} \overline{Q_{ei}^{(1,1)}} - 3 \overline{Q_{ei}^{(1,2)}} \right) , \\ q^{(1,1)} &= 8\sqrt{2} n_e^2 \overline{Q_{ee}^{(2,2)}} + 8n_e \sum_{i=2}^N n_i \left(\frac{25}{4} \overline{Q_{ei}^{(1,1)}} - 15 \overline{Q_{ei}^{(1,2)}} + 12 \overline{Q_{ei}^{(1,3)}} \right) \end{aligned} \tag{4.5}$$

(the sum is taken over all particles except the electrons). For molecular gases, in the lower temperature range, the electron molecule interaction has to be considered [CG98].

As an example, the temperature dependence of the electric conductivity is shown in figure 4.10. There is no significant Θ -dependence and excellent agreement with literature data.

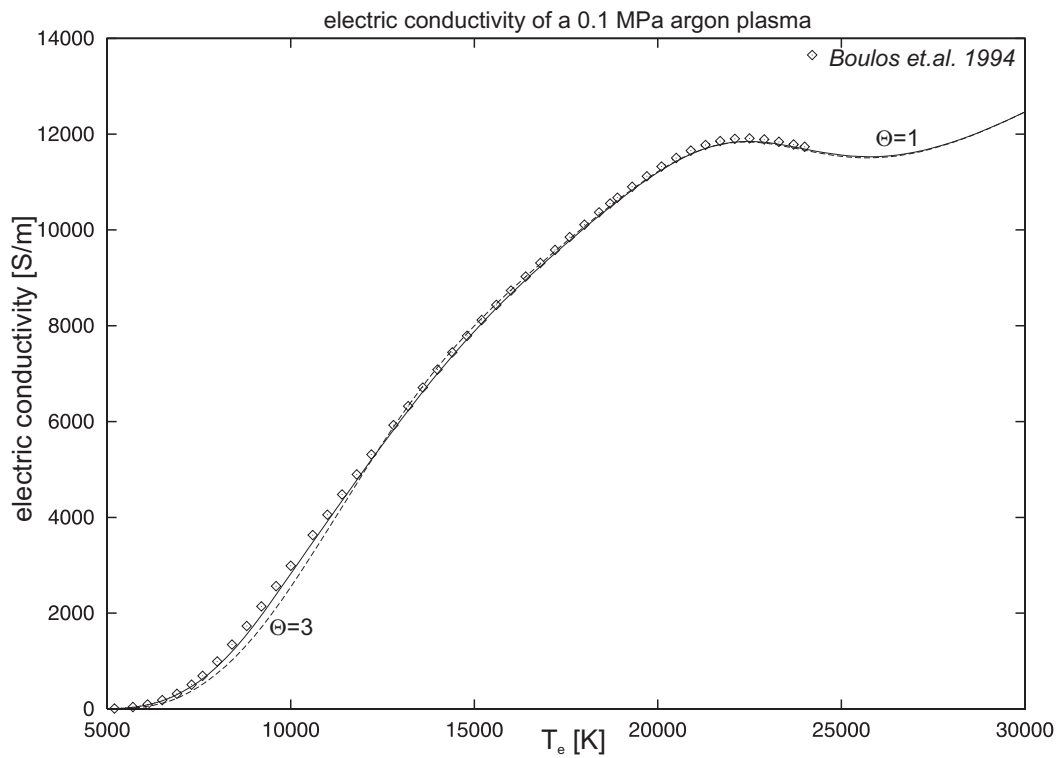


Figure 4.10: Electric conductivity of an atmospheric argon plasma plotted against electron temperature for 2 different values of the non-equilibrium parameter Θ (for comparison, the data published in [BFP94] are also plotted).

4.9 Simple treatment of radiation effects

In general, the effective radiation emission is computed by subtracting spectrally integrated emission and absorption :

$$S_{\text{rad}}(T_e, \vec{r}) = 4\pi \int_{\lambda} \varepsilon_{\lambda} d\lambda - \int_{\lambda} a_{\lambda} d\lambda$$

Because the numerical effort for a detailed treatment of the radiation transport is tremendous [MHP99], an effective net radiation emission coefficient as described by Lowke [Low74] is used for this work. The net radiation loss function $S_{\text{rad}}(T_e)$ was computed at the University of Karlsruhe [Thr98] by integration of the specific spectral radiation emissivity ε_{λ} :

$$S_{\text{rad}}(T_e) = 4\pi \int_{\lambda} \varepsilon_{\lambda} d\lambda$$

The following radiation emission mechanisms are taken into account:

$$\begin{aligned} \varepsilon_{\lambda}^{\text{bb}} &: \text{optical thin line radiation} \\ \varepsilon_{\lambda}^{\text{fb}} &: \text{recombination radiation} \\ \varepsilon_{\lambda}^{\text{ff}} &: \text{ion and atom Bremsstrahlung} \end{aligned}$$

The line emission coefficient $\varepsilon_{\lambda}^{\text{bb}}$ denotes the radiated power per solid angle, which stems from spontaneous radiative transition between two discrete energy levels. In LTE it depends on the population density of the upper level E_k , when the transition probability A_{ki} is known, and reads

$$\varepsilon_{\lambda}^{\text{bb}} = \frac{h\nu}{4\pi} A_{ki} n_z(T) \cdot \frac{g_k}{U_z(T)} \cdot \exp\left[-\frac{E_k}{k_b T}\right]$$

n being the density, g_k the statistical weight of level k in the ionization state z and U_z the partition function. In general, the wavelength dependence of the radiated power can be denoted by

$$\varepsilon_{\nu} = P(\nu) \varepsilon_L \quad , \quad \int_{\text{Line}} P(\nu) d\nu = 1 \quad ;$$

with $P(\nu)$ a normalized profile. Stark and possibly van der Waals broadening often dominate the line profile in high pressure arcs, while Doppler broadening plays a minor role because of the relatively low temperatures.

The continuum radiation arises from recombination (free-bound) and bremsstrahlung (free-free) transitions and is usually given in terms of hydrogen, with appropriate correction factors, the so-called Bibermann factors ξ . For a high-pressure plasma the contribution of electron-atom encounters has also to be taken into account, and the continuum emission coefficient becomes

$$\varepsilon_C = \varepsilon_{\text{ff}}^{\text{ei}} + \varepsilon_{\text{ff}}^{\text{ea}} + \varepsilon_{\text{fb}}$$

The terms can be calculated from [BP97b]

$$\begin{aligned} \varepsilon_{\text{ff}}^{\text{ei}} &= \frac{1}{(4\pi\epsilon_o)^3} \frac{16\pi e^6}{3c^3 \sqrt{6\pi m_e^3 k_b}} \sum_z \frac{n_e n_z}{\sqrt{T_e}} z^2 \exp\left(-\frac{h\nu}{k_b T_e}\right) \xi_{\text{ff}}(\nu, T_e, z) \\ \varepsilon_{\text{ff}}^{\text{ea}} &= \frac{1}{4\pi\epsilon_o} \frac{32e^2}{3c^3} \left(\frac{k_b}{2\pi m_e}\right)^{3/2} n_a n_e T_e^{3/2} Q_{\text{ea}}(T_e) \end{aligned}$$

$$\begin{aligned} & \times \left\{ \left(1 + \frac{h\nu}{k_b T_e} \right)^2 + 1 \right\} \exp \left(-\frac{h\nu}{k_b T_e} \right) \\ \varepsilon_{fb} = & \frac{1}{(4\pi\epsilon_o)^3} \frac{16\pi e^6}{3c^3 \sqrt{6\pi m_e^3 k_b}} \sum_z \frac{n_e n_z}{\sqrt{T_e}} z^2 \\ & \times \left\{ 1 - \exp \left(-\frac{h\nu}{k_b T_e} \right) \right\} \frac{g_{z,1}}{U_z} \xi_{fb}(\nu, T_e, z) \end{aligned}$$

In figure 4.11, the net radiation emission coefficients calculated in Karlsruhe are visualized. Doping the discharge medium with low ionization potential materials can have a strong effect on the radiative properties at lower temperatures. The radiation source strength at a specific plasma temperature linearly increases with pressure [Bau62].

For the optical thick radiation an effective radiative heat conductivity can be calculated [AN72, MHP99, Wil96a]. Recently, a full treatment of the radiation problem came into the range of treatable models [MHP99].

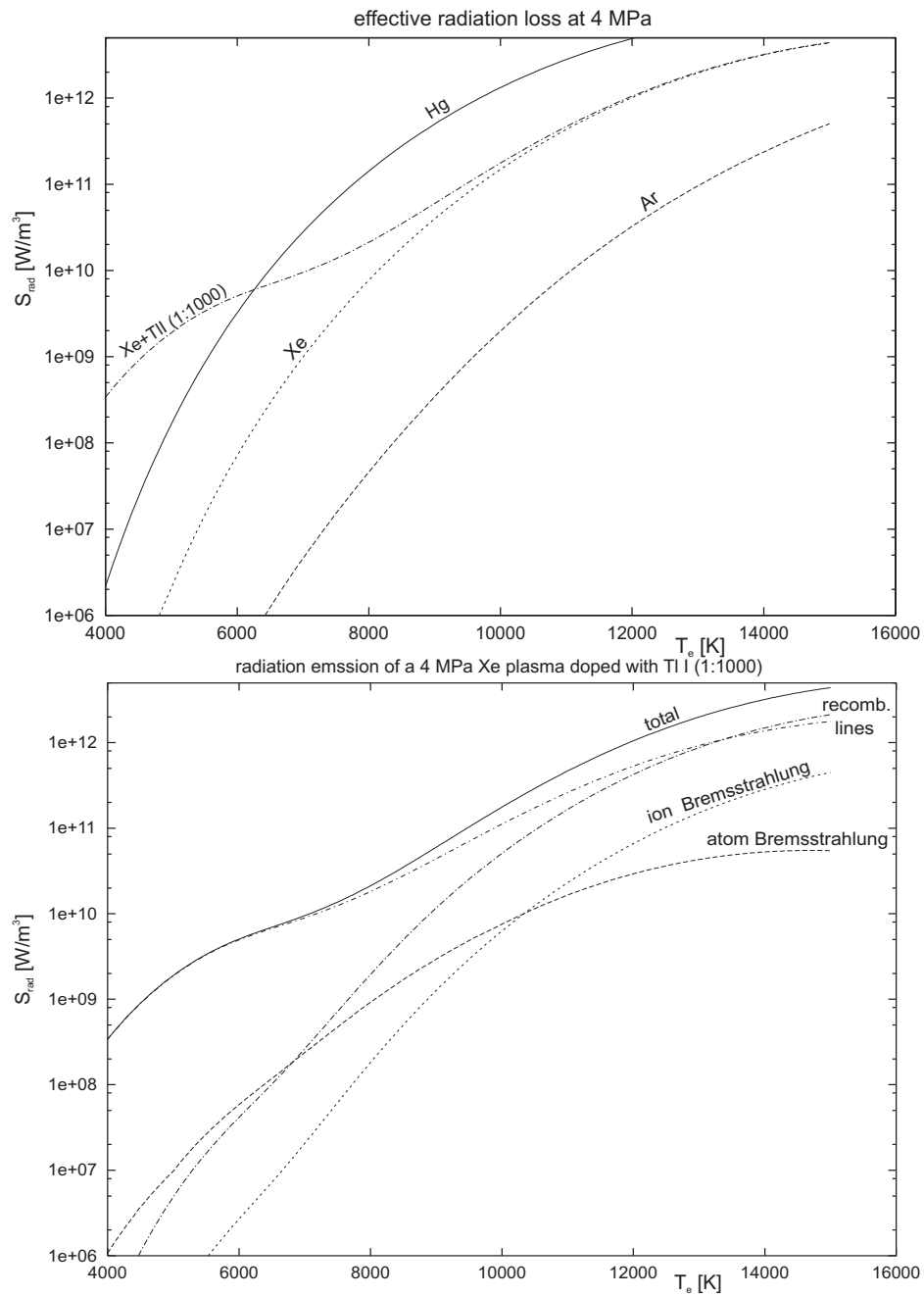


Figure 4.11: Net radiation emission coefficient of a 4 MPa xenon plasma doped with Thallium-iodide (bottom) and comparison with pure Ar, Xe and Hg plasmas (top).

4.10 Simple treatment of ionization non-equilibrium

For a number of applications, the thermal plasma is not in ionization equilibrium. The ionization rate is proportional to electron and atom density, recombination is mainly a three particle reaction $A^+ + e + e \rightarrow A^* + e$. The net ionization rate is defined to be

$$\dot{n}_e = \beta_{\text{ion}} n_e n_a - \alpha_{\text{rec}} n_e^2 n_i$$

Using $\dot{n}_{e,\text{LTE}} = 0$, the ionization rate can be expressed in terms of the recombination rate and the net ionization rate becomes:

$$\dot{n}_e = \alpha_{\text{rec}} n_e^3 \cdot \left[\left(\frac{n_{e,\text{LTE}}}{n_e} \right)^2 \cdot \left(\frac{n_a}{n_{a,\text{LTE}}} \right) - 1 \right]$$

Following the detailed computation of the recombination rate coefficient [BN98], one can use the following simple approximation [HL67]:

$$\alpha_{\text{rec}} = 1.29 \cdot 19^{-44} \left(\frac{E^*}{k_b T_e} + 2 \right) e^{\frac{E_{\text{ion}} - E^*}{k_b T_e}} \quad [\text{m}^6/\text{s}]$$

E_{ion} is the ionization energy and E^* can be identified with the energy of the first excited level (see table 4.1).

4.11 Sensitivity analysis of the transport coefficients and their influence on the resulting discharge parameters

Tr. Coeff.	100% Value	Q_{ea}	Q_{CT}	$Q_{\text{Coul.}}$	Q_{aa}
$\sigma(T = 5\text{kK})$	26 S/m	-0.9	0.0	-0.1	0.0
$\sigma(T = 7.5\text{kK})$	940 S/m	-0.5	0.0	-0.5	0.0
$\sigma(T = 10\text{kK})$	3390 S/m	-0.3	0.0	-0.7	0.0
$\kappa(T = 5\text{kK})$	0.04 W/(m K)	0.0	0.0	0.0	-1.0
$\kappa(T = 7.5\text{kK})$	0.11 W/(m K)	-0.3	0.0	-0.2	-0.5
$\kappa(T = 10\text{kK})$	0.42 W/(m K)	-0.3	-0.2	-0.4	-0.1
$\nu(T = 5\text{kK})$	$1.8 \cdot 10^{-4}$ kg/(m s)	0.0	0.0	0.0	-1.0
$\nu(T = 7.5\text{kK})$	$2.3 \cdot 10^{-4}$ kg/(m s)	0.0	0.0	0.0	-1.0
$\nu(T = 10\text{kK})$	$2.2 \cdot 10^{-4}$ kg/(m s)	0.0	-0.2	0.0	-0.8

Table 4.3: Sensitivity of the plasma transport coefficients on cross section data (LTE xenon plasma at 1 MPa).

The sensitivity gives the principal dependency of the transport coefficient or arc parameter f on the cross section data Q :

$$f(Q) = f(Q_0) \cdot \left(\frac{Q}{Q_0} \right)^s$$

parameter	100% Value	all Q 's	Q_{ea}	Q_{ia}	Q_{ee}	Q_{aa}
V_{arc}	11.8 V	0.2	0.2	± 0.02	0.1	-0.1
$V_{C,\text{el.}}$	8.0 V	0.2	0.2	± 0.03	0.2	-0.3
$V_{A,\text{el.}}$	2.7 V	0.2	0.0	± 0.01	-0.1	0.3
$E_{\text{col.}}$	882 V/m	0.6	0.4	± 0.01	0.1	± 0.1
$T_{\text{col.}}$	7444 K	0.1	0.05	0.0	0.0	0.04
$T_{C,\text{max.}}$	3306 K	0.0	0.0	0.0	0.0	0.0
$v_{\text{max.}}$	0.5 m/s	0.5	0.2	± 0.02	-0.02	0.6
$S_{\text{rad,max.}}$	$5.7 \cdot 10^9 \text{ W/m}^3$	1.8	1.2	± 0.06	0.2	-0.1
rad. yield	0.3	0.8	0.4	± 0.03	0.1	0.3

Table 4.4: Sensitivity of basic arc parameters on cross section data (discharge configuration: see figure 5.1).

For the transport coefficients, the sensitivity is trivial (table 4.3: They are proportional to $1/Q$ ($s = -1$)). The electric conductivity depends on Q_{ea} for low ionization degrees and on Q_{Coul} , for higher ionization degrees. The total plasma heat conductivity depends on Q_{aa} for low and on all Q 's for high ionization degrees. Viscosity is dominated by atom-atom interaction (Q_{aa}). The influence of cross section data on the basic arc properties is shown in table 4.4. Decreasing or increasing the numerical values of the cross sections (e.g. by multiplication with 1.5), normally changes most arc properties by less than 20%. The column electric field (and thus the arc voltage for longer arcs) more strongly depends on electron-atom interaction (Q_{ea}). Global arc parameters with strong temperature dependencies like the radiative properties show more significant changes with changing cross sections, especially the Ramsauer data (Q_{ea}) can have remarkable influences. Because the complex and nonlinear nature for the arc-electrode system, such sensitivities will also depend on the specific discharge situation and can be calculated only for small deviations from a given parameter set.

Intellektuelle Erkenntnisse sind Papier.
Vertrauen hat immer nur der,
der von Erfahrenem redet.

H. Hesse

Chapter 5

Modelling results, validation and sensitivity analysis

5.1 Introduction

In the previous chapters, a self consistent physical model of the complete arc discharge was developed (chapter 3). The necessary plasma transport coefficients were computed (chapter 4), and the basis of the numerical calculation schemes was discussed (chapter 2).

This chapter will first show detailed results predicted for a simple (in terms of geometry and computing time) discharge configuration. This will give an impression of the discharge properties emerging from the interaction of the different physical processes discussed in chapter 3. The influence of the details of the physical model on the overall discharge behaviour will become evident from a physical sensitivity analysis.

By a variation of the fundamental arc parameters like current, gas, pressure and cathode properties, the model will prove its ability to reproduce all major discharge features. The discharge properties visualized for these parameter studies are mostly obtainable by experiment. Thus the results can be regarded as predictions of future measurements.

The experimental validation of the model will be discussed in further detail and some comparisons with existing measurement data will be presented.

5.2 Detailed properties computed for a representative arc configuration (model lamp)

The computational effort (logical depth) of the numerical solution for the complete arc model is tremendous. It scales with the spatial dimensions of the discharge and the dimensions of the electrodes. Very high current densities within the cathode hot spot require numerical parameters (e.g. the virtual time step) far beyond the capability of current computers. The *model lamp* was therefore selected to be relatively small. Nevertheless, it can be realized experimentally and the results are very useful for the understanding of a large and economically important class of thermal plasma gas discharges, the high pressure arc lamps, also called **High Intensity Discharges**.

In figure 5.1, the *model lamp* configuration is sketched and the fundamental parameters and boundary conditions are provided. If not otherwise stated, the numerical calculations include the following effects:

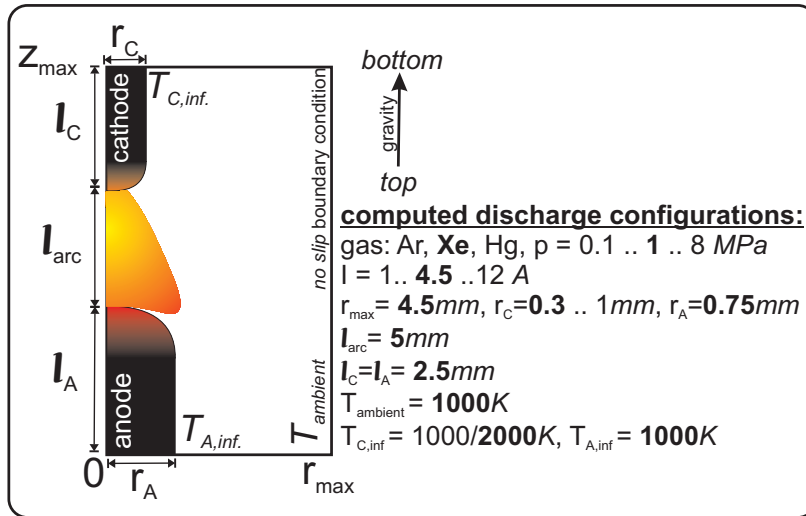


Figure 5.1: Arc discharge configuration used for the calculations. The default parameter values are typed in boldface.

- Inside the electrodes, the two dimensional heat conduction equation is solved (section 3.2).
- Electron emission is described by the Richardson/Schottky formula (section 3.3.1). The theoretical value of the Richardson constant A_R is used.
- Cathode sheath and presheath phenomena are taken into account as described in sections 3.3.2 and 3.3.4.
- All cathode heating processes described in section 3.3.6 are taken into account.
- The anode layer is included by applying the simple sheath model description from section 3.4.
- Mass continuity and momentum balance are included by solving the Navier-Stokes equations (3.8) and (3.10).
- The complete two temperature heat balances are solved (section 3.5.2.2).
- Current transport is computed from Ohm's law and current continuity equation (3.18).
- The magnetic field is computed from equation (3.19).
- The plasma transport coefficients were calculated for the partial LTE case as described in chapter 4.

All these equations are solved within the iterative procedure sketched in figure 5.2. The geometry is always cylindrical, and the numerical grid is non equidistant.

Ab-initio electric arc modelling procedure:

Input data:

- discharge current,
- discharge gas (Ar, Xe, Hg, ..), pressure (0.1 .. 8 MPa) & geometry [arc- and electrode lengths, bulb- & electrode geometry],
- electrode materials (anode & cathode) and its properties [heat conductivity $\lambda(T)$, el. cond. $\sigma(T)$, work function Φ_C , $\epsilon_{rad}(T)$].

Plasma composition and transport coefficients

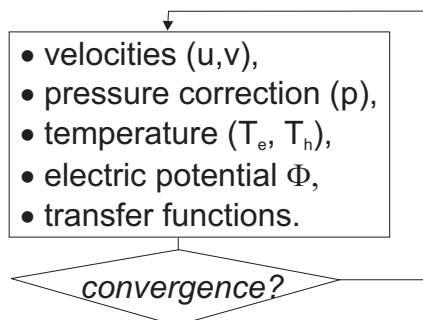
(as a function of T_e and T_h or T_e and $\Theta = T_e/T_h$):

- partition function calculation (requires energy levels),
- plasma density, enthalpy and specific heat,
- plasma transport coefficients (conductivities, etc.).

Initial values, e.g.:

- data from similar calculations (scaled),
- data from calculations with prescribed hot spot current density,
- artificial plausible temperature distributions.

Main iteration procedure:



Results output and visualization:

- global arc quantities: voltage, radiated power, etc.,
- $u(r,z)$, $v(r,z)$, $p(r,z)$, $T_{e,h}(r,z)$, $\Phi(r,z)$, sheath voltage distributions,
- cathode- & anode fall voltages, • other derived quantities.

Figure 5.2: Arc discharge modelling *set-up*.

5.2.1 Properties of the overall discharge

First of all, the spatial distribution of the plasma temperatures and the flow field within the discharge is visualized in figure 5.3. Regarding fluid flow, the driving forces within the *model lamp* are mainly natural convection (gravity) and the magnetic compression resulting from the high current densities near the cathode and anode hot spot. For a lamp burning vertically with the cathode at the bottom, convection is dominated by a flow vortex with the center in a torus around the arc. The magnetic forces due to the constriction of the arc current within the near anode plasma act against the cathode and the buoyant jet coming from the cathode at the bottom. As a result, a second vortex structure emerges around the anode (top of figure 5.3). Because of the high impact of convective heat transport, the arc temperature distribution follows the flow field. Finally, the temperature map looks like a reversed bulb. For this plasma gas (xenon) and discharge pressure level (1 MPa) and current (4.5A), the arc is mostly in LTE ($T_e = T_h$). Near the electrode surfaces, the electron temperature decouples from the heavy particles temperature. This thermal boundary layer results from the thermal isolation of the electron fluid due to sheath effects, while the heavy particles equilibrate with the electrode solid.

Reversing the burning position of the arc (figure 5.4, bottom), a similar temperature map results, but the cathode and anode exchange their roles. Due to the higher impact of the cathode jet now working against natural convection, the overall flow field is more complex. There are three major vortex structures emerging: The main vortex around the center of the discharge is smaller, and has two child vortices at the bottom. The vortex around the cathode at the top is larger and the overall flow field will be more sensitive to disturbances.

Neglecting buoyancy (gravity) effects, the impact of the flow field on the arc temperature map is smaller and a two vortex structure emerges (figure 5.4, top).

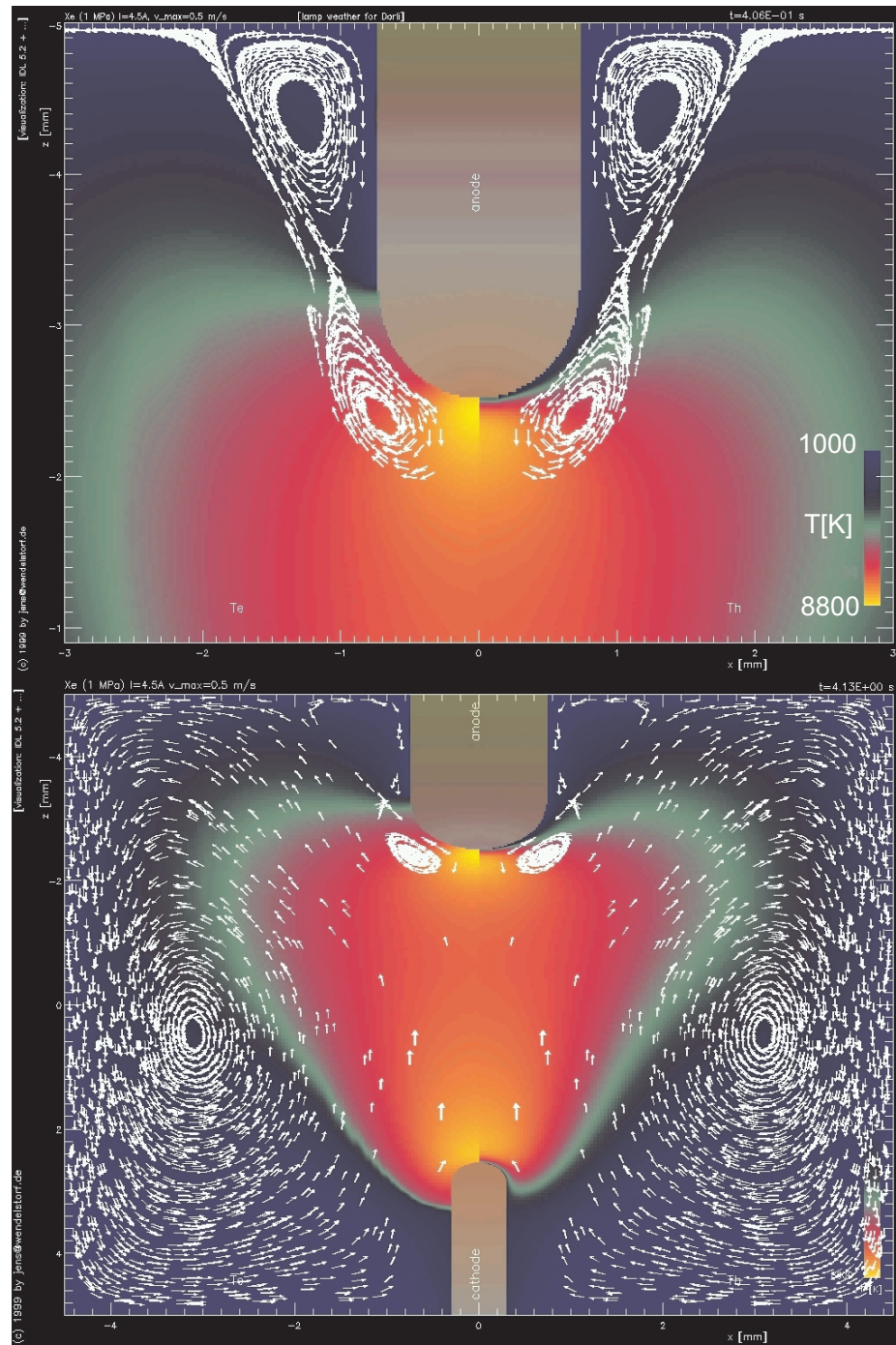


Figure 5.3: Plasma temperatures (left side: T_e , right side: T_h) and flow field of a 4.5A, 1 MPa xenon arc discharge. The vortex resulting from the anode jet is enlarged on the top.

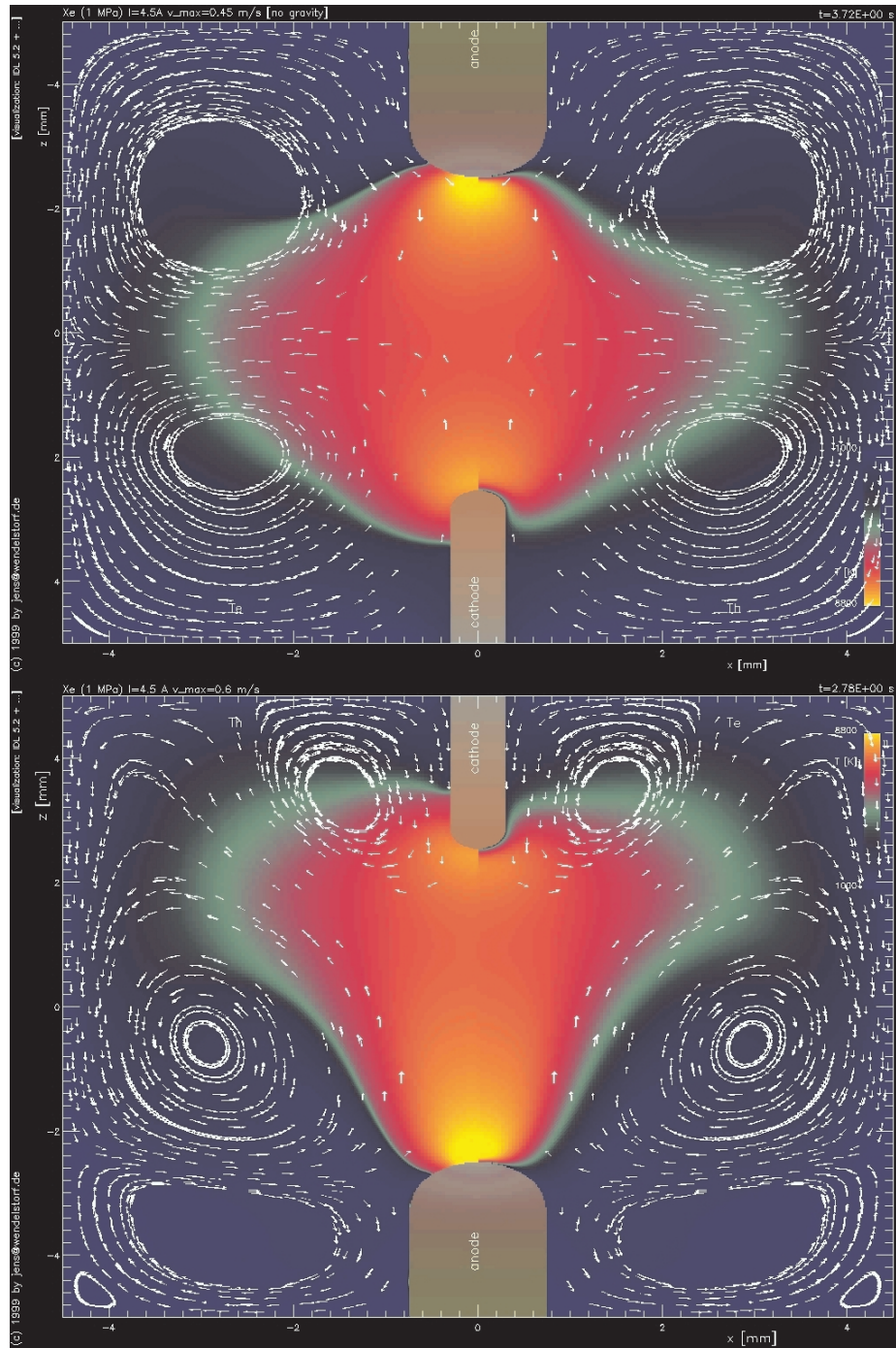


Figure 5.4: Plasma temperatures (left side: T_e , right side: T_h) and flow field of a 4.5A, 1 MPa xenon arc discharge burning with the anode at the bottom and without gravity effects (top) .

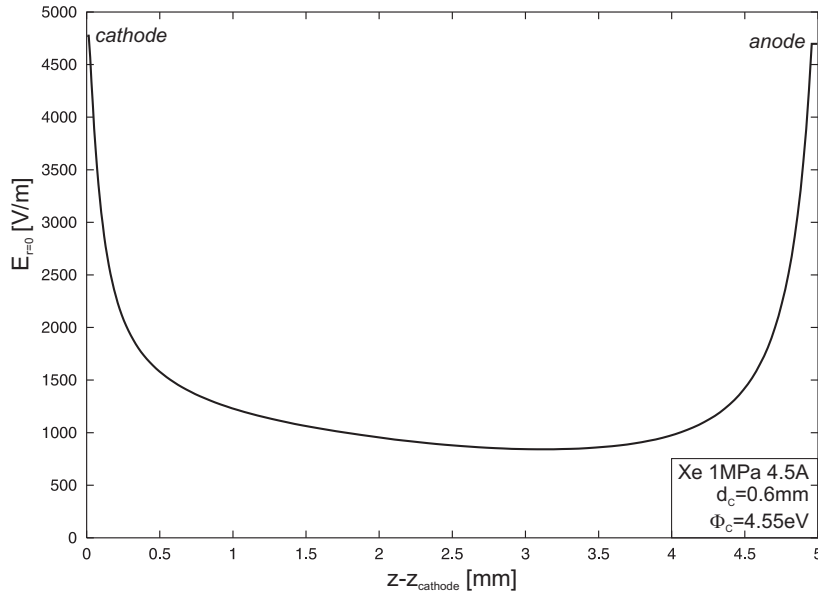


Figure 5.5: Electric field on the axis of a 1 MPa xenon arc discharge.

The spatial temperature and velocity distribution of the arc (figure 5.3) is mainly caused by the spatial distribution of the electrical quantities visualized in figure 5.6. The upper left picture shows the electric potential distribution within the arc electrode system. The main voltage drop is located in the space charge layer around the cathode surface. The anode sheath model used here, delivers a self consistent negative space charge layer voltage drop around the anode surface. This voltage drop is limiting the diffusive electron current from the plasma to the prescribed total current level and a current density level determined by the electric conductivity of the near anode plasma. The upper right picture gives an impression on the spatial distribution of the electric conductivity within the arc electrode system. Because the conductivity of the solid electrodes is several orders of magnitude larger than that of the thermal plasma, the conductivity drop gives rise to the important sheath effects included into the model. The picture at the bottom provides an impression of the current constriction within the cathode and anode hot spot. The resulting high electrical current densities lead to the magnetic compression forces driving the flow field within these areas.

The electric field strength on the arc axis is plotted in figure 5.5. Near the cathode and anode surface, the plasma constriction requires electric fields around 4500 V/m, while the electric field in the arc center is rather small (geometrical decompression in the column). In this region, the current carrying area is much larger (the sheath induced electric fields at the electrode surfaces are not visualized here).

The axial plasma temperature distribution (figure 5.7) allows to estimate the thickness of the thermal boundary layer near the electrodes, where non LTE effects occur. The high electrode hot spot current densities increase the ohmic heating of the plasma. As a result, the plasma temperature shows two maxima within the thermal boundary layers at the electrodes.

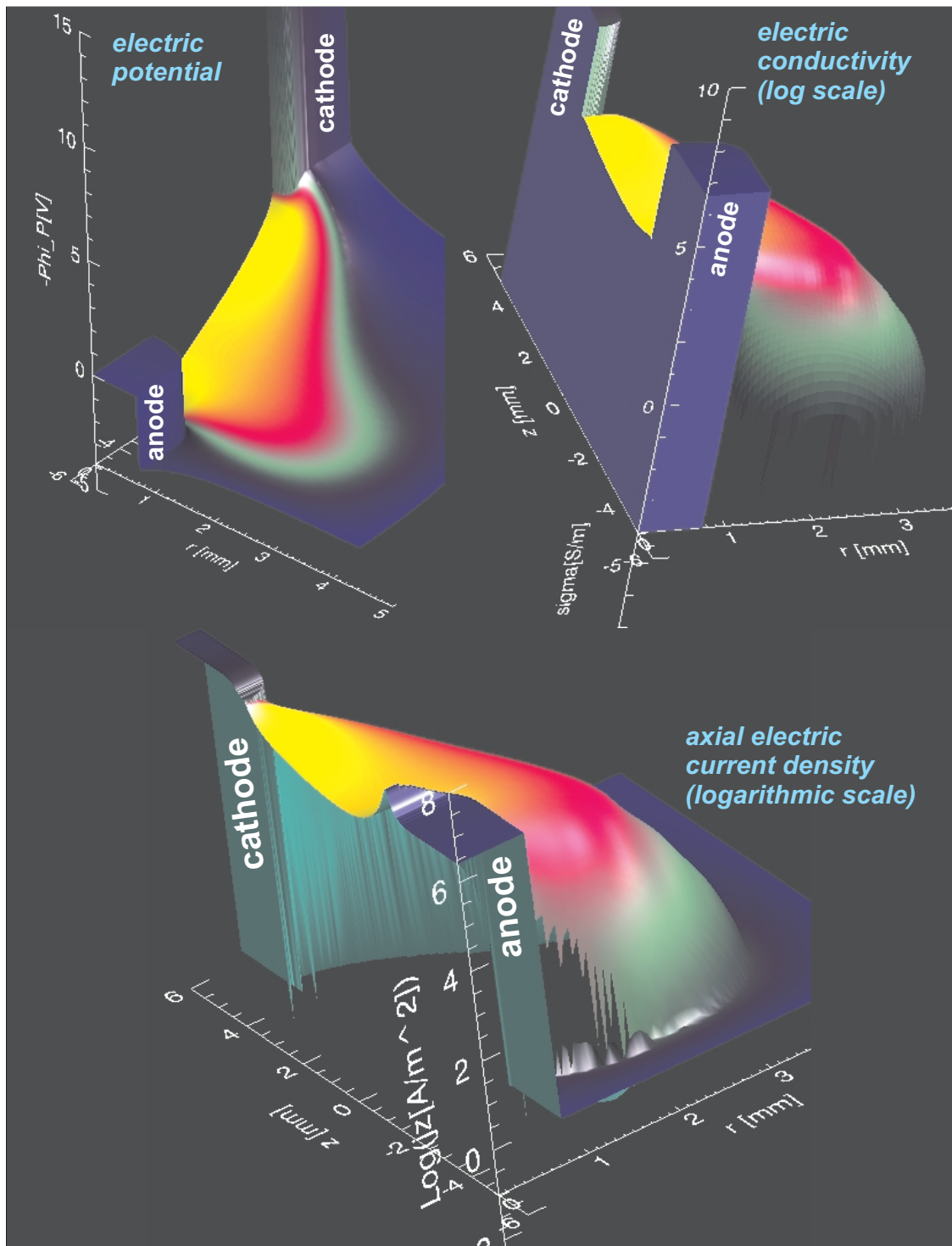


Figure 5.6: Electric quantities of a 1 MPa xenon arc discharge ($I=4.5\text{A}$).

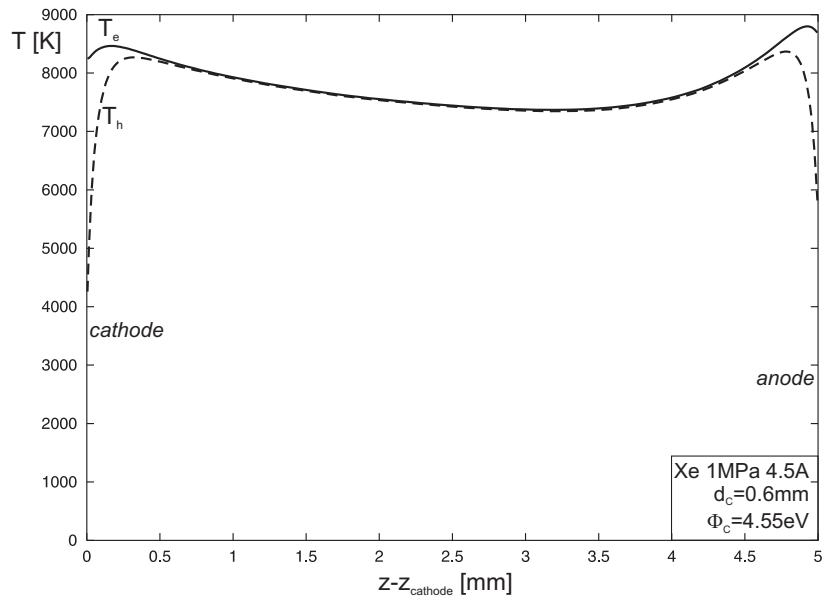


Figure 5.7: Electron and heavy particles temperature on the axis of a 1 MPa xenon arc discharge.

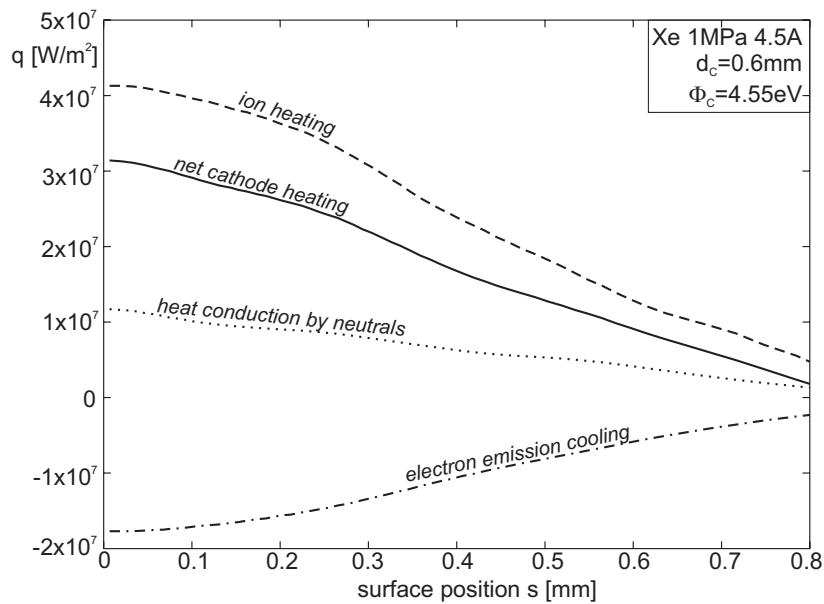


Figure 5.8: Heat fluxes to the cathode surface for a 1 MPa xenon arc discharge ($I=4.5\text{A}$).

5.2.2 Properties of the cathode hot spot

The model does not use any prescribed boundary conditions at the cathode or anode surface. The net heat flux distribution at the electrode surfaces is emerging self consistently from the interaction of electron emission, plasma sheaths and constriction near the surface. As shown in figure 5.8, the energy balance within the cathode hot spot is determined by ion heating, electron emission cooling and heating due to the neutral gas temperature gradient.

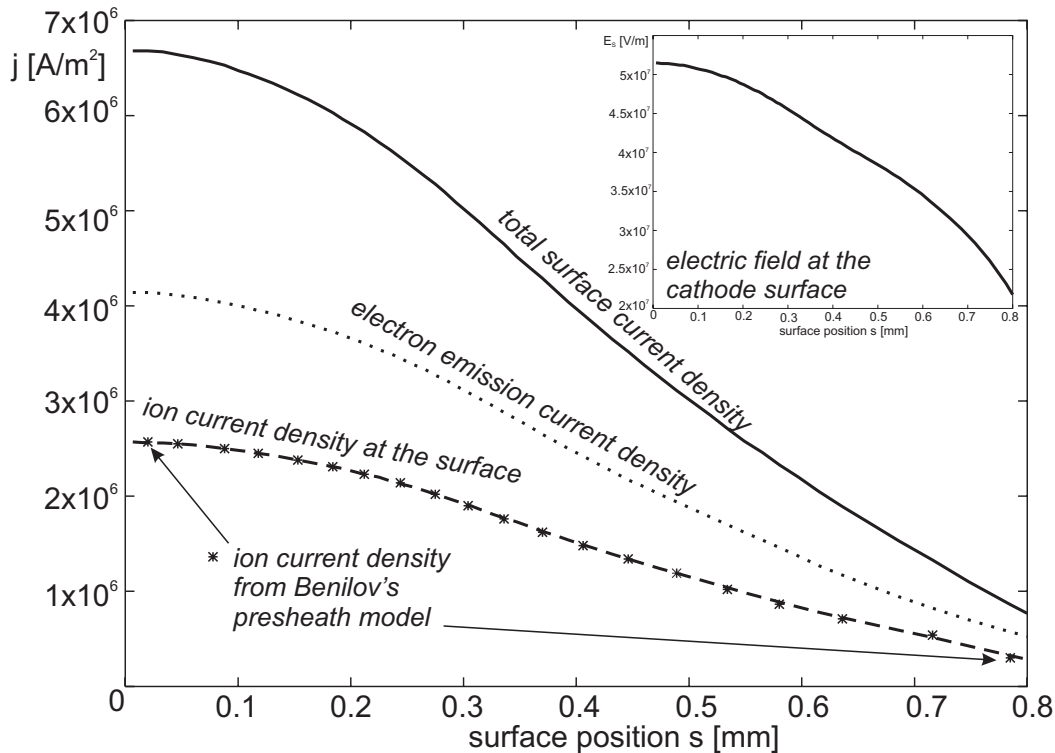


Figure 5.9: Current densities at the cathode surface for a 1 MPa xenon arc discharge ($I=4.5A$).

The electrical current density at the cathode surface (figure 5.9) is given by the electron emission current density and the ion current coming from the presheath.

While the overall discharge model used here does not require a detailed model of the cathodic ionization layer (presheath), it is possible to compare the resulting ion current coming from the presheath with the results from the one dimensional model developed by Benilov and Marotta ([BM95], section 3.3.5). Figure 5.9 shows the excellent agreement of both modelling approaches. As shown in figure 5.10, the major assumptions of the layer model (see section 3.6) agree with the mean free paths in the near cathode plasma.

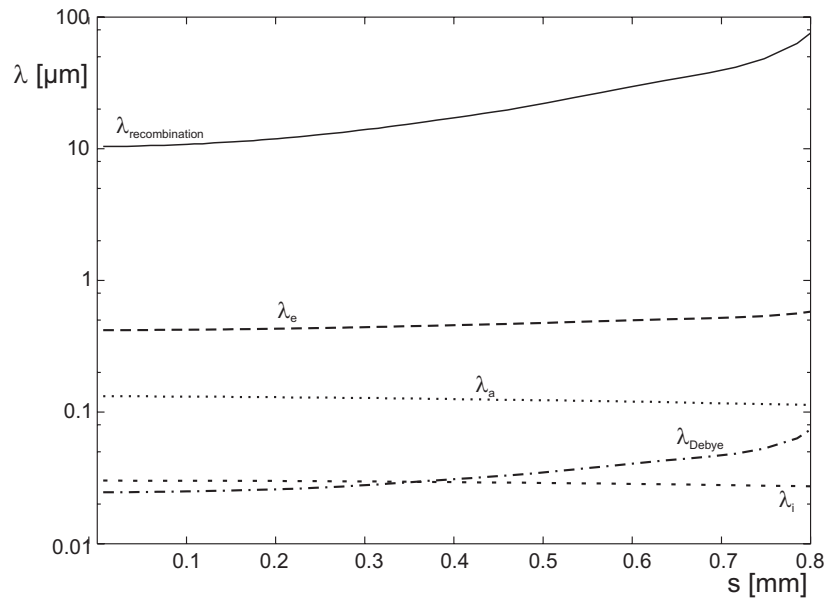


Figure 5.10: Debye length λ_d , ion, electron and atom mean free paths and recombination length of the plasma species along the cathode surface coordinate s (Xe, 1MPa, 4.5A).

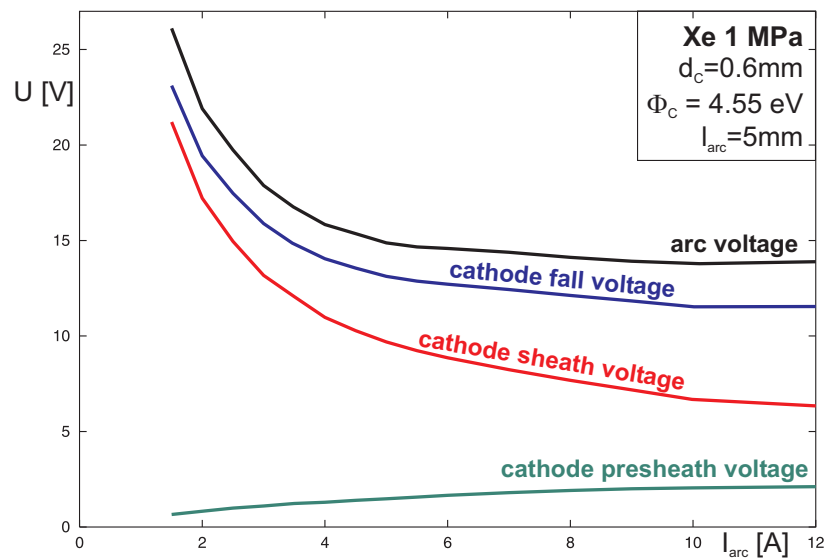


Figure 5.11: Variation of the arc, cathode fall and layer voltages with total current.

5.2.3 Parameter variations

After discussing the spatial distribution of the basic physical arc properties, the modelling input parameters plasma gas, discharge pressure, total current, cathode diameter and electron work function will be varied.

5.2.3.1 Arc voltage, cathode fall and layer voltages

The first and most important quantity of thermal plasma gas discharges, the voltage current characteristic is shown in figure 5.11. The high burning voltages for very low currents can be identified with the increase of the space charge layer sheath voltage with decreasing current. The self consistent presheath voltage slightly increases with current, while the cathode fall voltage defined by

$$U_{C,PP} = U_{\text{arc}} - U_{r=0,z=l_{\text{arc}}/2} - l_{\text{arc}}/2 \cdot E_{r=0,z=l_{\text{arc}}/2} \quad (5.1)$$

follows the sheath voltage characteristic. The difference of the cathode fall voltage (which can be determined experimentally [LNBM99]) to the sum of sheath and presheath voltage comes from the increasing electric field due to the near cathode plasma constriction.

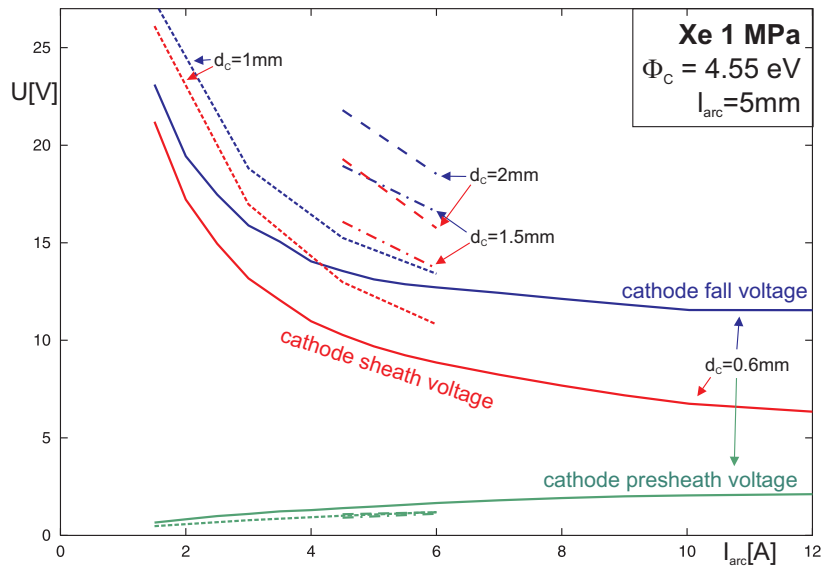


Figure 5.12: Variation of the cathode fall and layer voltages with total current plotted for different values of the cathode diameter d_C .

Larger cathode diameters increase the heat losses of the cathode and thus require higher sheath voltages to increase the energy of the impinging ions heating the cathode surface to thermionic emission temperatures (figure 5.12).

Increasing pressure slightly enhances the layer and cathode fall voltages due to the smaller ionization degree of the plasma (figure 5.13). The larger increase in arc voltage with increasing pressure is caused by the larger electric fields required in the main arc core, because radiative, convective and conductive heat losses increase and electric conductivity decreases. At lower pressure levels, the cathode fall voltage can become larger than the arc voltage, because the anode fall voltage becomes negative.

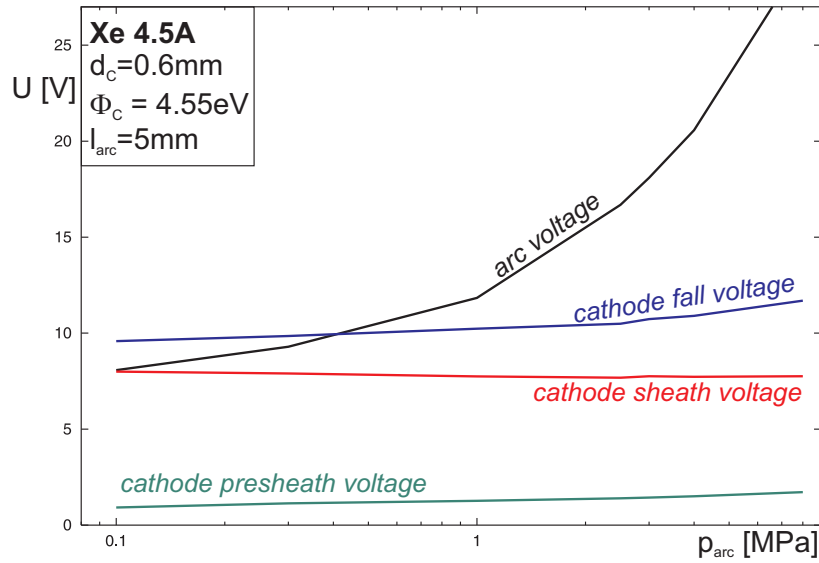


Figure 5.13: Variation of the arc, cathode fall and sheath voltages with discharge pressure.

Varying pressure for different plasma gases (figure 5.14) shows how gases with low ionization energy like mercury require higher cathode fall voltages with increasing pressure, due to the increasing voltage drop in the near cathode plasma. Because above 1 MPa the argon plasma undergoes a transition from partial LTE to LTE in the arc column, the sheath voltage may even decrease with pressure,

One of the main purposes of the space charge layer (sheath) is to accelerate the ions in order to gain energy for heating the cathode to thermionic emission temperatures. With decreasing cathode work function Φ_C , the sheath voltage is thus also decreasing (figure 5.15).

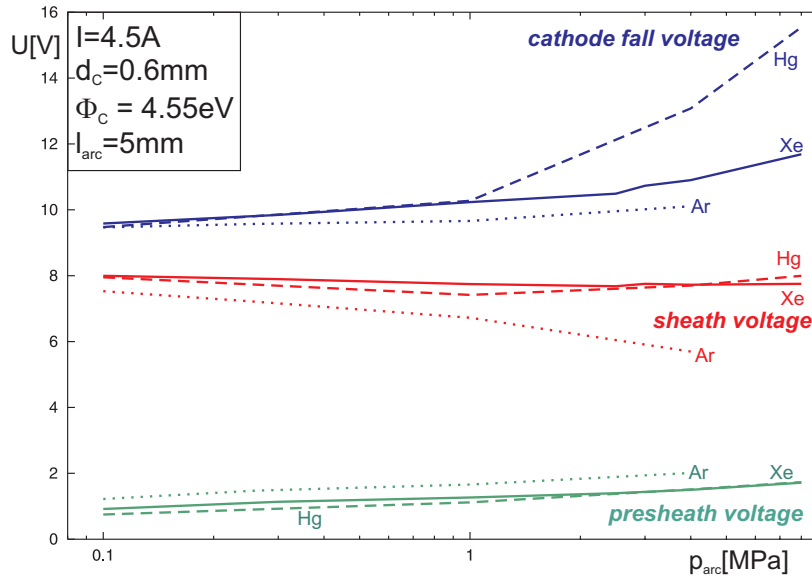


Figure 5.14: Variation of the cathode fall and layer voltages with total discharge pressure for different filling gases.

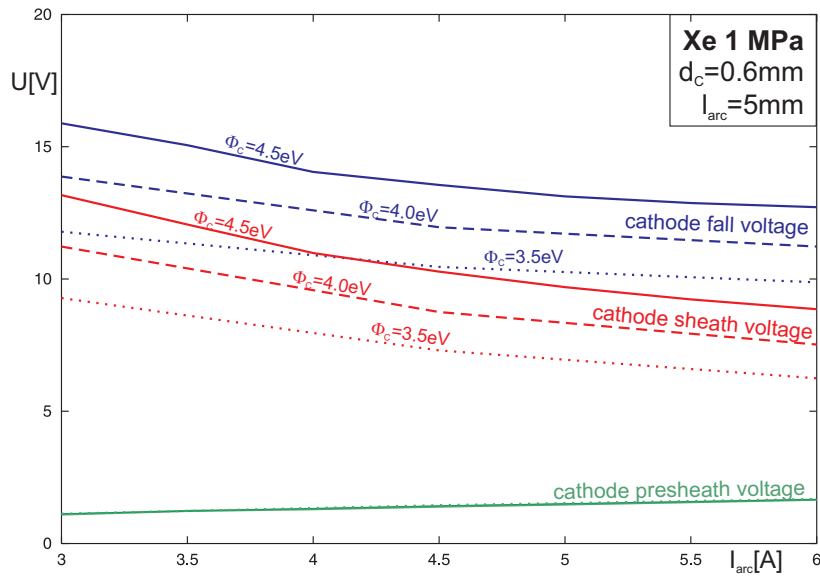


Figure 5.15: Variation of the cathode fall and layer voltages with current for different values of the cathode work function Φ_C .

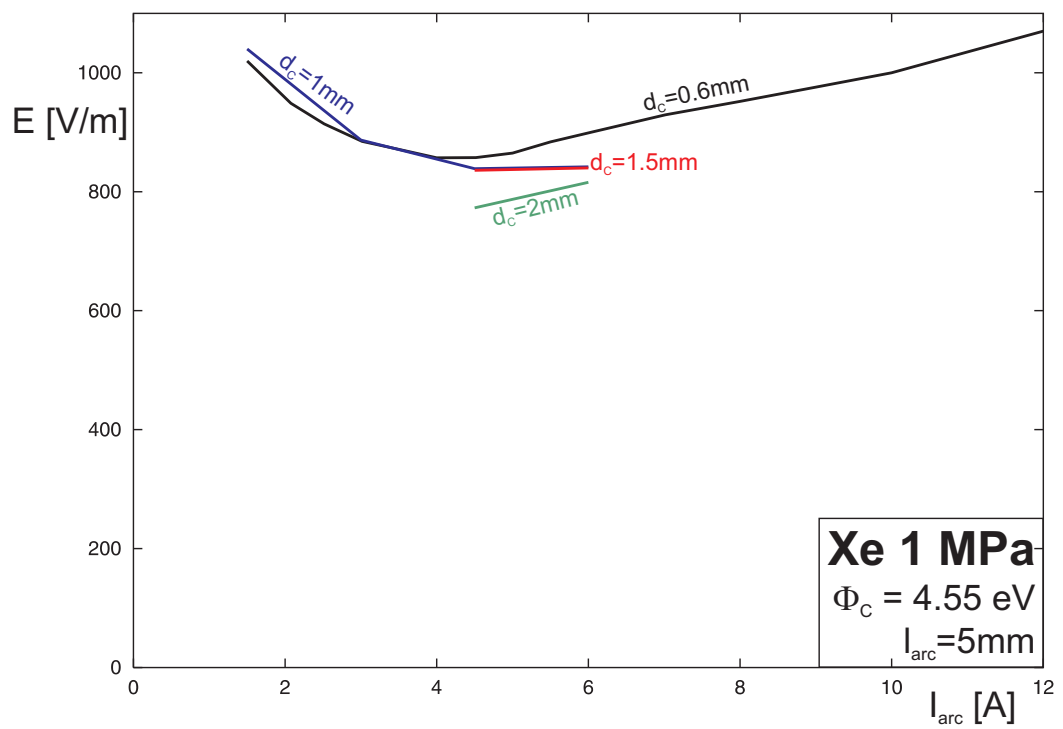


Figure 5.16: Variation of the minimum electric field in the arc column with current for different values of the cathode diameter d_C .

5.2.3.2 Electric field in the arc column

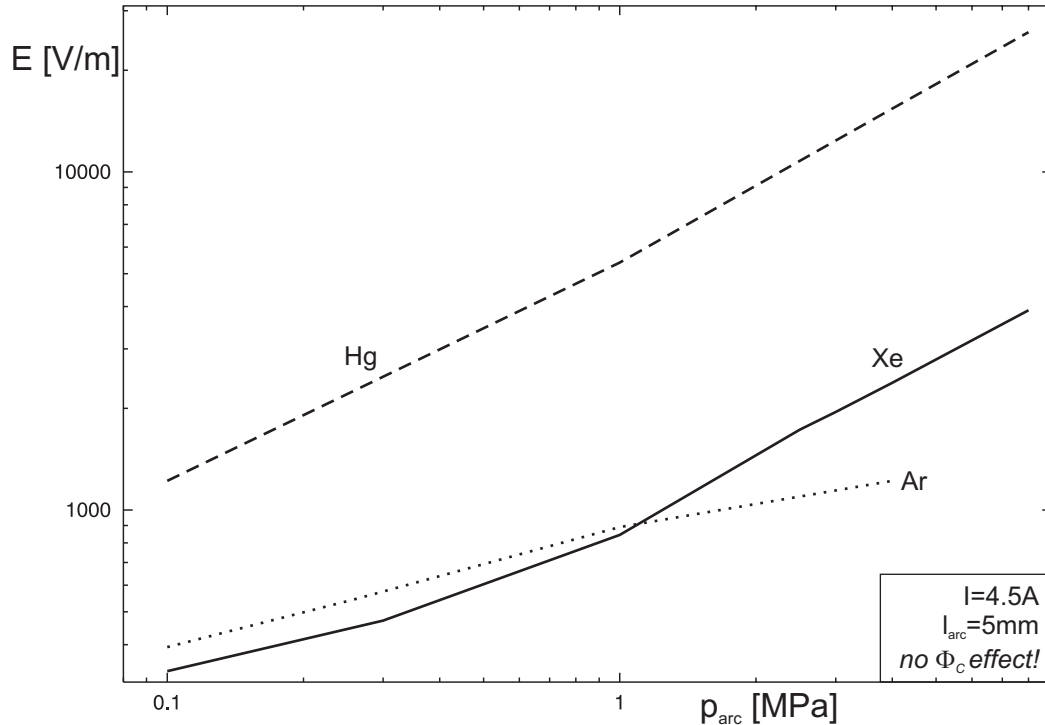


Figure 5.17: Variation of the minimum electric field in the arc column with pressure for different filling gases.

The minimum electric field in the arc column (determined from its axial variation shown in figure 5.5) depends on current and pressure (see also figure 3.4). As shown in figure 5.16, the model is able to reproduce this fundamental arc property. The effect of the cathode properties like diameter d_C is rather small. For most discharge configurations electrode effects on this quantity vanish with increasing arc length.

Higher discharge pressure levels increase the radiative, convective and conductive energy losses. To carry the prescribed arc current, the electric field in the arc column increases with pressure (figure 5.17). Due to the missing Ramsauer minimum and its larger values, the electron-atom cross section causes much higher electric fields in mercury discharges than in xenon or argon.

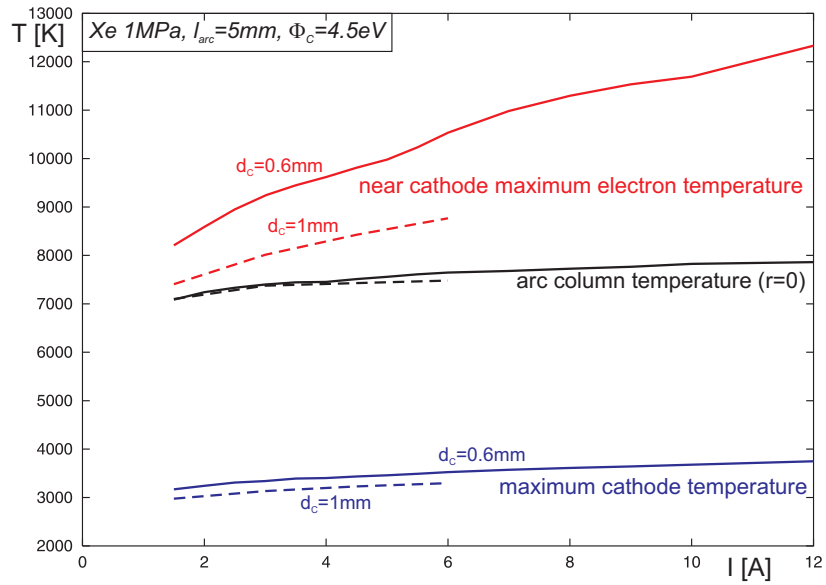


Figure 5.18: Variation of the maximum electron temperature near the cathode, the on-axis electron temperature in the arc center and the cathode hot spot surface temperature with total arc current for different cathode diameters d_C .

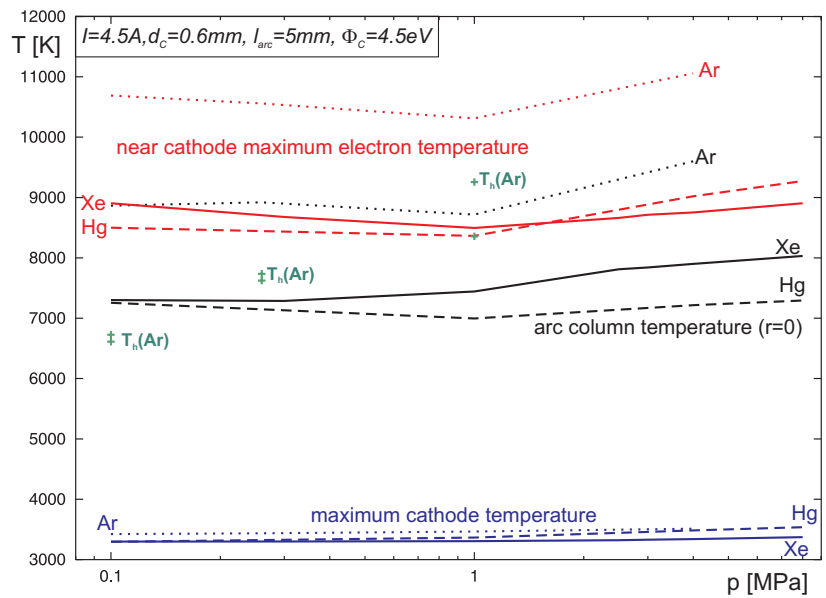


Figure 5.19: Variation of the maximum electron temperature near the cathode, the on axis electron temperature in the arc center and the cathode hot spot surface temperature with discharge pressure for different plasma gases (for the non LTE argon discharges, the heavy particles temperatures in the arc center is also plotted).

5.2.3.3 Plasma and cathode hot spot temperatures

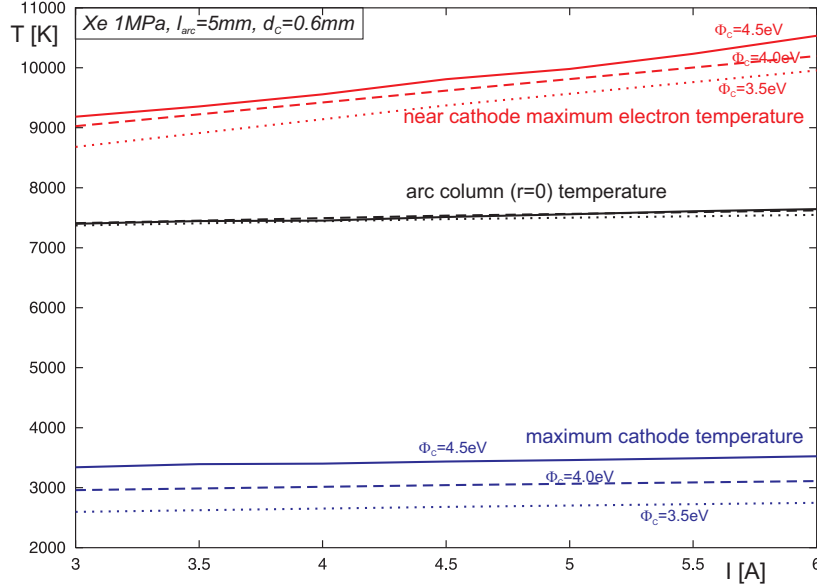


Figure 5.20: Variation of the maximum electron temperature near the cathode, the on axis electron temperature in the arc center and the cathode hot spot surface temperature with current for different values of the cathode work function Φ_C .

In figure 5.18, the variation of the plasma and cathode hot spot temperatures with arc current is shown. The column temperature is slightly increasing due to a small variation of the energy balance in the arc center with increasing current. Its absolute value is mainly determined by the variation of electric conductivity with electron temperature. The near cathode maximum of the axial electron temperature distribution strongly depends on current (increasing current densities increase the joule heating term) and electrode properties like cathode diameter (figure 5.18) and work function (figure 5.20).

Depending on the ionization threshold temperature of the plasma gas, the plasma temperatures are larger for inert gases (figure 5.19). Additionally, for low current levels and pressures below 1 MPa, the argon arc is not in local thermal equilibrium (LTE). As shown in figure 5.19, with decreasing pressures an increasing gap between electron and heavy particles temperature in the argon arc column occurs.

The cathode hot spot surface temperature is not very sensitive to the discharge gas or pressure. It mainly depends on the cathode work function (figure 5.20) and the cathode geometry (figure 5.18). Due to the workfunction effect on the hot spot current density, the maximum electron temperature also increases with the cathode material work function.

5.2.3.4 Cathode hot spot peak current density

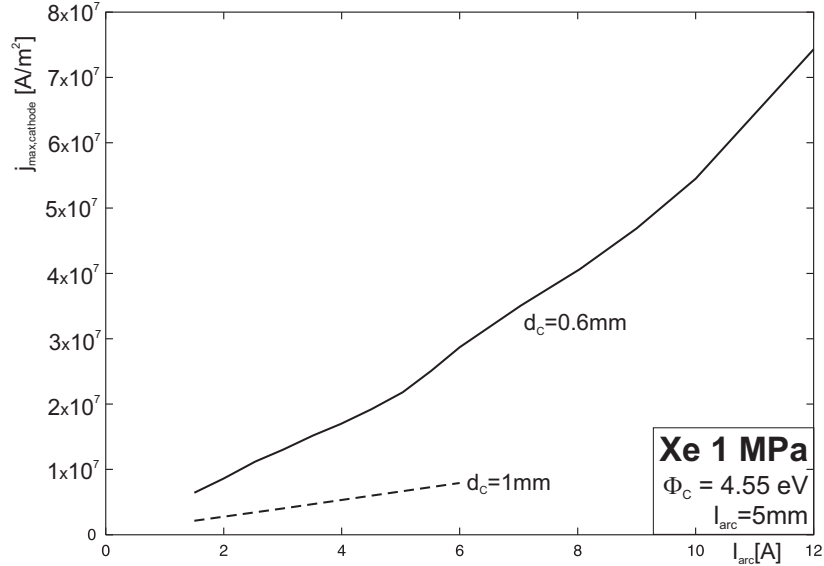


Figure 5.21: Variation of the maximum cathode hot spot electric current density on the axis with arc current for different values of the cathode diameter d_C .

All computations were carried out for a diffuse cathode hot spot. The electric current density on the cathode surface varies with position (figure 5.9) and its maximum value on the axis is plotted in figure 5.21, figure 5.22 and figure 5.23. Small cathode diameters introduce an additional constraint for the current density distribution, because the plasma has to follow the cathode curvature and the current density is strongly determined by the energy balance within the cathode. For small cathode diameters, the peak current density is thus strongly increasing with current, while for larger diameters the current density increase is much smaller (figure 5.21). A further increase in cathode diameter or very low currents will finally result in a change of the cathode attachment mode.

For atmospheric discharge pressures, the effect of the plasma gas and pressure on cathode peak current density is much smaller than for pressure levels above 1 MPa (figure 5.22). In such high pressure discharges, the effect of the higher electric field, required in the arc plasma to carry the prescribed current, gives also rise to increasing peak current densities.

Decreasing the cathode work function allows for lower cathode surface temperatures and a flattening of the current density distribution is energetically preferred. The peak current densities are thus smaller for smaller cathode work functions (figure 5.23).

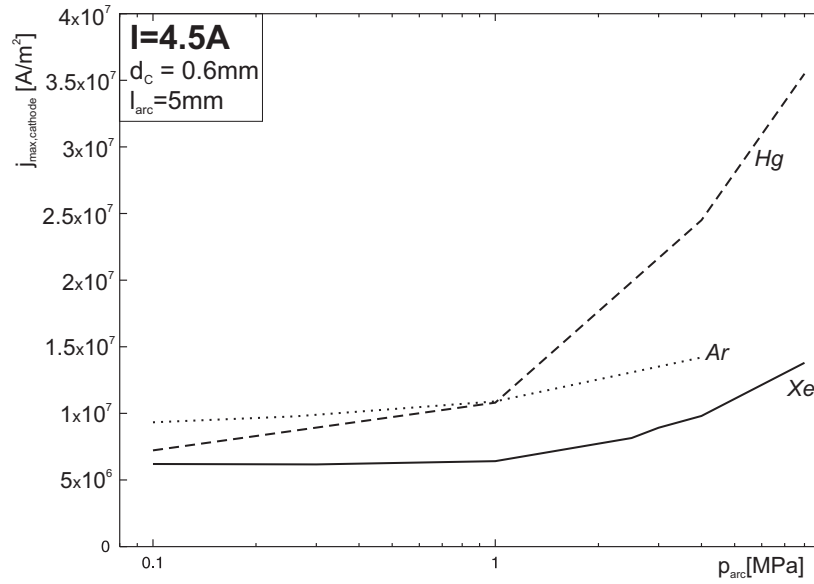


Figure 5.22: Variation of the cathode hot spot current density with discharge pressure for different plasma gases.

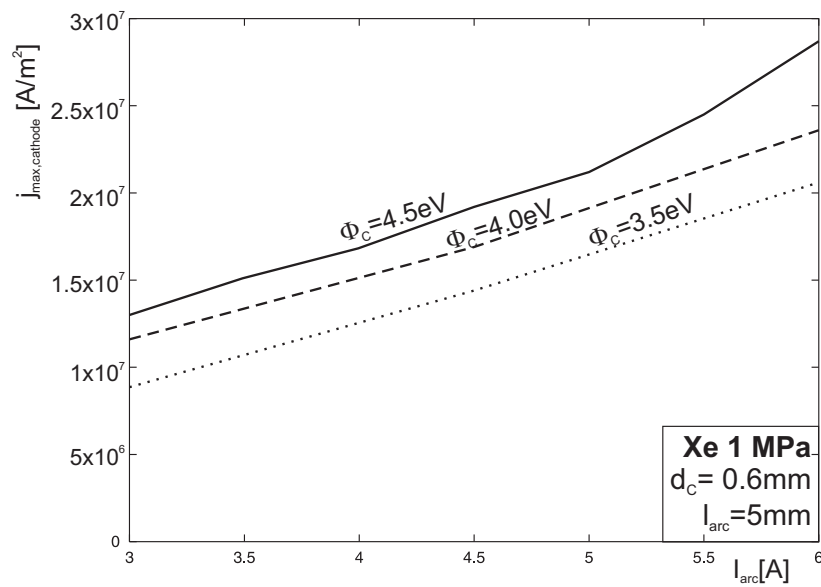


Figure 5.23: Variation of the cathode hot spot current density with arc current for different values of the cathode work function Φ_C .

5.2.3.5 Maximum flow velocity

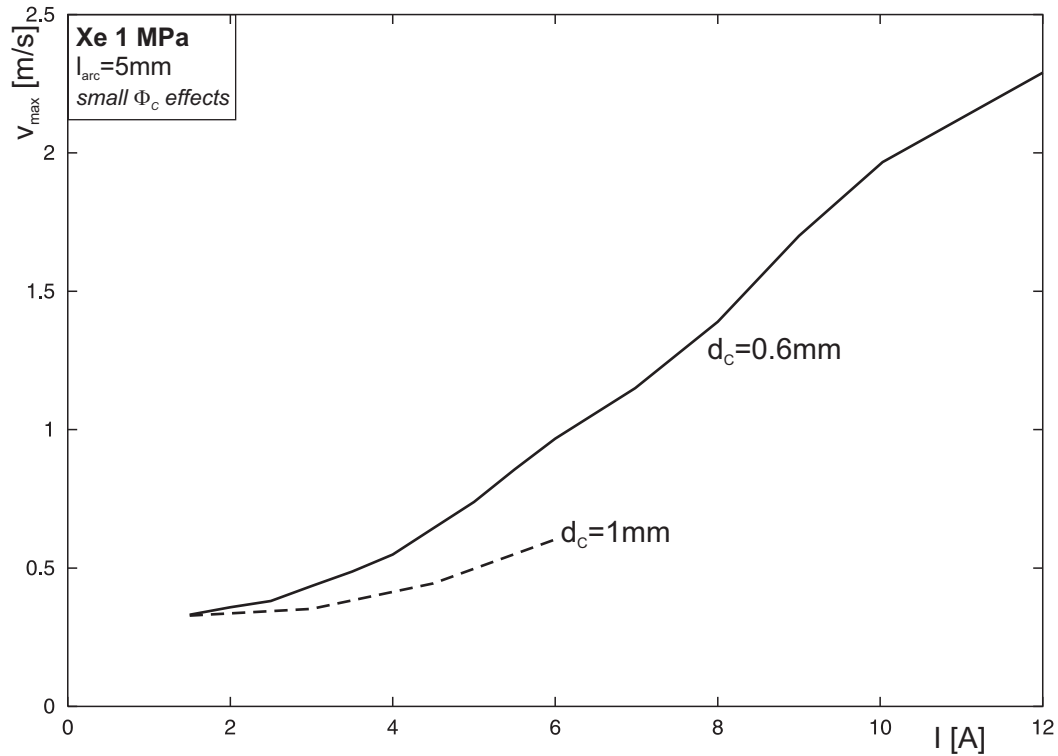


Figure 5.24: Variation of the maximum axial flow velocity with arc current for different values of the cathode diameter d_c .

The maximum axial flow velocity is mainly determined by the magnetic compression in the cathode hot spot (cathode jet). As the peak current density increases with total current, the maximum velocity follows (figure 5.24).

There is also an increase with discharge pressure (figure 5.25), because additional natural convection forces accelerate the flow for this burning position of the arc (cathode at the bottom). The effect of the discharge gas on maximum flow velocity can be explained by the atomic weight of the gas particles.

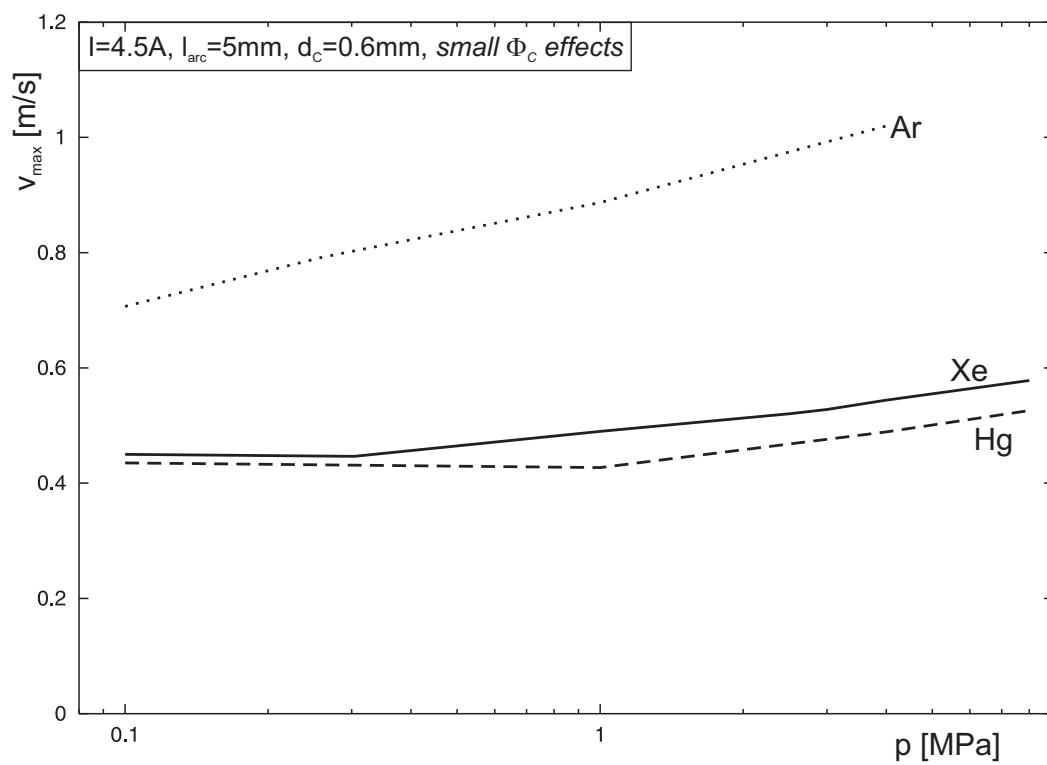


Figure 5.25: Variation of the maximum axial flow velocity with discharge pressure for different plasma gases.

5.2.3.6 Radiative properties of the discharge

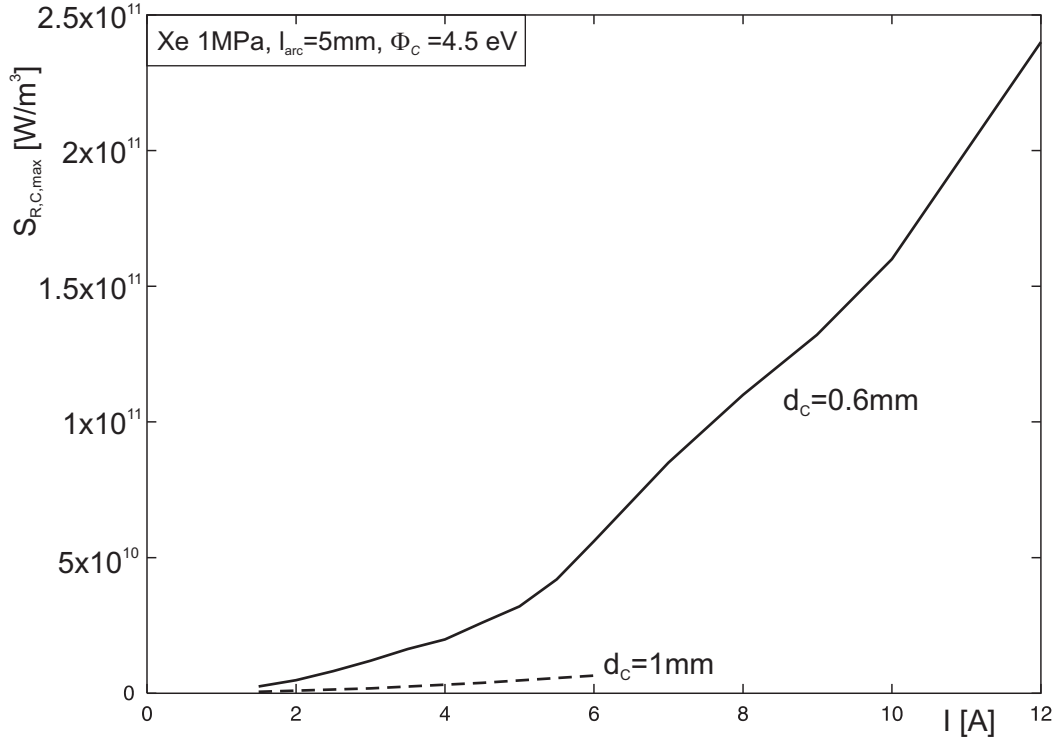


Figure 5.26: Variation of the maximum net radiation emission coefficient with arc current for different values of the cathode diameter d_c .

For lighting applications as well as for the spectroscopic determination of plasma temperatures, the maximum radiation intensity generated within the discharge is crucial. Because detailed radiation transport is not modeled here, only the maximum net radiation emission coefficient can be taken as a measure for this quantity. Due to the rather crude anode sheath model, the maximum net radiation emission coefficient calculated at the axial near cathode electron temperature maximum is provided as a measure of the radiation intensity properties of the discharge.

For small cathode diameters, the increase with arc current is rather strong (figure 5.26). This effect is again caused by the increasing current density (figure 5.21). The order of magnitude of the radiative intensity is first given by the radiative properties of the discharge gas and second by the discharge pressure (figure 5.27). The effect of cathode work function on the peak current density and thus maximum electron temperature can also be found in the increasing net radiation emission coefficient with increasing work function of the cathode material (figure 5.28).

Because high pressure arc discharges are high performance sources of radiation, it is worth to look at the plasma radiation yield, i.e. the total power radiated by the plasma relative to the total power of the discharge (figure 5.29, figure 5.30 and figure 5.31). Due to the sharp increase in the net radiation emission coefficient with electron temperature, the radiation yield follows the dependencies of the maximum electron temperature and thus the peak electric current density in the cathode hot spot. It linearly increases with current (figure 5.29) and strongly

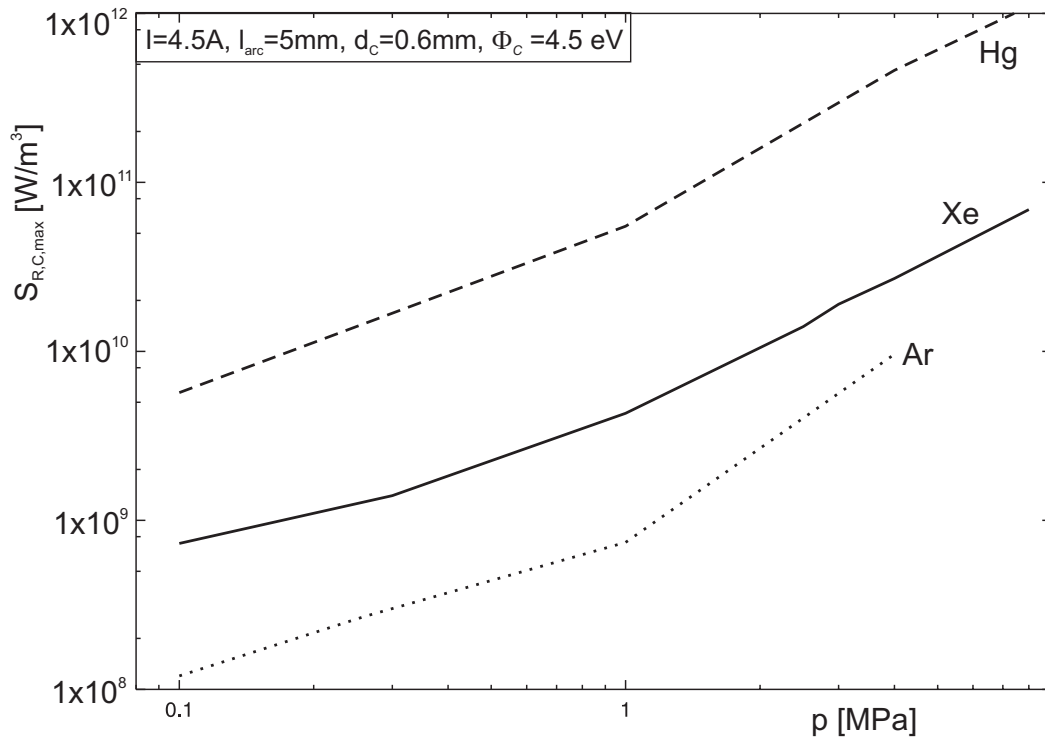


Figure 5.27: Variation of the maximum net radiation emission coefficient with discharge pressure for different plasma gases.

depends on the radiative properties of the filling gas (figure 5.31). The increase of the radiation yield with decreasing work function shown in figure 5.29 can be explained by a change in the spatial distribution of the plasma temperature. A wider temperature distribution can provide a larger area at high electron temperature and thus higher radiation yields.

In reality, the high radiative yields of the mercury discharge at very high pressures (figure 5.31) are limited by radiation transport phenomena not included in the current model. For lamp fillings like mercury and discharge pressures above several atmospheres, a quantitative calculation at least requires an inclusion of a radiative heat conductivity into the model (see section 5.3.5).

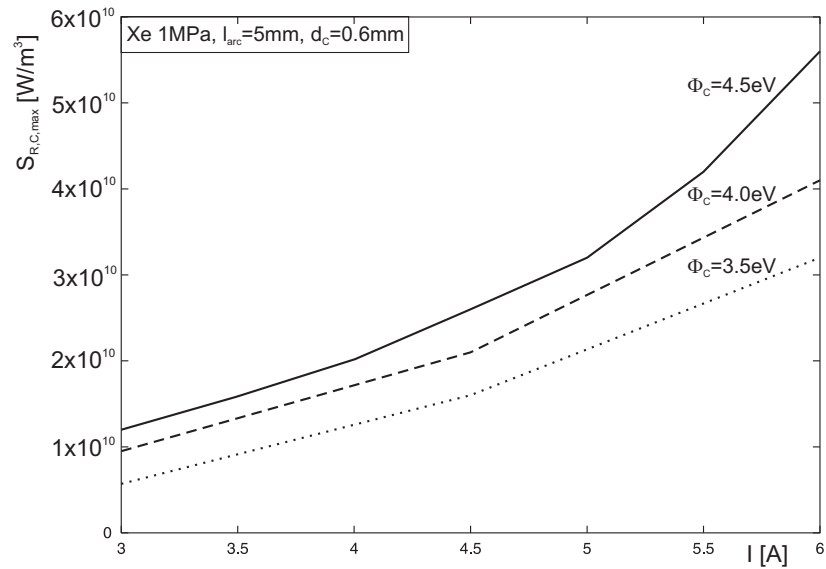


Figure 5.28: Variation of the maximum net radiation emission coefficient with current for different values of the cathode work function Φ_C .

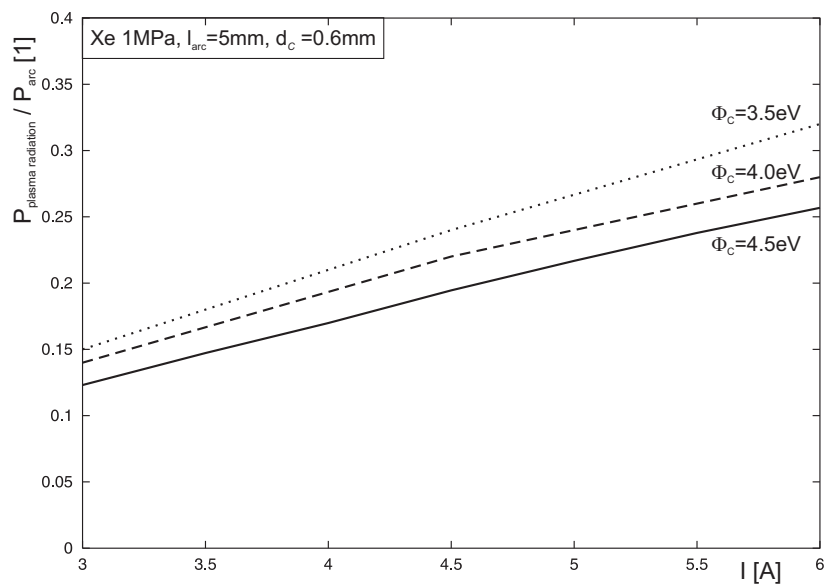


Figure 5.29: Variation of the radiation yield with current for different values of the cathode work function Φ_C .

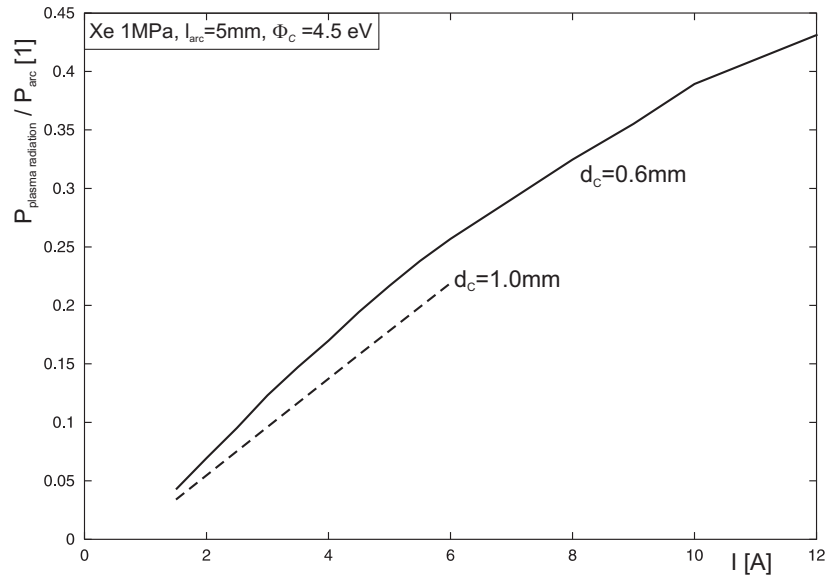


Figure 5.30: Variation of the radiation yield with arc current for different values of the cathode diameter d_c .

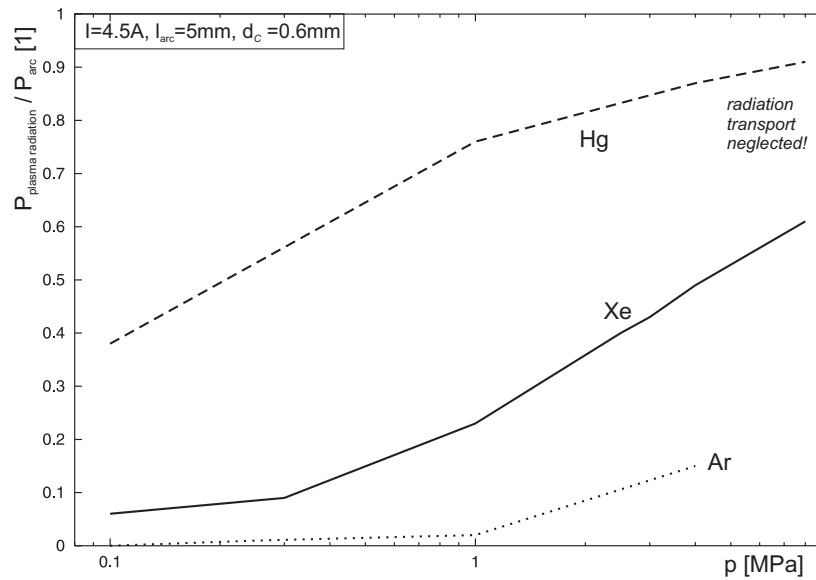


Figure 5.31: Variation of the radiation yield with discharge pressure for different plasma gases.

5.2.4 Physical sensitivity analysis

Dimensionless numbers describing the fundamental hydrodynamic characteristics of arc discharges:		
$Ma = \frac{\text{inertia force}}{\text{elastic force}} = \frac{v}{v_{\text{sound}}}$		$\ll 0.3$
$Re = \frac{\text{inertia force}}{\text{viscous force}} = \frac{\rho v l}{\mu}$		1..300
$Gr = \frac{(\text{inertia force})(\text{buoyant force})}{(\text{viscous force})^2} = \frac{\rho^2 g l^3 \beta \Delta T}{\mu^2}$		63..(>10000)
$Ga = \frac{\text{gravity force}}{\text{viscous force}} = \frac{g \rho^2 l^3}{\mu^2}$		500..50000
$Fr = \frac{\text{inertia force}}{\text{gravity force}} = \frac{v^2}{g l}$		0.5..10
$J_w = \frac{\text{magnetic force}}{\text{gravity force}} = \frac{j B}{\rho g}$		>1000
$Pr = \frac{\text{momentum diffusivity}}{\text{thermal diffusivity}} = \frac{c_p \mu}{\kappa}$		0.5 .. 5
$Pe = \frac{\text{heat convection}}{\text{heat conduction}} = \frac{\rho c_p v l}{\kappa}$		1 .. 300
fundamental dependency: discharge pressure:		
0.1 .. 8 MPa		

maximum values, minimum mostly 0!

Figure 5.32: Hydrodynamic parameters of thermal plasma gas discharges.

From figure 5.32 the importance of flow phenomena in general and of natural convection and magnetic compression in detail can be estimated. The Reynolds number is above unity but well below the critical values for turbulence. The plasma will show fully developed laminar flow. The Peclet number is always above unity, therefore one should not calculate thermal plasma gas discharges without taking fluid flow effects into account.

Nevertheless, the arc is mainly an electrical phenomenon, and the influence of the different physical effects has to be computed for every specific discharge situation. The validation of most physical approximations can not be done in advance.

In table 5.1, the physical sensitivity matrix of the model discharge configuration is provided. The values of the second row are absolute quantities in SI-units, while all other values are given as the relative deviation to the second row.

U denotes the total arc voltage, $U_{C,PP}$ the cathode fall voltage (equation 5.1), E_{\min} the minimum electric field in the arc column, $T_{C,\max}$ the maximum cathode temperature, $T_{e,\text{col}}$ the plasma temperature in the center of the arc column, $T_{e,C,\max}$ the maximum plasma temperature in front of the cathode, $S_{R,C}$ the maximum net radiation emission coefficient (see section 4.9), S_R the amount of radiated power compared to the total arc power, $j_{C,\max}$ the maximum current density at the cathode surface and v_{\max} the maximum flow velocity in the discharge.

The table is based on calculations for the model arc configuration (Xe 1MPa, 4.5A, $d_C = 4.5\text{mm}$, $\Phi_C = 4.55\text{eV}$) on a non equidistant grid of 48x96 finite volumes. It has to be interpreted as

variant:	U	$\bar{U}_{C,PP}$	E_{\min}	$T_{C,max}$	$T_{e,col}$	$T_{e,C,max}$	$S_{R,C}$	$S_R\%$	$j_{C,max}$	v_{max}
1. all 3 A	13.6%	12%	3.7%	-2.8%	-1.4%	-5.2%	-54.1%	-37%	-34%	-28%
2. all 4.5A	11.4	9.9	819	3301	7402	8422	$4 \cdot 10^9$	24%	$6 \cdot 10^6$	0.5
3. all 6 A	-2.4%	-3.2%	4.2%	2.1%	1.6%	5.1%	103%	28%	44%	45%
4. fine grid	1.5%	0.9%	2.8%	0.6%	0.5%	0.5%	11%	-0.9%	17%	3.4%
5. no flow	-7.9%	-6.6%	-6.2%	-0.6%	-2.4%	-3.0%	-35%	6.5%	-14%	-
6. top down	-2.6%	-9.1%	1.7%	-0.5%	1.0%	-3.0%	-35%	16%	-12%	12%
7. no gravity	-3.7%	-0.9%	-11%	-0.1%	-2.8%	-1.2%	-14%	5.6%	-1.2%	-23%
8. no $\vec{j} \times \vec{B}$	1.0%	0.4%	3.3%	0.1%	-0.1%	0.0%	2.7%	-1.6%	2.2%	-52%
9. " & td	-6.2%	-12%	5.1%	-1%	0.8%	-4.2%	-46%	16%	-21%	-54%
10. no $\vec{j} \nabla T_e$	3.6%	3.8%	1.2%	0.2%	0.1%	0.8%	14%	-1.7%	7.2%	-0.2%
11. $U_S = \text{const.}$	4.3%	0.3%	2.7%	3.7%	1.1%	9.5%	251%	-3.1%	159%	20%

Table 5.1: Sensitivity of basic arc parameters regarding the inclusion of different physical processes, current and arc burning position (see text).

follows: The first and third rows show the variation of the basic arc parameters with total discharge current and the fourth row shows the relative deviation for calculations with a very fine numerical grid (144x288 finite volumes or more). In the following rows, the relative deviations obtained by switching off the different physical effects included into the discharge model are presented. Deviations smaller than the numerical error provided in row 4 are questionable and should be interpreted very carefully. The basic results of this physical sensitivity analysis are as follows:

- Very fine numerical grids are required for calculating the maximum radiation intensity and the maximum cathodic current density with an accuracy better than 10%.
- Neglecting fluid flow phenomena (*no flow*, row 5) delivers most arc properties with an accuracy of 5-10%. The consequences of neglecting flow phenomena are as follows:
 - The maximum radiation intensity of the arc can not be determined quantitatively.
 - The cathode hot spot formation can be modelled with an accuracy of about 15%.
 - Quantities directly related to flow phenomena like the heat load distribution to the inner surfaces of the discharge tube can not be computed.
 - Taking the variation of the arc properties with current into account, a 5-10% accuracy is often identical to a total discharge current varying by a factor of two.
- Reversing the burning position of the model lamp (*top down*, row 6, anode now at the bottom) changes radiative properties as well as cathodic spot quantities.
- Neglecting (gravity induced) natural convection (*no gravity*, row 7) drastically changes the flow pattern and thus the column electric field and the radiative properties.
- Neglecting magnetic compression forces (*no $\vec{j} \times \vec{B}$* , row 8) gives much smaller flow velocities. The effect is more drastic for the reversed burning position (*no $\vec{j} \times \vec{B}$ and top down*, row 9) and will also result in unrealistic flow patterns for horizontal burning positions.
- Neglecting electron enthalpy flow (*no $\vec{j} \nabla T_e$* , row 10) can lead to deviations in the same order of magnitude as the total cancelation of flow phenomena.

- A spatially constant cathode space charge layer voltage ($U_S = \text{const.}$, row 11) strongly influences radiative and cathode hot spot properties.

As a conclusion, neglecting one of the different driving forces of the flow ($\vec{j} \times \vec{B}$ or gravity) can have larger effects on the results than neglectation of flow phenomena at all. A quantitative computation of the radiative properties of high-pressure lamps strongly demands for the full inclusion of flow phenomena. For mercury, at pressures above 2 MPa, the radiation transport has also to be described in detail. Radial symmetric calculations are not possible for arcs burning horizontally. With increasing pressure, even discharges with cylindrical symmetry may develop three dimensional or turbulent flow patterns.

5.3 Model validation

As a result of the basic parameter study and the physical sensitivity analysis presented above, a number of fundamental problems regarding the experimental validation of arc models must be taken into account:

- Most physical and technological properties of the discharge are the result of self organization within the overall arc electrode system: Without violating the *ab initio modelling* principle, the discharge can not be divided into separately computeable parts (see section 1.3).¹
- The experimental and modelled discharge configuration have to agree in almost every detail, especially in the electrode geometry.
- Not all measureable quantities are usefull for a validation of the numerical and physical details of the model, e.g. the experimental accuracy of spectroscopic plasma temperature measurements is about 5-10%, but the plasma temperature does only slightly change with current or pressure [WDWS97a].
- Only radial symmetric arc discharges in a stationary state in or not too far away from LTE can be described *ab initio* by actually available models.
- Physical quantities crucial for the overall discharge behaviour (e.g. peak electrode current densities) are often not accessible by experiment.
- A number of fundamental properties like cross sections or electrode work function are not exactly known. As a result, the effect of a material property accuracy may hide the failure of a specific model or may give quantitative wrong results for a physically correct model.

In the following sections, a number of discharge configurations with available experimental data is presented and the modelling results are compared with experiment in order to obtain an overall model validation statement and a testimony for the individual physical descriptions of the arc regions.

¹With decreasing total current the discharge can become dominated by the requirement to heat the cathode to thermionic emission temperatures – the cathode attachment thus can be calculated by a sheath-cathode model [BB00].

5.3.1 Low current atmospheric argon arc

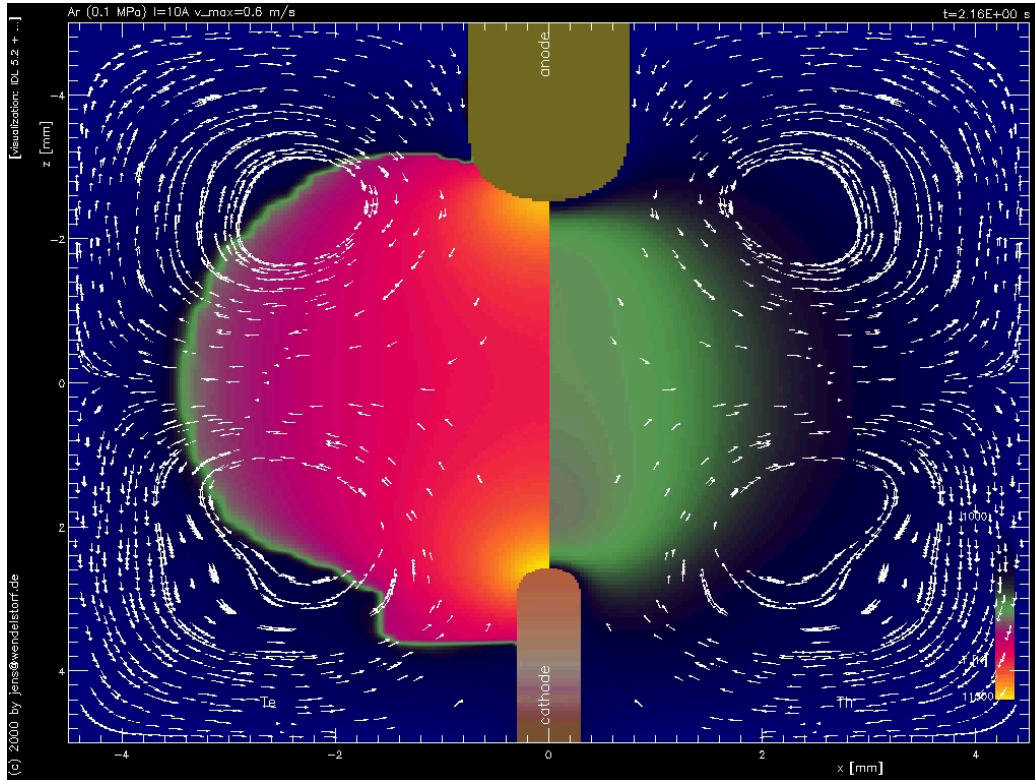


Figure 5.33: Plasma temperatures (left side: T_e , right side: T_h) and flow field of a 10A, 0.1 MPa argon arc discharge (the electron temperature *step* in the lower left corner is a numerical artefact not influencing any measureable discharge parameter, it will vanish after sufficiently large computation times).

The experimental determination of the cathode fall voltage and plasma temperature map is difficult for high pressure discharges. It is more affordable and simple to perform measurements for argon discharges at or around the atmospheric pressure level. Especially at total currents below 50A, the arcs show very few radiation from the arc column and thus the electrode temperatures may be determined by thermography. It is also possible to determine the electron- and heavy particle temperatures as well as the electron density by spectroscopical methods. As shown in figure 5.33, the computed temperature distribution of such low power atmospheric argon arcs is far away from LTE. The electron temperature level lies about 50% above the heavy particle temperature. These results demonstrate the ability of the model to describe non-LTE discharges. At current levels above 10A, there is excellent agreement between the measured arc temperatures and the modelling results (figure 5.34). Thus the model has proven its ability to calculate discharge situations not in LTE.

Nevertheless, a further decrease of the overall discharge current gives rise to another non LTE effect currently not implemented into the model: The deviation from Ohm's law (see section 3.5.3). At a current of 5A or less, the measured electrical field in the arc column is twice the electric field calculated by Ohm's law. As a result, there is a quantitative disagreement of the calculated temperatures (figure 5.35) and electron densities (figure 5.36).

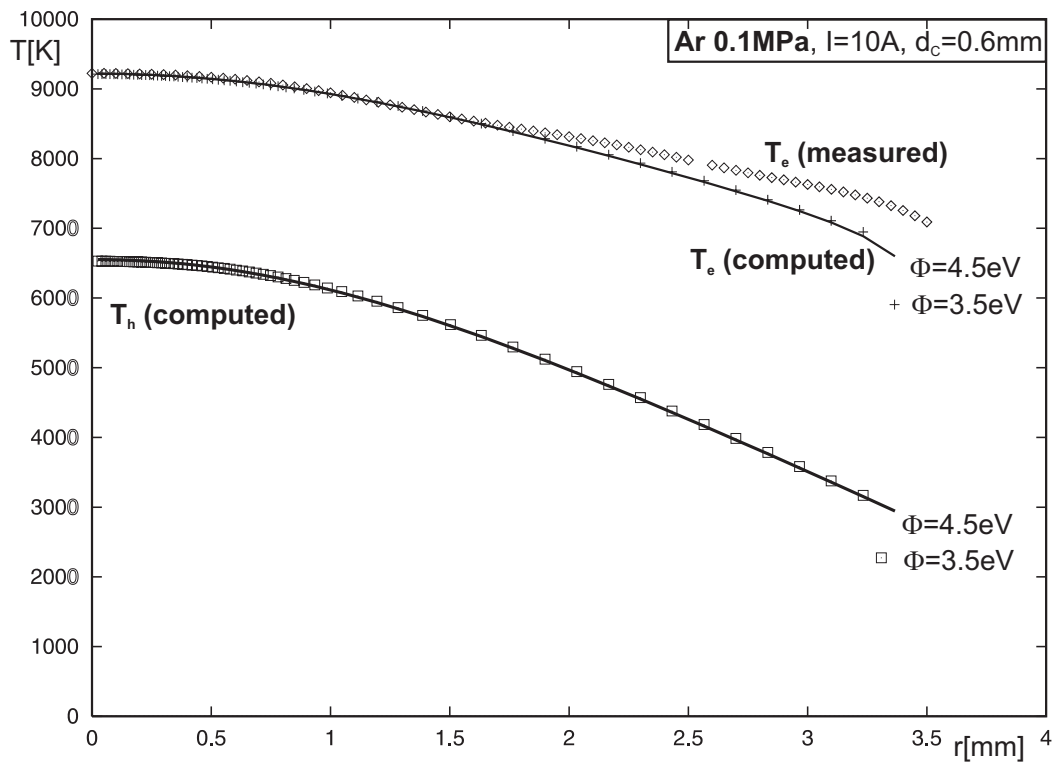


Figure 5.34: Radial variation of the electron and heavy particles temperatures 2mm below the cathode tip (the measurement values are taken from [KSGK99, KSM⁺00]).

Because the main purpose of the discharge is to heat the cathode surface to thermionic emission temperatures, the cathode fall voltage is dominated by the sheath voltage for such discharge configurations. Such a little impact of the electric field in the arc column on the cathode fall voltage results in an excellent agreement with the measurements (figure 5.37). Nevertheless, the model is not able to reproduce the overall burning voltage for discharges so far away from LTE. The computed and measured anode fall voltages do not vary with arc current, but their absolute values differ due to the very simple anode layer model and the large deviations from Ohm's law near the anode.

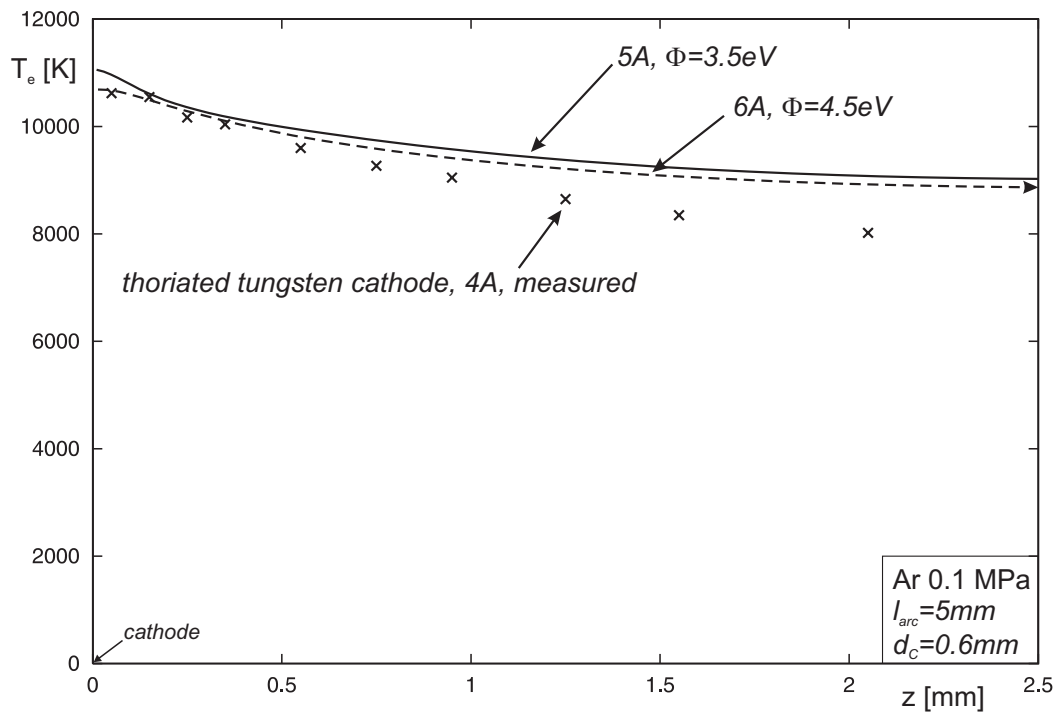


Figure 5.35: Axial variation of the electron temperature for a very low current atmospheric argon arc (the measurement values are taken from [KSGK99, KSM⁺00]).

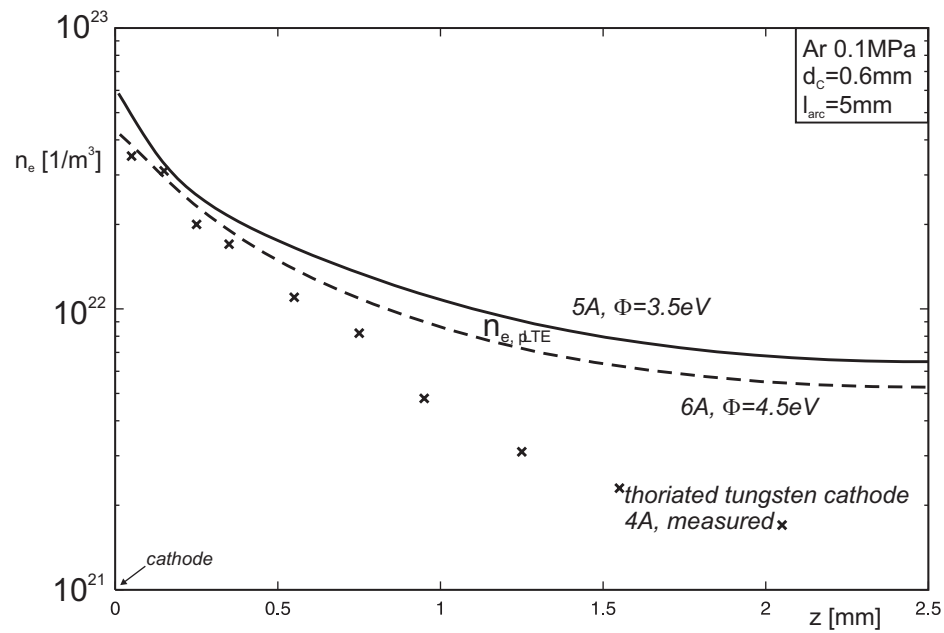


Figure 5.36: Axial variation of the electron density for a very low current atmospheric argon arc (the measurement values are taken from [KSGK99, KSM⁺00]).

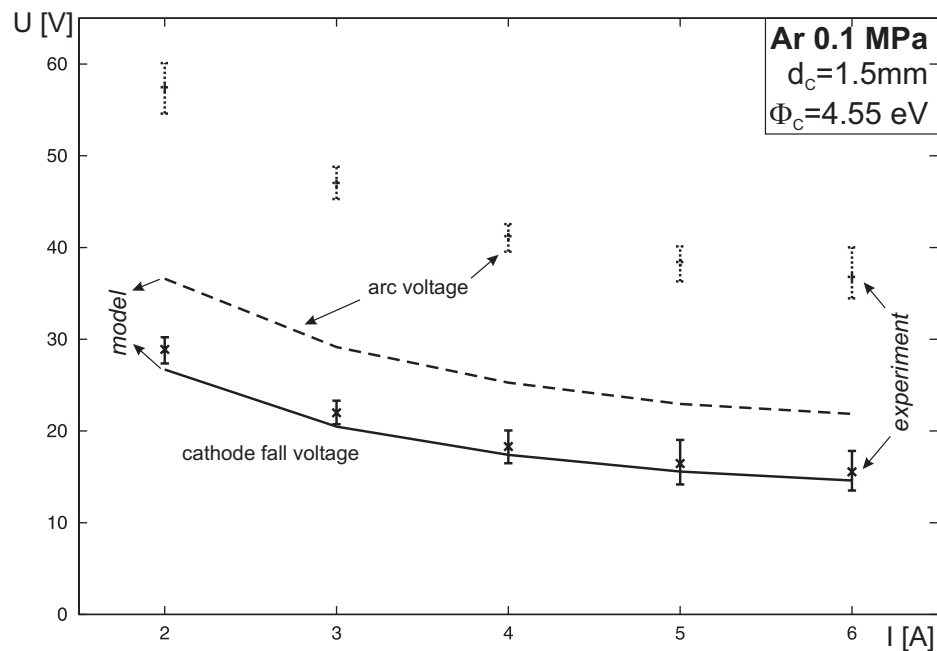


Figure 5.37: Comparison of the calculated variation of the arc and cathode fall voltage with experimental values [LNBM99] ($l_{\text{arc}} = 20\text{mm}$, $l_{\text{a,c}} = 14\text{mm}$).

5.3.2 Low current high pressure xenon model lamp

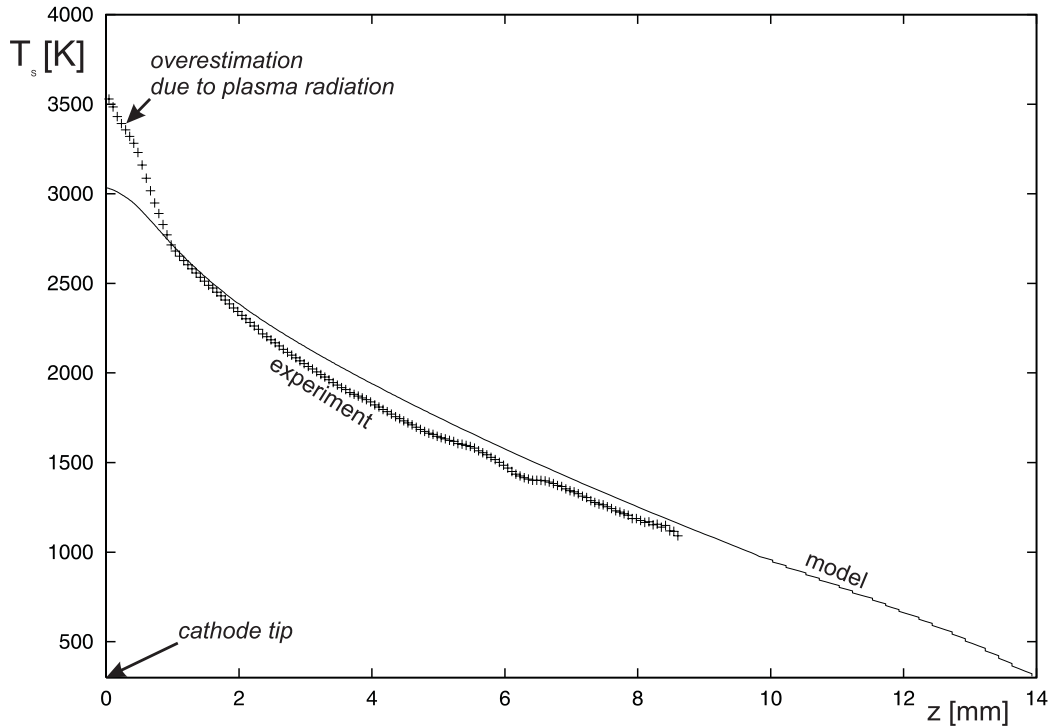


Figure 5.38: Comparison of the calculated and measured cathode surface temperature distribution for a 1 MPa, 2A argon discharge.

Some initial experimental data for 1 MPa xenon discharges at 1-6A are available. This section will provide a comparison with this data and a prediction of the values to be measured in the future.

The major problem of this discharge configuration is the instable arc observed experimentally and predicted by the failure of stationary calculations including fluid flow. All modelling results are therefore coming from computations without any convection effects.

The discharge geometry is that described in figure 5.1, with $l_C = l_A = 14\text{mm}$, $r_C = 0.3\text{mm}$, $r_A = 0.75\text{mm}$ and $l_{\text{arc}} = 20\text{mm}$. The temperature boundary condition for the electrodes at $z = 0$ and $z = z_{\text{max}}$ is 300K.

$I[\text{A}]$	$U[\text{V}]$	$U_C[\text{V}]$	$U_S[\text{V}]$	$U_{\text{PS}}[\text{V}]$	$E[\text{V/m}]$	$j_C[\text{A/m}^2]$	$T_C[\text{K}]$	$P_{C,\infty} [\text{W}]$
6.0	18.6	8.7	5.8	1.3	621	$7.04 \cdot 10^6$	3356	5.7
4.5	18.6	8.9	6.2	1.2	612	$5.03 \cdot 10^6$	3293	5.8
3.0	18.9	9.1	6.9	1.0	613	$3.14 \cdot 10^6$	3205	5.8
1.5	20.9	9.8	8.3	0.7	666	$1.40 \cdot 10^6$	3066	5.7

Table 5.2: Basic discharge parameters calculated for a long arc xenon model lamp (1 MPa).

The calculated discharge parameters shown in table 5.2 are provided to give an approximate prediction of the values to be measured in the near future by Prof. Mentel's group at Bochum

University [LNB99]. Because of the neglect of fluid flow (as a result of the arc instability caused by the large arc length and tube diameter), and the uncertainty in the cathode work function², the accuracy is only about 3V for the cathode fall voltage and about 100K for the cathode hot spot temperature. An additional error for the overall arc voltage may result from the simple anode layer model.

The comparison with initial experimental data for the cathode surface temperature distribution shows sufficient agreement (figure 5.38) – nevertheless the uncertainty in the cathode work function has to be taken into account.

This discharge configuration was defined for comparison of modelling results with experimental data. The calculated arc parameters show reasonable agreement with the first measurement values available. For a quantitative model validation, the discharge configuration has to be changed. Additional efforts are required to eliminate the principal errors induced by inaccurate input data like cross sections and work functions. As a conclusion, the quantitative validation of this or similar discharge models can be done only with respect to a specific quantity to be computed. Additionally, the validation has to be performed for a wide range of discharge pressures and currents.

²The work function of pure tungsten is estimated to be 4.35...4.65eV.

5.3.3 High pressure xenon arcs after Bauer and Schulz

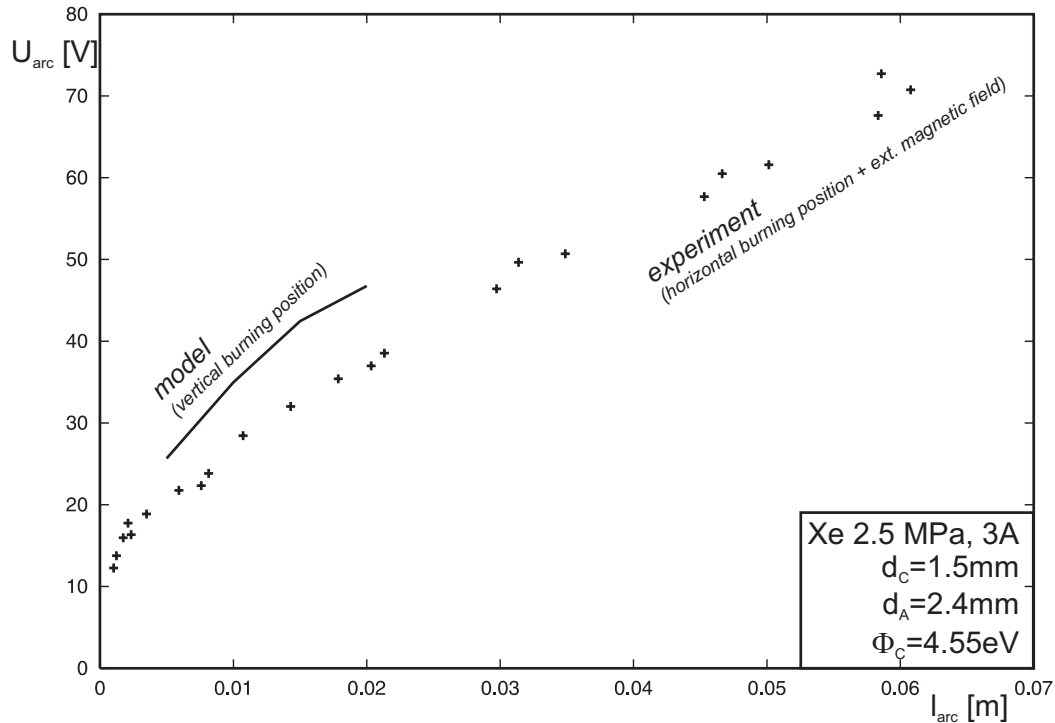


Figure 5.39: Comparison of the calculated variation of the arc voltage with arc length with the experimental values from Bauer and Schulz [BS54].

In 1954, Bauer and Schulz made detailed measurements of arc voltage, cathode fall and electric fields for horizontally burning high pressure xenon arcs [BS54]. This section is an attempt to calculate a similar discharge configuration, and to compare the results with the data from Bauer and Schulz.

As shown in figure 5.39, the experimental arc voltages are slightly below the computed ones. Before treating this fact as a problem of the model, one should take into account the external magnetic field and horizontal burning position Bauer and Schulz used for their experiments. The modelling results were obtained for the vertically burning arc configuration with the cathode at the bottom.

The calculated cathode fall is 23.6V for a discharge pressure of 2.5 MPa, while Bauer and Schulz measured 14V for 3.5MPa and 26V for 1.5MPa. The comparison gives evidence to the need for an exact reproduction of the experimental configuration by the model or vice versa. Additionally, the calculation of the cathode fall from the modelling results for only one arc length (equation 5.1) is justified for long wall stabilized arcs only.

Because of the large computing times needed, it was not possible to get modelling results for all discharge configurations used by Bauer and Schulz.

5.3.4 The high pressure xenon short arc lamp

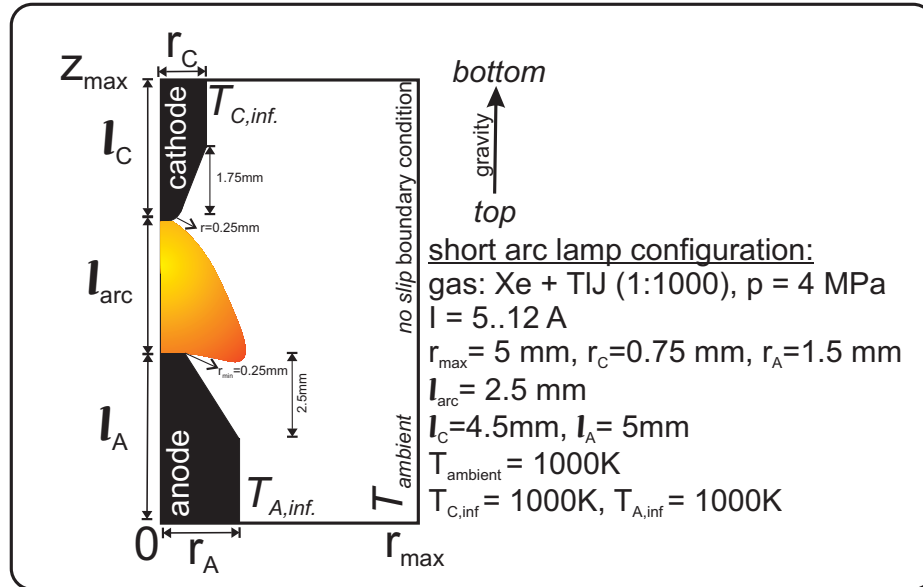


Figure 5.40: Computed configuration of the high pressure short arc lamp.

One of the direct application areas of the model are high pressure short arc lamps. The DC arc is burning in mercury and xenon at pressure levels between 5 and 80 atmospheres (0.5 to 8 MPa). The cathode is tipped, and the anode is relatively large in order to conduct and radiate the heat coming from the arc.

Such a configuration was investigated experimentally by Hoppstock [Hop87]. For numerical efficiency, the modeled configuration was simplified and is shown in figure 5.40. The computed temperature map is presented in figure 5.41. Near the cathode, there is a temperature maximum responsible for the high luminosity of such lamps. The computed and measured plasma temperatures on the arc axis agree within the experimental error (figure 5.42).

Using a thalliumiodide doped xenon filling for such a lamp, Hoppstock found a mode transition in the current range between 5 and 10A. The cathode hot spot changes from a diffuse attachment at 10A to a constricted attachment mode below 5A. The transition shows a hysteresis and a 1V change in the arc voltage. The modelling results were obtained for the diffuse arc attachment. At total currents below 9A, the numerical parameters had to be changed to very small computational timesteps, otherwise numerical divergence occurred. Using such safe numerical parameters, solutions for the diffuse cathode attachment mode were obtained. The calculated peak current densities decrease from $6 \cdot 10^7 \text{ A/m}^2$ at 9A to $4 \cdot 10^7 \text{ A/m}^2$ at 5A. The convergence was not absolute and the computation can be continued for a very long time (several weeks). On such a (computational) time scale, there seems to be a tendency towards a spot mode. Because of the large computing times, it was not possible to obtain a converged spot mode solution.

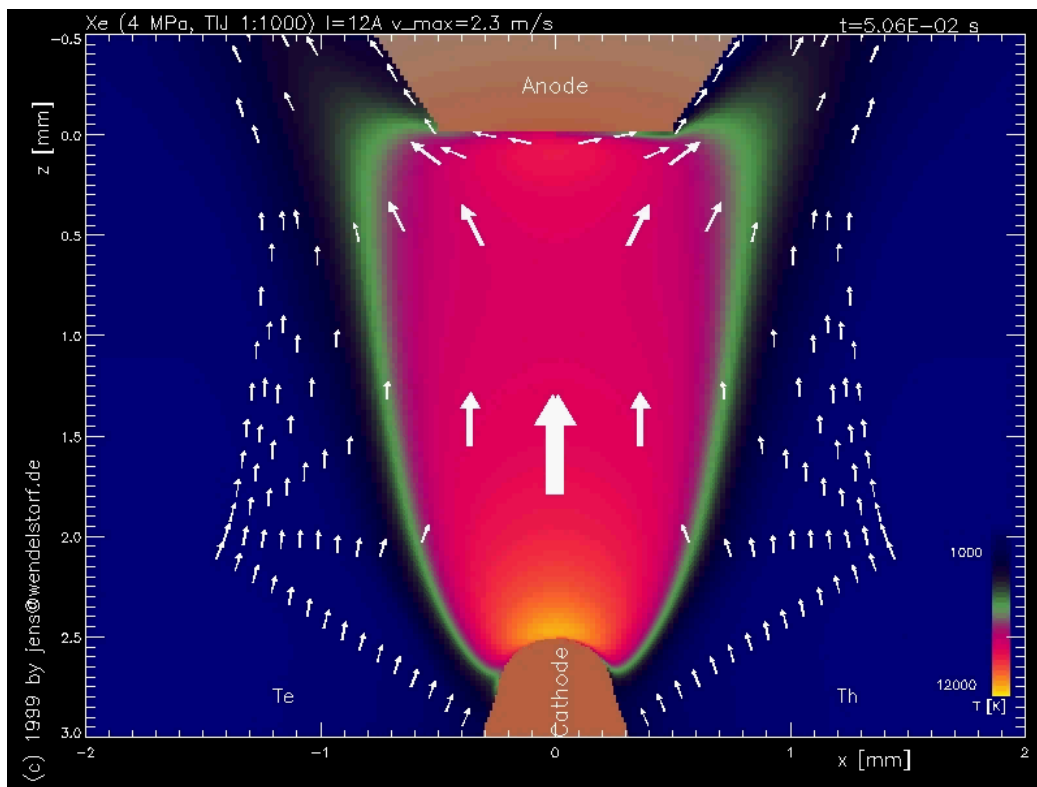


Figure 5.41: Temperature map and flow field of a doped xenon short arc lamp (4 MPa, 12A).

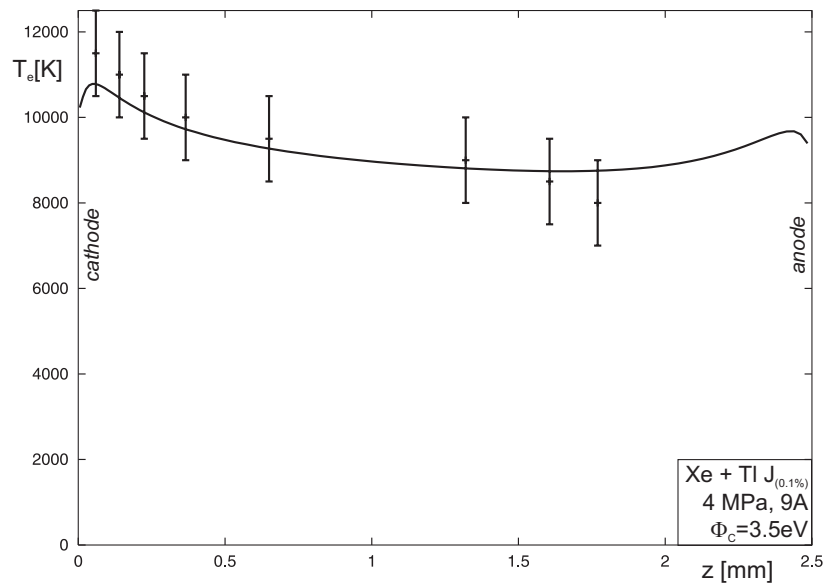


Figure 5.42: Temperature on the axis of a doped xenon short arc lamp (4 MPa, 9A). The measurement values are taken from [Hop87].

5.3.5 The high pressure mercury discharge

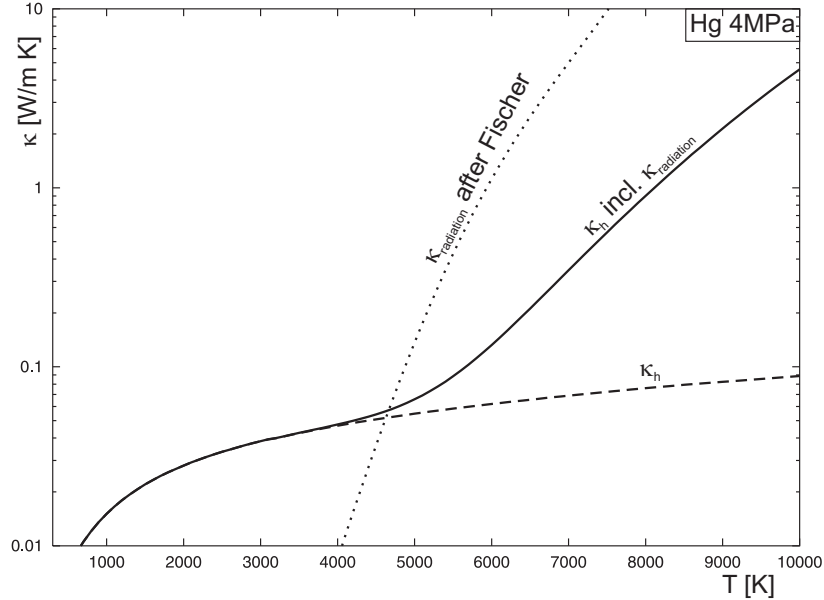


Figure 5.43: Temperature dependence of the heavy particles heat conductivity (mercury, 4 MPa). For comparison, the values obtained by equation 5.2 are also plotted.

Another important application area of thermal plasma gas discharges are high pressure mercury discharge lamps. Currently, low power lamps at pressure levels around 4 MPa are introduced for car headlight systems and even ultra high pressure lamps (8-20 MPa) for data and video projection systems are under development or already available. The modelling of these lamps was reviewed by Dakin [Dak89].

As shown in figure 5.44, the discharge is highly influenced by hydrodynamic phenomena. At atmospheric pressure, the flow field is dominated by magnetic forces and at 80 atmospheres, the natural convection forces become of the same importance. Due to the higher radiative and conductive losses, the discharge also constricts at higher pressure levels.

One of the specifics of such arc discharges is the increasing role of radiation transport phenomena with increasing pressure. Because detailed radiation transport is not included into the model, such effects are described by a radiative heat conductivity taking account of the optical thick radiation emitted and reabsorbed within the discharge. Such a radiative heat conductivity was computed by Fischer [Fis87] and was used by Giese [Gie97]³:

$$\begin{aligned} \kappa_{\text{radiation,Hg}} &= 6.1 \cdot 10^{-11} \cdot p \cdot e^{y(T)} & (5.2) \\ \text{with } y(T) &= 1.89 \cdot 10^{-14} \cdot T^4 - 4.0356 \cdot 10^{-10} \cdot T^3 \\ &\quad + 2.859 \cdot 10^{-6} \cdot T^2 - 5.303 \cdot 10^{-3} \cdot T \end{aligned}$$

For this work, the radiative heat conductivity was computed by Wilhelm [Wil96a], as shown in figure 5.43. The computed parameters for such a *D1-lamp* like discharge are provided in figure 5.45.

³like all quantities in this work, given in SI Units.

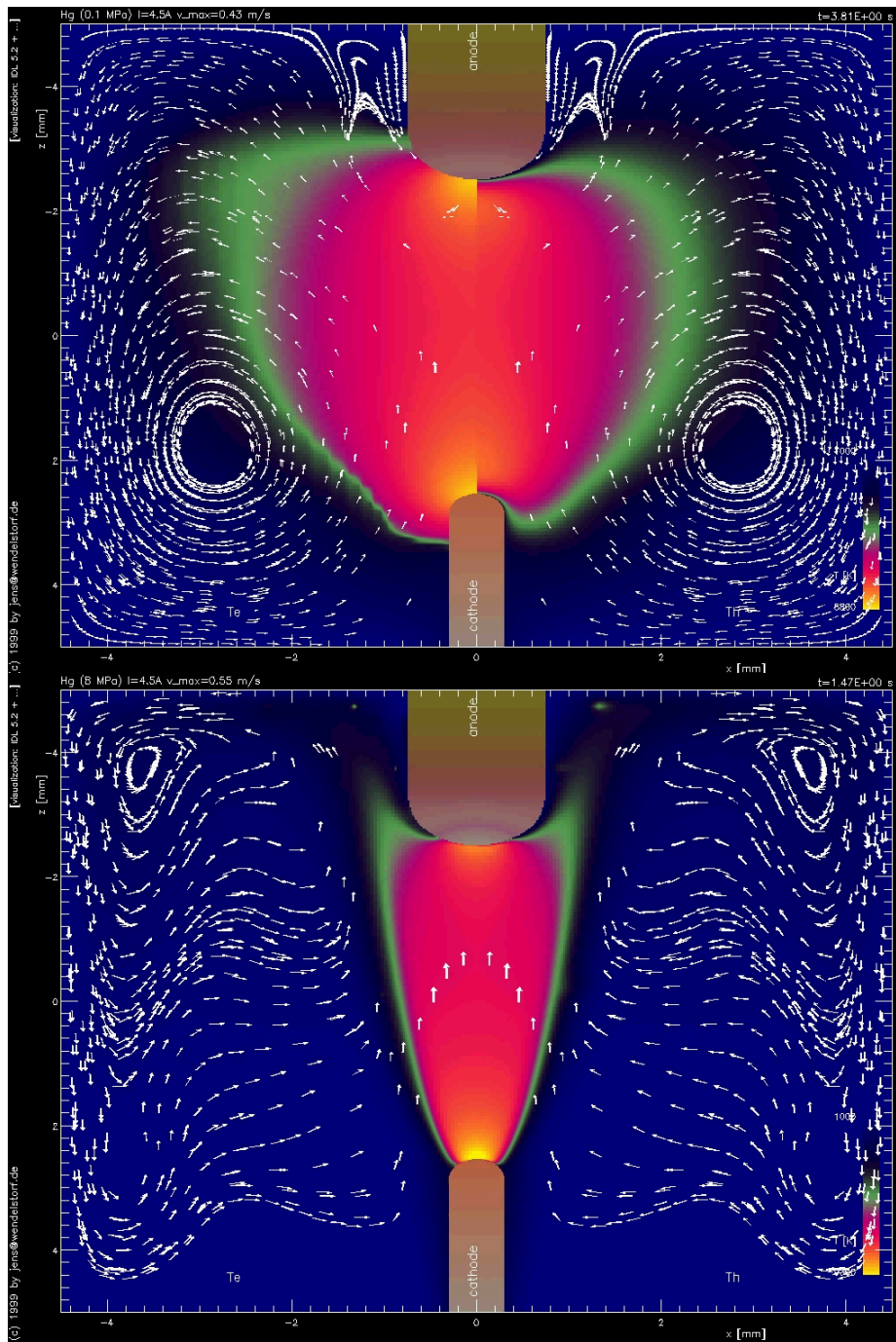


Figure 5.44: Temperature map and flow field of a 0.1 MPa (top) and 8 MPa (bottom) mercury discharge.

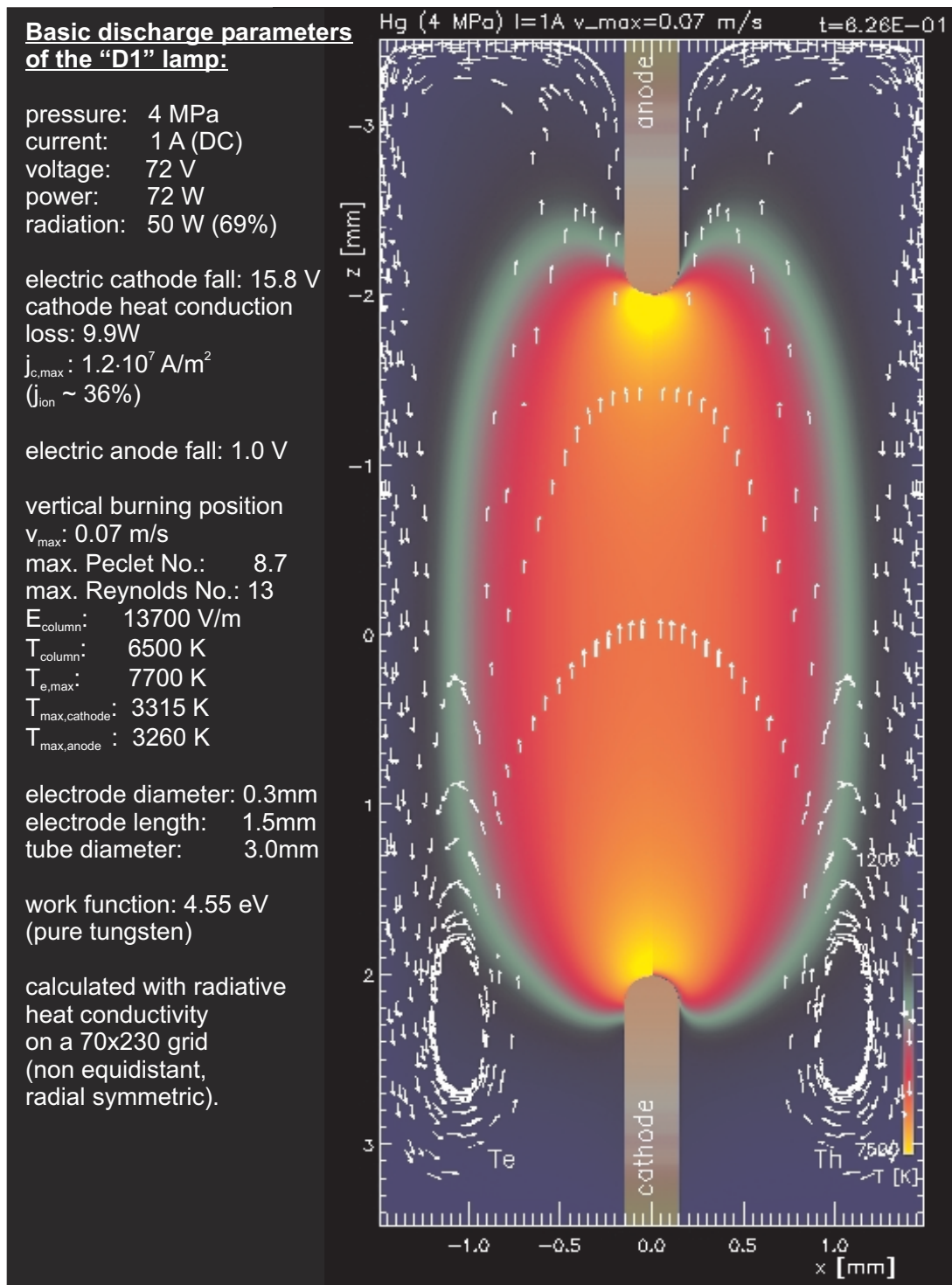


Figure 5.45: Basic discharge data for the calculated high pressure mercury lamp.

5.3.6 The TIG welding arc

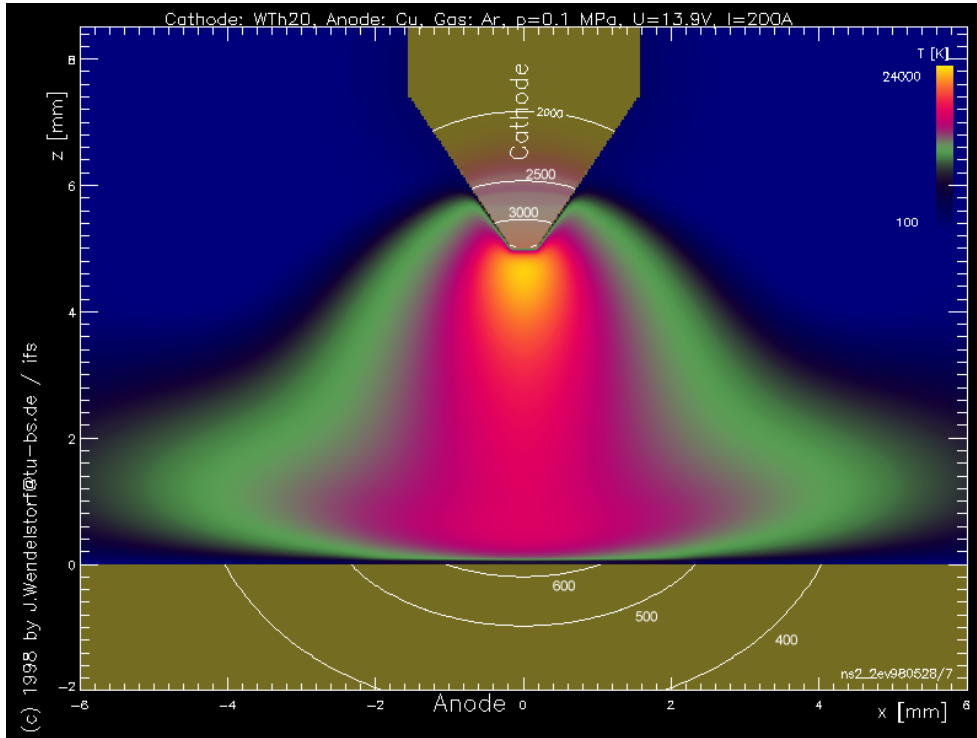


Figure 5.46: Temperature map of a 200A argon arc at atmospheric pressure (see text and [WDWS97a]).

Model/Exp	100A	200A
100A	-6%	+5%
200A	-18%	-7%

Table 5.3: Mean relative deviation of computed and measured arc temperature maps.

The atmospheric pressure argon arc burning between a tungsten cathode and a flat anode is one of the arc configurations investigated in depth by experimental techniques like emission spectroscopy [Bot66, Gli76, HF84, HEP83, Tho93], Laser scattering [MFH92] and Laser induced fluorescence [SMHR95]. Regarding the results of such spectroscopical arc temperature measurements, one has to take into account the small variation of arc temperature with arc current. In table 5.3, the mean deviation of measured and calculated arc temperature is provided for the LTE case. Comparing the computed 100A temperature map with the spectroscopical 200A temperature map gives a mean deviation still inside the experimental error bars.

Additionally, a number of independent groups have developed mathematical models for this so called standard welding arc [Lan92]. A detailed review can be found in [WDWS97b]. For this arc situation, a number of arc electrode models was published [DS90, ZLM92, LMH97]. Additionally, ambipolar diffusion and radiation transport was studied in depth [SHL00, MML00].

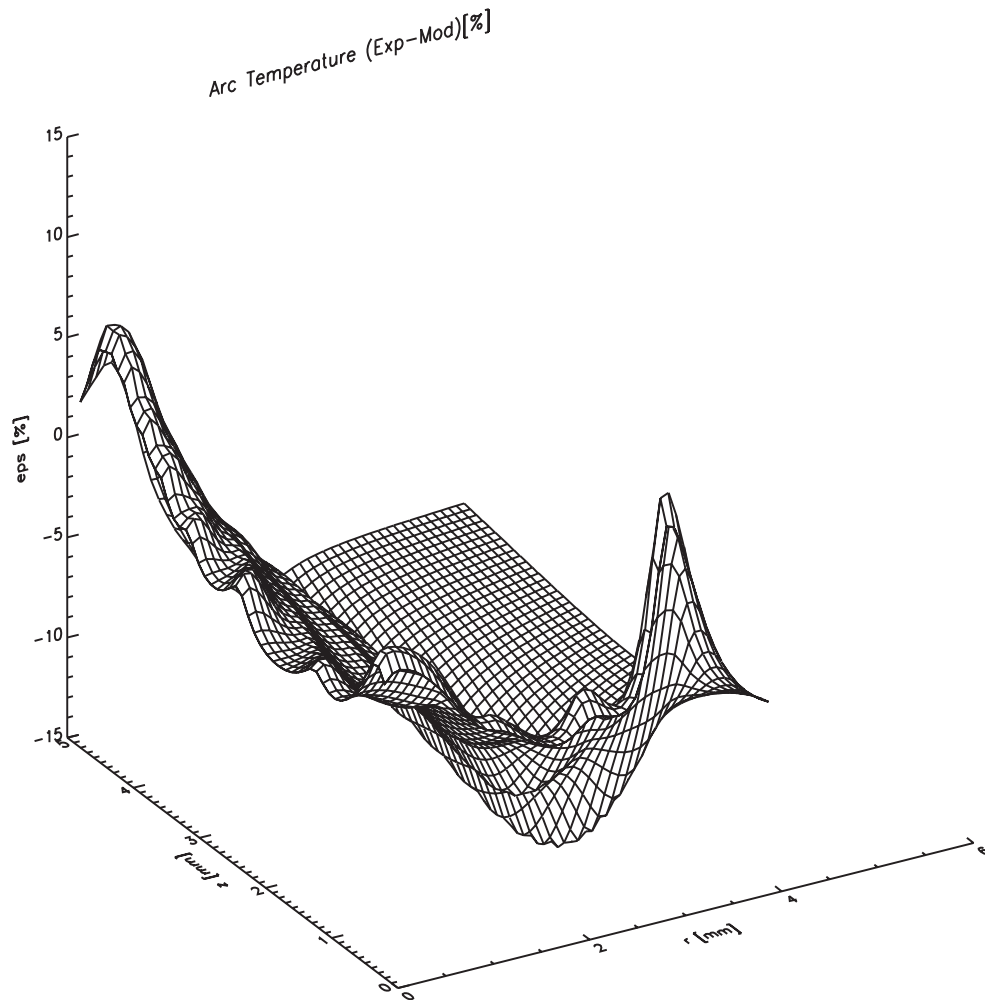


Figure 5.47: Relative deviation of the computed temperature map and the experimental data obtained by [Hsu82] (see text and [WDWS97a]).

Assuming LTE, the self consistent calculation of the arc electrode system is straightforward and the results agree with measured arc temperatures within the principal error.

While most experiments assume LTE for such a high current arc, there is strong evidence for non LTE effects near the electrodes [Ben97], as well as in the arc column [Hai97]. These calculations are in agreement with recent experiments [SLR93, SRF⁺94]. Using the pLTE plasma electrode model in this work, one can investigate this problem in larger detail.

5.4 Comparison with other modelling results

For the high pressure xenon model lamp (section 5.3.2), a comparison of this work (BS) with the results of a model developed by Wiesman [Wie98] and Flesch [FWN00] in the group of Prof. Neiger at Karlsruhe (LTI) is possible. The LTI model is based on a non-LTE electric conductivity equation, originally introduced by Fischer [Fis87]. It solves the (LTE) heat conduction and current continuity equation on a very fine finite element grid.

	U [V]	U_C [V]	E [V/m]	T_C [K]	$P_{C,\infty}$ [W]
BS	19.4	9.9	622	3299	5.8
LTI	22.8	8.6	636	3474	6.0

Table 5.4: Basic discharge parameters calculated by this work (BS) and the model developed in Karlsruhe (LTI) for a long arc xenon model lamp (1 MPa, 4.5A, $\Phi_{eff} = 4.55$ eV, $d_C = 0.6$ mm, $l_{arc} = 20$ mm).

As shown in table 5.4, the results are quite similar. Compared to the results presented in table 5.2, the BS-values were obtained including fluid flow and for $r_A = 0.3$ mm. The overall arc voltage may show better agreement with experiment for the LTI model, because of an underestimation of the anode fall by the model presented in this work. Because of the missing space charge layer model, the LTI values for the cathode tip temperatures may be found to be more inaccurate than the BS ones.

	U [V]	U_C [V]	E [V/m]	T_C [K]	$P_{C,\infty}$ [W]
BS	71.1	16.4	13400	3264	9.6
LTI	82.4	19.8	13900	3331	9.5

Table 5.5: Basic discharge parameters calculated by this work (BS) and the model developed in Karlsruhe (LTI) for a short arc mercury lamp (0.75A, other parameters see figure 5.45).

The same agreement is found by comparing the results obtained by the different models for a high pressure mercury short arc lamp (table 5.5). The differences in the arc voltage is a result of the different anode falls computed (0.9V for this model and 7.0V for the LTI one).

This comparison allows for a very important conclusion: The arc and electrode fall voltages mainly depend on the electrode work function and the temperature dependence of the electric conductivity. Including the most important effects governing the overall discharge self-consistently into the model, one will get similar results. These most important physical processes are:

- electron emission at the cathode surface.
- current and energy transport in the thermal plasma region.

While the model presented here (BS), was developed for maximum physical self consistency, even a model neglecting flow and sheath phenomena (LTI) may allow for a computation of the arc voltage current characteristics. This picture may change for the prediction of discharge parameters which are more sensitive to flow phenomena (see table 5.1).

The number of references describing a self-consistent arc modelling approach is limited to this work, the LTI approach and the work done at CSIRO in Australia (see e.g. [LMH97]). For the model presented here, results in a pressure range of 0.1 to 8 MPa are available. The LTI model is restricted to pressures above 1 MPa, LTE discharges and neglects fluid flow phenomena. For the CSIRO model, only results for a high current atmospheric argon arc were published.

Taking into account modelling approaches with fit parameters (e.g. the peak current density at the cathode surface) or calculating only one specific region of the arc, there is a large amount of literature available. Most of these references deal with the TIG welding arc situation and are discussed in [WDWS97b].

Some of the high pressure mercury lamp models presented in the literature provide results for a three dimensional flow situation [CS92, Gie97]. Because of the missing cathode and anode layer model, the only measureable quantity provided is the arc temperature distribution. In [Gie97], a reasonable number of different discharge situations was modeled. The results show the impact of natural convection, especially for the horizontal burning position and high discharge pressures. Because the magnetic compression forces were neglected, the results are rather questionable both quantitatively and qualitatively, especially near the electrodes. No arc burning voltages were presented in [Gie97].

5.5 Summary of the modelling results and validation

This chapter has provided modelling results for a wide range of discharge parameters as well as a discussion of the influence of the individual physical effects on the overall discharge behaviour. It can be regarded as an in depth presentation of arc discharge properties based on *ab initio* mathematical modelling. Special emphasis was given to the impact of fluid flow and its specific driving forces.

Based on the results of a physical sensitivity analysis, an attempt was made to validate the model by comparison with experimental data. For discharges in LTE or near LTE, the available experimental data justifies the physical model.

A more detailed and accurate validation can be performed by enhancing the numerical calculation schemes to allow for the calculation of longer arcs and mode transitions using less computing time. The uncertainties of the electrode work function values and of the cross section and radiative data will require special strategies for an increase and test of the models accuracy.

Damit das Mögliche entsteht,
muß immer wieder das Unmögliche versucht werden.
Hermann Hesse

Chapter 6

Summary, applications, outlook and conclusions

This work is dedicated to the quantitative prediction of the physical and technological parameters of a large class of gas discharges, the electric arcs. The fundamental physical mechanisms of such electric discharges were described first by J. Stark at the beginning of the twentieth century [Sta03]. Based on one century of fundamental research on arc physics, models of the individual discharge regions were developed or applied and finally integrated to a complete self-consistent description of the *synergetic system electric arc discharge*.

In this chapter, the major achievements, especially in the realized modelling concept, are summarized, the application areas are sketched and finally some future developments are encouraged, followed by a final conclusion.

6.1 Major achievements

Within the scientific literature, there is a large amount of papers dedicated to the modelling of individual features of specific arc discharges (reviews are provided by [FS89, Cif91, ALS95, WDWS97b]). Restricting the search to references dealing with the quantitative computation of measurable global arc properties, like the arc voltage, the situation changes to a few references only [DS90, ZLM92, LMH97, FWN00]. This work allows for a quantitative prediction of the discharge properties with the highest physical consistency currently available:

- The cathode layer model includes a self consistent space charge sheath and presheath model, allowing for an accurate calculation of the cathode fall voltage and, by a precise treatment of the surface energy balance, of the cathode surface temperature and electric current density distribution.
- The anode sheath is described by a simple physical self consistent model including a space charge layer. The importance of diffusive current transport was emphasized.
- The overall arc electrode system was quantitatively predicted *ab initio* by a physical self consistent and numerically stable iterative scheme.
- The required transport coefficients were calculated for the partial local thermodynamic equilibrium (pLTE) case ($T_e \neq T_h$) and the influence of the cross section data precision was discussed.

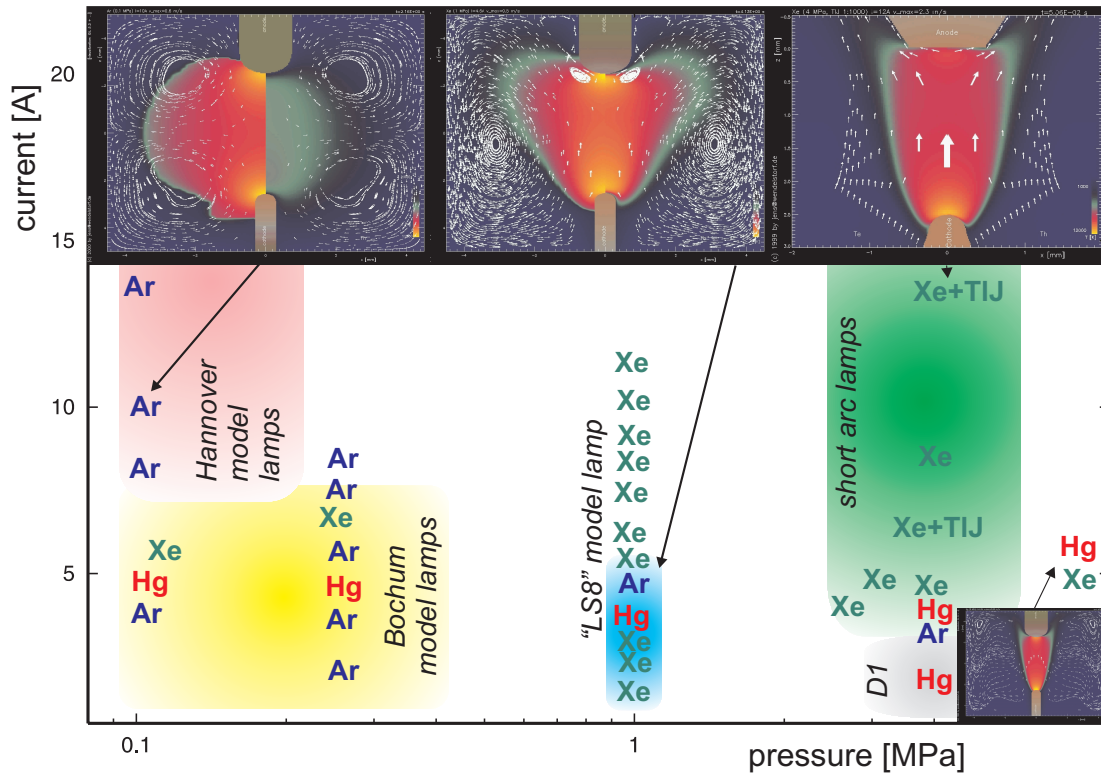


Figure 6.1: Calculated arc discharge configurations.

- By calculating a large number of arc configurations (see figure 6.1) for currents above 1 A, several discharge gases and for pressure levels from 0.1 to 8 MPa, the model has proved its ability to reproduce all major discharge features.
- The sensitivity analysis has shown the relevance of the specific physical processes with respect to the resulting arc parameters, especially the impact of fluid flow.
- The relevance of the different driving forces of the flow was visualized and discussed.
- The validation by comparison with existing experimental data has proven the quantitative accuracy of the model.

The modelling results were obtained by a large computer code (algorithmic complexity) using a large amount of computing time (logical depth). A comparison with similar approaches [DS90, ZLM92, LMH97, FWN00] is restricted to the comparison of modelling results available for identical discharge configurations. It was performed for the model developed at the University of Karlsruhe (LTI, [FWN00]).

A comparison of the results with available experimental data was provided for the quantitative measurement data sets available. The validation of the model was found to be limited by the required agreement of the computed and measured arc configuration, by the limited experimental accuracy and by the precision of the numerical solutions resulting from the numerical grid spacing and the inaccuracy of the input data, especially the cathode material work function.

As a conclusion, the LTE arc column and the cathode fall calculation was found to be as accurate as the experimental determination of cathode fall voltages and arc temperature distributions. The anode layer model may be regarded to provide a lower limit for the anode fall voltage and is the first self consistent one not neglecting space charge formation in front of the anode. A more detailed validation of the model will require a large number of accurate experiments obtained for discharges mainly in local thermodynamic equilibrium (LTE). This may also allow for a determination of parameters like the cathode work function by solving an inverse problem. Within the limitations of the computing requirements and the experimental precision, the model was found to be suitable for a quantitative prediction of arc discharge data within a pressure range of 0.1 to 8 MPa and currents above 1 A.

6.2 Conceptual progress

The physical model has a large degree of self consistency by iteratively linking 2D plasma and 1D sheath models. Its success is based on the principle of applying different models to physically different regions, instead of trying to describe the overall discharge by a single set of equations. Compared to the LTI approach, the number of discretization points required is orders of magnitude smaller. The current implementation was optimized in terms of development time and thus wasting computing time by the missing solution adapted numerical mesh. This is not a disadvantage of the model itself. Additionally the *transfer function* approach for boundary layer modelling is very general and can be implemented into other existing computational fluid dynamics (CFD) or finite element (FEM) models.

The self consistent locally defined space charge layer model may be regarded as the most important part of the approach, but the overall realization of the scheme was clearly the most complex part of this work.

6.3 Applications

The range of possible applications of such an *ab initio* predictive modelling approach is as wide as the application area of arc discharges itself. While the actual model is (numerically) restricted to stationary direct current (DC) discharges with cylindrical symmetry, the first applications will lie in the field of high intensity discharge (HID) lamps. One of the direct application areas are high pressure short arc lamps used for projection devices, searchlights, laser pumping and other areas where large light intensities are required. Such products may be improved by modelling and/or model enhanced experimental optimization. Especially for high pressure mercury discharges, additional radiation transport modelling will be required. As a conclusion, the model may change the way of light source development from *trial and error* to *computational prediction and optimization*.

Electric arc discharges are also applied as energy sources for high temperature material processing. New cutting, welding and spraying torches, as well as other new arc applications may be developed on the basis of the model. Currently, the optimization of DC tungsten inert gas welding processes (TIG/GTAW), as well as plasma arc welding (PAW) is in reach of the model. A few enhancements of the numerical procedures will also allow for an optimization of arc furnaces for metal and mineral processing and waste destruction. More sophisticated enhancements of the numerics are required for modelling transient arc discharges, which can be found in circuit breakers and switches.

6.4 Future developments

The possible enhancements of the model can be divided into three different fields. First, the physical model can be optimized by implementing the generalized Ohms law, ambipolar diffusion within the arc core, other diffusion and demixing processes and a more detailed radiation transport model. Second, the numerical solution has to be optimized by transferring the approach to a commercial CFD software package. Finally, the problem of bifurcations (mode transitions), multiple solution hysteresis and all other aspects of discharge complexity can be addressed by further fundamental research. All these enhancements strongly interact with each other and have to be carefully planned and weighted against the available development resources.

Parallel to the model enhancement, validation experiments have to be performed. It is proposed to optimize the input parameters (cathode work function, cross section and radiative data) for a best fit to one set of experimental data and to test the extrapolation capability of the model by comparison with a second set of experimental data.

6.5 Conclusions

Thermal plasma gas discharges (electric arcs) are complex self organizing dissipative physical systems. For specific parameter sets representing an increasing survival pressure, the discharge reorganizes itself to a more sophisticated spatial structure (symmetry breaking) or self organized criticality (constricted electrode attachment).

While such complex natural phenomena are actually mostly unpredictable, this work has shown the possibility of quantitative and *ab initio* computation of complete and really existing discharge configurations. The physical description was found to be more general than the actual numerical implementation, which is limited to the stationary radial symmetric case.

The final conclusion is the practical predictability of this type of gas discharges by mathematical modelling. It was achieved by a proper balance of physical understanding and application oriented numerical software development. The computational effort was $10^{11\dots 12}$ floating point operations per discharge configuration.

Bibliography

- [AC97] M Y Amusia and L V Chernysheva, *Computation of atomic processes*, IOP Publishing, 1997.
- [ADDG92] J D Anderson, G Degrez, E Dick, and R Grundmann, *Computational fluid dynamics*, Springer-Verlag, 1992.
- [AF83] J Aubreton and P Fauchais, *Influence des potentiels d'interaction sur les proprietes de transport des plasmas theramiques: exemple d'application le plasma argon hydrogene a la pression atmospherique*, *Revue de Physique Applique* (supplement to *Journal de Physique*) **18** (1983), 51–66.
- [AJHP98] T Amakawa, J Jenista, J Heberlein, and E Pfender, *Anode-boundary-layer behaviour in a transferred, high-intensity arc*, *J. Phys. D: Appl. Phys.* **31** (1998), no. 20, 2826–2834.
- [ALS95] H G Adler, R W Liebermann, and R Speer, *HID-Modelling and experimental assessment*, 7th International Symposium on Science and Technology of Light Sources, Kyoto, Japan (R Itatani and S Kamiya, eds.), August 1995, pp. 203–204.
- [AN72] B H Armstrong and R W Nichols, *Emission, absorption and transfer of radiation in heated atmospheres*, Pergamon Press, 1972.
- [And90] A Anders, *A formulary for plasma physics*, Akademie-Verlag, 1990.
- [Ayr02] H Ayrton, *The electric arc*, The Electrician Printing and Publishing Co., New York, 1902.
- [Bak90] V Bakshi, *Saha equation for a two temperature plasma*, *Phys. Rev. A* **42** (1990), no. 4, 2460.
- [BAM85] C Bonnefoi, J Aubreton, and J M Mexmain, *New approach taking into account elastic and inelastic processes for transport properties of two temperature plasmas*, *Z. Naturforsch.* **40a** (1985), 885–891.
- [Bau62] U H Bauder, *Radiation from high pressure plasmas*, *J. Appl. Phys.* **39** (1962), no. 1, 148–152.
- [BB57] J N Butler and R S Brokaw, *Thermal conductivity of gas mixtures in chemical equilibrium*, *J. Chem. Phys.* **26** (1957), no. 6, 1636–1643.

- [BB00] R Böttcher and W Böttcher, *Numerical modelling of arc attachment to cathodes of high-intensity discharge lamps*, J. Phys. D: Appl. Phys. **33** (2000), 367–374.
- [BCP99] S Brugeat, H Coitout, and M J Parizet, *Study of Ar-CO₂ and Ar-N₂ thermal plasma*, XXIV International Conference on Phenomena in Ionized Gases (ICPIG), Warsaw, Poland (P Pisarczyk, T Pisarczyk, and J Wolowski, eds.), vol. 2, July 1999, pp. 53–54.
- [Ben97] M S Benilov, *Analysis of thermal non-equilibrium in the near-cathode region of atmospheric-pressure arcs*, J. Phys. D: Appl. Phys. **30** (1997), 3353–3359.
- [BFP94] M I Boulos, P Fauchais, and E Pfender, *Thermal Plasmas. Fundamentals and Applications*, vol. 1, Plenum Press, New York, 1994.
- [BM95] M S Benilov and A Marotta, *A model of the cathode region of atmospheric pressure arcs*, J. Phys. D: Appl. Phys. **28** (1995), 1869–1882.
- [BN98] M S Benilov and G V Naidis, *Ionization layer at the edge of a fully ionized plasma*, Phys. Rev. E **57** (1998), no. 2, 2230–2241.
- [Boh49] D Bohm, *Minimum ionic kinetic energy for a stable sheath*, The characteristics of electrical discharges in magnetic fields (A Guthrie and R K Wakerling, eds.), McGraw-Hill, New York, 1949, pp. 77–86.
- [Bon83] C Bonnefoi, *Contribution a l'etude des methodes de resolution de l'equation de boltzmann dans un plasma a deux temperatures: exemple le melange argon-hydrogene*, Ph.D. thesis, Universite de Limoges, France, May 1983.
- [Bot66] J F Bott, *Spectroscopic measurements of temperatures in an argon plasma arc*, Phys. Fluids **9** (1966), no. 8, 1540–1547.
- [BP97a] R Badii and A Politi, *Complexity: hierarchical structures and scaling in physics*, Cambridge nonlinear science series, vol. 6, Cambridge University Press, Cambridge, UK, 1997.
- [BP97b] U H Bauder and Schmidt H P, *Sparks, arcs, and other electric discharges*, Encyclopedia of Applied Physics (G L Trigg, ed.), vol. 19, VCH Publishers, Weinheim, 1997, pp. 157–187.
- [Bra65] S I Braginskii, *Transport processes in a plasma*, Reviews of plasma physics (M A Leontovich, ed.), vol. 1, Consultants Bureau, New York, 1965, pp. 205–311.
- [Bro60] R S Brokaw, *Thermal conductivity of gas mixtures in chemical equilibrium. II*, J. Chem. Phys. **32** (1960), no. 4, 1005–1006.
- [BS54] A Bauer and P Schulz, *Elektrodenfälle und Bogengradienten in Hochdruckentladungen, insbesondere bei Xenon*, Z. Phys. **139** (1954), 197–211.
- [BSL60] R B Bird, W E Stewart, and E N Lightfoot, *Transport phenomena*, Wiley, 1960.

- [BVY87] L M Biberman, V S Vorob'ev, and I T Yakubov, *Kinetics of nonequilibrium low-temperature plasmas*, Plenum Press, New York, 1987.
- [Cap72] M Capitelli, *Cut-off criteria of electronic partition functions and transport properties of thermal plasmas*, J. Plasma Phys. **7** (1972), 99–106, part 1.
- [CG98] B Chervy and A Gleizes, *Electrical conductivity in thermal plasma at low temperature (1000-5000 K)*, J. Phys. D: Appl. Phys. **31** (1998), no. 19, 2557–2565.
- [CH99] X Chen and P Han, *On the thermodynamic derivation of the saha equation modified to a two-temperature plasma*, J. Phys. D: Appl. Phys. **32** (1999), 1711–1718.
- [Cif91] L Cifuentes, *High-pressure discharge lamps: approaches to modelling*, Lighting Research and Technology **23** (1991), no. 4, 161–165.
- [CPR88] L E Cram, L Poladian, and G Roumeliotis, *Departures from equilibrium in a free-burning argon arc*, J. Phys. D: Appl. Phys. **21** (1988), 418–425.
- [CS92] P Y Chang and W Shyy, *A study of three-dimensional natural convection in high-pressure mercury lamps. III. Arc centering by magnetic field*, Int. J. Heat Mass Transfer **35** (1992), no. 8, 1857–1864.
- [CZA96] K Charrada, G Zissis, and M Aubes, *Two-temperature, two-dimensional fluid modelling of mercury plasma in high-pressure lamps*, J. Phys. D: Appl. Phys. **29** (1996), no. 9, 2432–2438.
- [Dak89] J T Dakin, *Predicting high-pressure discharge performance*, 5th international symposium on science and technology of light sources, York (R Devonshire, J Meads, and D O Wharmby, eds.), September 1989, pp. 316–324.
- [Dev65] R S Devoto, *The transport properties of a partially ionized monoatomic gas*, Ph.D. thesis, Stanford University, 1965.
- [Dev67] R S Devoto, *Simplified expressions for the transport properties of ionized monoatomic gases*, Phys. Fluids **10** (1967), no. 10, 2105–2112.
- [Dev73] R S Devoto, *Transport coefficients of ionized argon*, Phys. Fluids **16** (1973), 616–623.
- [DF65] H W Drawin and P Felenbok, *Data for plasmas in local thermodynamic equilibrium*, Gauthier-Villars, Paris, 1965.
- [Din79] H A Dinulescu, *Analysis of the anode boundary layer of a high pressure - high current arc*, Ph.D. thesis, University of Minnesota, Minneapolis, 1979.
- [DS90] C Delalondre and O Simonin, *Modelling of high intensity arcs including a non-equilibrium description of the cathode sheath*, J. Physique Coll. **51** (1990), no. C5, 199–206.

- [EFF⁺91] W Ebeling, Förster, Fortov, Gryaznov, and Polishchuk, *Thermodynamical properties of hot dense plasmas*, Teubner Texte zur Physik, vol. 25, Teubner Verlag, 1991.
- [Ete93] K Etemadi, *Energy balance in a welding arc with evaporating anode*, private communication, 1993.
- [Fis87] E Fischer, *Modelling of low-power high-pressure discharge lamps*, Philips J. Research **42** (1987), 58–85.
- [FM57] W Finkelnburg and H Maecker, *Elektrische Bögen und thermisches Plasma*, Gasentladungen II (S Flügge, ed.), Handbuch der Physik, vol. 22, Springer, 1957, pp. 254–444.
- [FNT93] N Femia, L Niemeyer, and V Tucci, *Fractal characteristics of electrical discharges: experiments and simulation*, J. Phys. D: Appl. Phys. **26** (1993), 619–627.
- [FP64] L S Frost and A V Phelps, *Momentum-transfer cross sections for slow electrons in He, Ar, Kr, and Xe from transport coefficients*, Phys. Rev. A **136** (1964), no. 6, 1538–1545.
- [FP99] J H Ferziger and M Peric, *Computational methods for fluid dynamics*, 2 ed., Springer, 1999.
- [FS89] E Fischer and E Schnedler, *Chemical and physical modelling of metal halide discharges - today and tomorrow*, 5th International Symposium on Science and Technology of Light Sources, York (R Devonshire, J Meads, and D O Wharmby, eds.), September 1989, pp. 91–100.
- [FWN00] P Flesch, H Wiesmann, and M Neiger, *Grundlagenuntersuchungen der Eigenschaften thermisch emittierender Kathoden für Gasentladungen - Teilvorhaben: Modellierung von Elektrodenprozessen im Rahmen eines selbstkonsistenten Gesamtmodells*, Abschlußbericht BMBF FK 13N7107/0, Universität Karlsruhe, Lichttechnisches Institut, Juli 2000.
- [GCG99] A Gleizes, B Chervy, and J J Gonzalez, *Calculation of a two-temperature plasma composition: bases and application to SF₆*, J. Phys. D: Appl. Phys. **32** (1999), 2060–2067.
- [Gie97] H Giese, *Theoretische Untersuchungen zur Konvektion in Quecksilber-Hochdruckgasentladungslampen*, Dissertation, Universität Karlsruhe, Verlag der Augustinus-Buchhandlung, Aachen, 1997.
- [Gli76] S S Glickstein, *Temperature measurements in a free burning arc*, Welding Journal **55** (1976), no. 8, 222s–229s.
- [Gri62] H R Griem, *High density corrections in plasma spectroscopy*, Phys. Rev **128** (1962), no. 3, 997–1003.
- [Gri64] H R Griem, *Plasma spectroscopy*, McGraw-Hill, 1964.

- [Hai97] J Haidar, *Departures from local thermodynamic equilibrium in high-current free burning arcs in argon*, J. Phys. D: Appl. Phys. **30** (1997), no. 19, 2737–2743.
- [Hai99] J Haidar, *Non-equilibrium modelling of transferred arcs*, J. Phys. D: Appl. Phys. **32** (1999), no. 3, 263–272.
- [HCB64] J O Hirschfelder, C F Curtiss, and R B Bird, *Molecular theory of gases and liquids*, 2nd ed., John Wiley, 1964.
- [HEP83] K C Hsu, K Etemadi, and E Pfender, *Study of the free-burning high-intensity argon arc*, J. Appl. Phys. **54** (1983), 1293–1301.
- [HF84] G N Haddad and A D J Farmer, *Temperature determination in a free burning arc: I. experimental techniques and results in argon*, J. Phys. D: Appl. Phys. **17** (1984), 1189–1196.
- [HL67] M I Hoffert and H Lien, *Quasi-one-dimensional, non-equilibrium gas dynamics of partially ionized two-temperature argon*, Phys. Fluids **10** (1967), no. 8, 1769–1777.
- [Hop87] R Hoppstock, *Xenon-Hochdruck-Kurzbogenlampen mit Metallhalogenid-Dotierung und Wolfram-Halogen-Kreisprozeß*, Dissertation, Universität Karlsruhe, 1987.
- [HP83a] K C Hsu and E Pfender, *Analysis of the cathode region of a free-burning high intensity argon arc*, J. Appl. Phys. **54** (1983), no. 7, 3818–3824.
- [HP83b] K C Hsu and E Pfender, *Two-temperature modeling of the free-burning, high-intensity arc*, J. Appl. Phys. **54** (1983), 4359–4366.
- [Hsu82] K C Hsu, *A self consistent model for the high intensity free burning argon arc*, Ph.D. thesis, University of Minnesota, Minneapolis, USA, 1982.
- [HV97] H Haken and R Vallee, *Synergetics and cybernetics*, Encyclopedia of Applied Physics (G L Trigg, ed.), vol. 20, VCH Publishers, Weinheim, 1997, pp. 407–427.
- [Iti78] Y Itikawa, *Electron-atom momentum-transfer cross sections*, Atomic Data and Nuclear Data Tables **21** (1978), no. 1, 69–75.
- [Jüt97] B Jüttner, *The dynamics of arc cathode spots in vacuum: new measurements*, J. Phys. D: Appl. Phys. **30** (1997), no. 2, 221–229.
- [KB77] D Kannappan and T K Bose, *Transport properties of a two temperature argon plasma*, Phys. Fluids **20** (1977), no. 10, 1668–1673.
- [Kim74] C W Kimblin, *Cathode spot erosion and ionization phenomena in the transition from vacuum to atmospheric pressure arcs*, J. Appl. Phys. **45** (1974), 5235–5244.
- [KPS94] T Klein, J Paulini, and G Simon, *Time-resolved description of cathode spot development in vacuum arcs*, J. Phys. D: Appl. Phys. **27** (1994), no. 9, 1914–1921.

- [Kru70] C H Kruger, *Nonequilibrium in confined arc plasmas*, Phys. Fluids **13** (1970), no. 7, 1737–1746.
- [KSGK99] F Könemann, E Schulz-Gulde, and M Kock, *Evidence of non-equilibrium near the cathode of a low current argon arc*, XXIV International Conference on Phenomena in Ionized Gases (ICPIG), Warsaw, Poland (P Pisarczyk, T Pisarczyk, and J Wolowski, eds.), vol. II, July 1999, pp. 195–196.
- [KSM+00] M Kock, E Schulz, W Mende, F Könemann, J Reiche, A Knoche, and G Kühn, *Grundlagenuntersuchungen der Eigenschaften thermisch emittierender Kathoden für Gasentladungen - Teilvorhaben: Spektroskopischer Nachweis von erodiertem Elektrodenmaterial im Kathodenbereich von Gasentladungslampen*, Abschlußbericht BMBF 13N7106/0, Institut für Atom- und Molekülphysik, Abteilung Plasmaphysik, Uni Hannover, Germany, July 2000.
- [Kul71] P P Kulik, *High-temperature viscosity and thermal conductivity of argon*, High Temperature **9** (1971), 389–390.
- [LA99] G G Lister and H G Adler, *Modeling and diagnostics of HID lamp electrodes*, XXIV International conference on phenomena in ionized gases (ICPIG), Warsaw, Poland (P Pisarczyk, T Pisarczyk, and J Wolowski, eds.), vol. I, July 1999, pp. 229–230.
- [Lan92] J F Lancaster, *TIG arc configuration for temperature and other measurements*, IIW Doc. No. 212-821-92, 1992, International Institute of Welding, Study group 212: Physics of welding.
- [Lib59] R L Liboff, *Transport coefficients determined using the shielded coulomb potential*, Phys. Fluids **2** (1959), no. 1, 40–46.
- [LL94] M A Lieberman and A J Lichtenberg, *Principles of plasma discharges and materials processing*, John Wiley and Sons, 1994.
- [LMH97] J J Lowke, R Morrow, and J Haidar, *A simplified unified theory of arcs and their electrodes*, J. Phys. D: Appl. Phys. **30** (1997), no. 14, 2033–2042.
- [LNBM99] J Luhmann, D Nandelstaedt, A Barzik, and J Mentel, *Measurement of the cathode fall in a high pressure argon model lamp*, XXIV International Conference on Phenomena in Ionized Gases (ICPIG), Warsaw, Poland (P Pisarczyk, T Pisarczyk, and J Wolowski, eds.), vol. 1, July 1999, pp. 13–14.
- [Low74] J J Lowke, *Predictions of arc temperature profiles using approximate emission coefficients for radiation losses*, Journal of Quantitative Spectroscopy and Radiative Transfer **14** (1974), 111–22.
- [Mac29] S S MacKeown, *The cathode drop in an electric arc*, Phys. Rev. **34** (1929), 611–617.
- [Mae51] H Maecker, *Der elektrische Lichtbogen*, Ergebnisse der Exakten Naturwissenschaften **25** (1951), 293–358.
- [Man82] B B Mandelbrot, *The fractal geometry of nature*, Freeman, San Francisco, 1982.

- [MC58] C Muckenfuss and C F Curtiss, *Thermal conductivity of multicomponent gas mixtures*, J. Chem. Phys. **29** (1958), no. 6, 1273–1277.
- [MFH92] A B Murphy, A J D Farmer, and J Haidar, *Laser-scattering measurement of temperature profiles of a free-burning arc*, Appl. Phys. Lett. **60** (1992), no. 11, 1304–1306.
- [MHP99] J Menart, J Heberlein, and E Pfender, *Theoretical radiative transport results for a free-burning arc using a line-by-line technique*, J. Phys. D: Appl. Phys. **32** (1999), no. 1, 55–63.
- [MML00] J Menart, S Malik, and L Lin, *Coupled radiative, flow and temperature-field analysis of a free-burning arc*, J. Phys. D: Appl. Phys. **33** (2000), 257–269.
- [MMS67] E A Mason, R J Munn, and F J Smith, *Transport coefficients of ionized gases*, Phys. Fluids. **10** (1967), no. 8, 1827–1832.
- [Mon99] R Montero, *Numerische Berechnung der Transporteigenschaften thermischer Plasmen*, Diplomarbeit, TU-Braunschweig, Institut für Theoretische Physik, July 1999.
- [Mur98] A B Murphy, *Cataphoresis in electric arcs*, J. Phys. D: Appl. Phys. **31** (1998), no. 23, 3383–3390.
- [NL78] Y Nakamura and J Lucas, *Electron drift velocity and momentum cross-section in mercury, sodium and thallium vapours: II. Theoretical*, J. Physics D: Appl. Phys. **11** (1978), 337–345.
- [Ols59] H N Olsen, *Thermal and electrical properties of an argon plasma*, Phys. Fluids **2** (1959), 614–623.
- [Pan93] R L Panton, *Fluid dynamics, equilibrium*, Encyclopedia of Applied Physics (G L Trigg, ed.), vol. 6, VCH Publishers, Weinheim, 1993, pp. 409–436.
- [Pan94] I G Panevin, *Near electrode processes*, Thermal Plasma and new materials technology (O P Solonenko and M F Zhukov, eds.), vol. 1, Cambridge Interscience Publishing, 1994, pp. 203–227.
- [Pat80] S V Patankar, *Numerical heat transfer and fluid flow*, Hemisphere Publishing, Taylor and Francis, 1980.
- [PKS93] J Paulini, T Klein, and G Simon, *Thermo-field emission and nottingham effect*, J. Phys. D: Appl. Phys. **26** (1993), 1310–1315.
- [PP99] A V Phelps and Z L Petrovic, *Cold-cathode discharges and breakdown in argon: Surface and gas phase production of secondary electrons*, Plasma Sources Science and Technology **8** (1999), no. 3, R21–R44.
- [PPB⁺92] I Peres, L C Pitchford, J P Boeuf, H Gielen, and P Postma, *Current voltage characteristics in low pressure cold cathode argon discharges*, 6th International Symposium on the Science and Technology of Light Sources, Budapest (L Bartha and F J Kedves, eds.), August 1992, pp. 62–P.

- [Rai91] Y R Raizer, *Gas discharge physics*, Springer Verlag, Berlin, Germany, 1991.
- [Rak87] V I Rakhovsky, *State of the art of physical models of vacuum arc cathode spots*, IEEE Transactions on Plasma Science **PS-15** (1987), no. 5, 481–487.
- [RF62] D Rapp and W E Francis, *Charge exchange between gaseous ions and atoms*, J. Chem. Phys. **37** (1962), no. 11, 2631–2645.
- [RG67] E J Robinson and S Geltman, *Single- and double-quantum photodetachment of negative ions*, Phys. Rev. **153** (1967), no. 1, 4–8.
- [Ric03] O A Richardson, *The electrical conductivity imparted to a vacuum by hot conductors*, Phil. Trans. Roy. Soc. London **A201** (1903), 497–549.
- [Rie89] K U Riemann, *The bohm criterion and the field singularity at the sheath edge*, Phys. Fluids **B1** (1989), no. 4, 961–964.
- [RWKS96] B Rethfeld, J Wendelstorf, T Klein, and G Simon, *A self-consistent model for the cathode fall region of an electric arc*, J. Phys. D: Appl. Phys. **29** (1996), no. 1, 121–128.
- [Sch99] W Schneider, *Studies on arcing phenomena at high current discharges*, Ph.D. thesis, University of Essex, 1999.
- [Sel97] J H Selverian, *Finite difference model of thorium transport in tungsten*, Acta mater. **45** (1997), no. 12, 5099–5110.
- [SHL00] L Sansonnens, J Haidar, and J J Lowke, *Prediction of properties of free burning arcs including effects of ambipolar diffusion*, J. Phys. D: Appl. Phys. **33** (2000), 148–157.
- [SLR93] S C Snyder, G D Lassahn, and L D Reynolds, *Direct evidence of departure from local thermodynamic equilibrium in a free-burning arc-discharge plasma*, Phys. Rev. E **48** (1993), no. 5, 4124–4127.
- [SMB97] L I Sharakhovsky, A Marotta, and V N Borisyuk, *A theoretical and experimental investigation of copper electrode erosion in electric arc heaters: II. The experimental determination of arc spot parameters*, J. Phys. D: Appl. Phys. **30** (1997), no. 14, 2018–2025.
- [SMHR95] S C Snyder, A B Murphy, D L Hofeldt, and L D Reynolds, *Diffusion of atomic hydrogen in an atmospheric-pressure free-burning arc discharge*, Phys. Rev. E **52** (1995), no. 3, 2999–3009.
- [SRF+94] S C Snyder, L D Reynolds, J R Fincke, G D Lassahn, J D Grandy, and T E Repetti, *Electron-temperature and electron-density profiles in an atmospheric-pressure argon plasma jet*, Phys. Rev. E **50** (1994), no. 1, 519–525.
- [SST90] K Schade, G Suchanek, and H J Tiller, *Plasmatechnik, Anwendungen in der Elektronik*, Verlag Technik, Berlin, 1990.
- [Sta03] J Stark, *Zur Kenntnis des Lichtbogens*, Annalen der Physik **12** (1903), 673–713.

- [Tho93] M F Thornton, *Spectroscopic determination of temperature distributions for a TIG arc*, J. Phys. D: Appl. Phys. **26** (1993), 1432–1438.
- [Thr98] T Thrum, *Numerische Modellierung gepulst betriebener Hochdruckentladungslampen*, Dissertation, Universität Karlsruhe, Lichttechnisches Institut, 1998, Logos Verlag, Berlin.
- [vdM90] J A M van der Mullen, *Excitation equilibria in plasmas: A classification*, Phys. Rep. **191** (1990), no. 2-3, 109–220.
- [vdSS91] M C M van de Sanden and P P J M Schram, *Generalized law of mass action for two-temperature plasma*, Phys. Rev. A **44** (1991), no. 8, 5150–5157.
- [Vil82] F Vilsmeier, *Laserstreuung und Stromtransport im Argon-Bogenplasma*, Dissertation, TU München, 1982.
- [War55] R Warren, *Interpretation of field measurements in the cathode region of glow discharges*, Phys. Rev. **98** (1955), 1658–1664.
- [Way71] J F Waymouth, *Electric discharge lamps*, MIT Press, 1971.
- [WDWS97a] J Wendelstorf, I Decker, H Wohlfahrt, and G Simon, *Investigation of cathode spot behavior of atmospheric argon arcs by mathematical modeling*, XII International Conference on Gas Discharges and their Applications, Greifswald, Germany (G Babucke, ed.), vol. I, INP, September 1997, pp. 62–65.
- [WDWS97b] J Wendelstorf, I Decker, H Wohlfahrt, and G Simon, *TIG and plasma arc modelling*, Mathematical Modelling of Weld Phenomena 3 (H Cerjak, ed.), Materials Modelling, The Institute of Materials, 1997, pp. 848–897.
- [Wen90] J Wendelstorf, *Untersuchungen zu den in der Plasma-Wand-Wechselwirkung auftretenden Plasmaschichten*, Diplomarbeit, TU Braunschweig, Institut für Theoretische Physik, Dec 1990, (Prof. Dr. G. Simon).
- [Wie98] H Wiesmann, *Zweidimensionale Simulation von Hochdruckgasentladungslampen unter Berücksichtigung der Elektrodenbereiche mit der Finite-Elemente-Methode*, Dissertation, Universität Karlsruhe, Shaker Verlag, 1998.
- [Wil96a] R Wilhelm, *Berechnung des Strahlungsdiffusionsanteils der Wärmeleitfähigkeit von Hochdrucklampen-Plasmen*, Interner Bericht, Universität Karlsruhe, Lichttechnisches Institut, 1996.
- [Wil96b] R Wilhelm, *Numerische Modellierung der Transporteigenschaften dotierter Hochdrucklampen-Plasmen*, Diplomarbeit, Universität Karlsruhe, Lichttechnisches Institut, Januar 1996.
- [YW79] S W H Yih and C T Want, *Tungsten-sources, metallurgy, properties, and applications*, Plenum Press, New York and London, 1979.
- [ZLM92] P Zhu, J J Lowke, and R Morrow, *A unified theory of free burning arcs, cathode sheaths and cathodes*, J. Phys. D: Appl. Phys. **25** (1992), 1221–1230.

- [ZT91] O C Zienkiewicz and R L Taylor, *The finite element method. Volume 2: Solid and fluid mechanics, dynamics and non-linearity*, 4 ed., vol. 2, McGraw Hill, London, 1991.

Wissenschaftliche Veröffentlichungen und Tagungsbeiträge allgemeiner Art:

1. I. Decker, J. Wendelstorf und H. Wohlfahrt: Laserstrahl-WIG-Schweißen von Aluminiumlegierungen. *DVS-Berichte*, Bd.170 (1995), S.96-99
2. V.V. Avilov, I. Decker, H. Pursch und J. Wendelstorf: Study of a Laser-enhanced welding arc using advanced split anode technique. In: G. Ecker (ed.), *Proc. ICPIG XXI*, Bochum 19-24.9.1993, Bd.II (1993), S.36-37
3. H. Cui, I. Decker, H. Pursch, J. Ruge, J. Wendelstorf und H. Wohlfahrt: Laserinduziertes Fokussieren des WIG-Lichtbogens. *DVS-Berichte*, Bd.146 (1992), S.139
4. J. Wendelstorf: Komplexität - Das Schicksal moderner Naturbeschreibungen? *4tes ifs-Kolloquium*, IHK Braunschweig, 5.7.97.
5. J. Wendelstorf: Modellierung thermischer Lichtbögen. *3tes ifs-Kolloquium*, Braunschweig, 28-29.6.96.
6. J. Wendelstorf et.al., BRITE/EURAM Project BE-3037: Progress-, Assessment- and Final-Reports. Konferenz- und Ausstellungsbeiträge (EXPO'92, LASER'93 und Workshops).
7. J. Wendelstorf, I. Decker, G. Simon und H. Cui: Untersuchungen zur Laserinduzierten Stabilisierung des Schweißlichtbogens, *Verhandl. DPG (VI)*, Bd.27 (1992), S.1273
8. J. Wendelstorf, G. Simon, J. Kroos und B.R. Finke: Untersuchungen zur Raumladungsschicht in der Plasma-Wand-Wechselwirkung und ihre Bedeutung in der Lasermaterialbearbeitung, *Verhandl. DPG (VI)*, Bd.26 (1991), S.305
9. J. Kroos, G. Simon, J. Wendelstorf und B.R. Finke: Modellierung der Druckbilanz in der Dampfkapillare für den Laserschweißprozeß. *Verhandl. DPG (VI)*, Bd.26 (1991), S.305
10. J. Wendelstorf, G. Simon und B.R. Finke: PIC-Simulation der in der Plasma-Wand-WW auftretenden Raumladungsschicht. *Verhandl. DPG (VI)*, Bd.25 (1990), S.343

Danksagung

Mein besonderer Dank gilt meinem Doktorvater, Herrn Prof. Dr. G. Simon für die Möglichkeit der Anfertigung dieser Arbeit, die angenehme Betreuung und die zahlreichen Anregungen. Seinem Andenken als Wissenschaftler und herausragende Persönlichkeit ist diese Dissertation gewidmet.

Herrn Prof. Dr. U. Motschmann danke ich für die durch den Tod von Prof. Simon veranlaßte Übernahme der Mentorenschaft dieser Arbeit. Seine Verbesserungsvorschläge und sein Engagement haben wesentlich zur Qualität der Darstellung beigetragen und mir die Fertigstellung unter schwierigen Umständen ermöglicht.

Herrn Prof. Dr. M. Kock und Herrn Prof. Dr. J. Mentel danke ich für die Bereitschaft zur Übernahme des Koreferats. Ihnen und den anderen Mitgliedern der von Herrn Prof. Dr. W. Bötticher und Herrn Prof. Dr. K. Günther koordinierten Forscherverbände zum Thema Lampenkatoden sei an dieser Stelle für die Möglichkeit der Mitwirkung an diesem äußerst fruchtbaren Projekt und die zahlreichen Diskussionen gedankt.

Herzlich danken möchte ich mich auch den Kollegen in Europa, USA und Australien für die vielen konstruktiven wissenschaftlichen Diskussionen. Diese Arbeit ist erst durch die freie Kommunikation mit den anderen auf diesem Gebiet tätigen Forschern möglich geworden.

Meine Dankbarkeit gilt besonders meiner Freundin Doris und meinen Eltern für ihre Geduld und Unterstützung.

Die Ergebnisse dieser Arbeit wurden im Rahmen des vom BMBF geförderten Forscherverbundes "Lampenkatoden" (13N7105/9) berechnet. Die notwendigen Erfahrungen und Berechnungsverfahren entstanden in den Jahren 1994 bis 1999 während meiner Tätigkeit am Institut für Schweißtechnik der TU-Braunschweig unter der Leitung von Herrn Prof. Dr. H. Wohlfahrt. Er und seine Mitarbeiter und Mitarbeiterinnen haben die Durchführung dieser Arbeit erst möglich gemacht. Alle hier nicht namentlich genannten Freunde und Kollegen mögen mir verzeihen, daß ich an dieser Stelle nur noch Frau Dr. B. Rethfeld und Herrn R. Montero erwähne, die im Rahmen ihrer Diplomarbeit einen Beitrag zum Gelingen dieser Arbeit geleistet haben.